Dissertation for the degree of Doctor of Philosophy (PhD)

pH AND pH GRADIENTS REGULATE THE Hv1 ION CHANNEL IN MYELOID-DERIVED SUPPRESSOR CELLS AND MODULATE THE PHARMACOLOGY OF THE KCa3.1 CHANNEL OF T CELLS

by Marco Cozzolino

Supervisor: György Panyi, MD, PhD, DSc

UNIVERSITY OF DEBRECEN
DOCTORAL SCHOOL OF MOLECULAR MEDICINE

DEBRECEN, 2024

TABLE OF CONTENTS

LIST OF ABBREVIATIONS

1-EBIO: 1-Ethylbenzimidazolinone

2-GBI: 2-guanidinobenzimidazole

APC: Antigen presenting cell

Arg: Arginine

BK: Big-conductance Ca^{2+}-activated K^+ channels

CaM: Calmodulin

CaMBD: Calmodulin binding domain

CHO: Chinese hamster ovary

ClGBI: 5-chloro-2-guanidinobenzimidazole

CNS: Central nervous system

CRAC: Calcium release-activated channels

Cryo-EM: Cryo-electron microscopy

DAG: Diacylglycerole

EC_{50}: Half maximal effective concentration

G_K: Conductance of K^+

HA/HB/HC: Helix A/B/C

HEK: Human embryonic kidney

HIF: 3-(2-amino-5-methyl-1H-imidazol-4-yl)-1-(3,5-difluorophenyl)propan-1-one

HNSCC: Head and neck squamous cell carcinoma

H_v: voltage-gated proton channel

IFN: Interferon

IK: Intermediate-conductance Ca^{2+}-activated K^+ channels

IL: Intereleukin

IP_3: 1,4,5-inositol triphosphate

K_{Ca}: Calcium-activated potassium channel (h-: human, r-: rat)

K_d: dissociation constant

K_{ir}: Inwardly-rectifying potassium channel

K_v: Voltage-gated potassium channel

K_{2P}: Two P-domain potassium channel

LLC: Lewis lung cancer

(PMN/Mo-)MDSC: Polymorphonucleate/monocytic myeloid-derived suppressor cell

MHC: Major histocompatibility complex

MMP: Matrix metalloproteinase

MPO: Myeloperoxidase

mRNA: messenger ribonucleic acidnA: Nanoampere

NF: Nuclear factor

NFAT: Nuclear factor of activated T-cells

NK: Natural killer cell

P: Pore loop

pA: Picoampere

PBL: Peripheral blood lymphocyte

PD: Pore-forming domain

PDAC: Pancreatic ductal adenocarcinoma

pH_e: Extracellular pH

pH_i: Intracellular pH

PIP_2: Phosphatidylinositol 4,5-bisphosphate (PIP2)

PKC: Protein kinase C

PLC: Phospholipase C

qPCR: Quantitative polymerase chain reaction

RCK: Regulator of conductance of potassium domain

RNS: Reactive nitrogen species

ROS: Reactive oxygen species

SF: Selectivity filter

SK: Small-conductance Ca^{2+}-activated K^+ channels

SKA-31: Naphtho[1,2-d]thiazol-2-ylamine

TAM: Tumor-associated macrophages

TCR: T cell receptor

TIL: Tumor-infiltrating lymphocyte

TME: Tumor microenvironment

TM: Transmembrane domain

TNF: Tumor necrosis factor

TRAM-34: Triarylmethane-34

VCF: Voltage-clamp fluorometry

VSD: Voltage-sensitive domain

1 PREFACE

All cells, including immune and cancer cells, rely on ion channels for their survival and for other important cellular functions. Ion channels are proteins and, thus, are strongly sensitive to several parameters pertaining to their surrounding environment such as pH. Since ion channels are transmembrane proteins embedded in the lipid bilayer reaching both the intracellular and the extracellular milieu, changes in both the pH_i and the pH_e can affect their correct functionality and some of their properties. For example: $K_v1.3$, one of the most important voltage-gated K^+ channels regulating several different physiological functions, mostly in the immune system, is extremely sensitive to changes in both the intracellular and extracellular pH.

The work presented here attempts to extend our knowledge of the relationship between pH and ion channels to $K_{Ca}3.1$ which, along with $K_v1.3$, colocalizes in the immune synapse of T cells and is pivotal for their Ca^{2+}-dependent activation. Contrary to our vast knowledge about $K_v1.3$, not much is known about the pH sensitivity of $K_{Ca}3.1$. Several activators of $K_{Ca}3.1$ have been discovered in the last decades and they have been proposed as possible immune boosters, mostly against cancer. However, the deeply dysregulated and acidic tumor microenvironment (TME) strongly affects the neighboring cells, even influencing their intracellular pH. We analyzed, using whole-cell patch-clamping, the efficacy of Riluzole and SKA-31 using a range of different intracellular and extracellular solutions. To better characterize $K_{Ca}3.1$ we also used several specific mutations of $K_{Ca}3.1$ and Calmodulin.

Besides lymphocytes, tumors host a plethora of other immune cells, some of them acting in favor of the tumor itself. One of these is the family of myeloid-derived suppressor cells, which are related mostly to neutrophils and monocytes, which rely on the pH-sensitive proton channel H_v1 for several functions. Moreover, recently it has been discovered that *in vitro* generated myeloid-derived suppressor cells express H_v1 as their major plasma membrane channel. This prompted us to investigate the expression of H_v1 in an *in vivo* murine model. We chose the Lewis lung carcinoma cell line as a suitable one because of its tendency towards developing an immunologically "cold" tumor environment rich in pro-tumor cells. The subcutaneously developing tumor masses were excised and myeloid-derived suppressor cells were obtained through fluorescence-activated cell sorting. The presence of H_v1 in these cells was assessed at the protein and mRNA level through Western blotting, qPCR and immunofluorescence. We used whole-cell patch-clamping and several solutions titrated to different pH values to thoroughly analyze the biophysical and pharmacological properties of H_v1 in these cells.

2 INTRODUCTION

2.1 Ion channels

2.1.1 General information about ion channels

Ion channels are membrane proteins localized either in the plasma membrane or in the membrane of several intracellular organelles (1). As their name suggests, ion channels let ions passively diffuse across the membrane following their electrochemical gradient (2). Ion channels can transport up to 10^8 ions per second across the membrane (3), while functionally similar proteins called pumps/transporters have a ~1000+ times slower transport rate and in many cases can actively carry ions against their electrical and/or concentration gradients (4). These two main differences, i.e. transport rate and energetics, separate the two families, ion channels and pumps/transporters, which otherwise have several contact points and "blurred boundaries" (2,5). In this dissertation I will deal mostly with K^+- and H^+-channels, so they will receive a deeper analysis.

2.1.2 K^+ channels

K^+ channels belong to one of the biggest families of ion channels in the mammalian class, with almost 80 genes and even more functional proteins (6). They are multimers composed of different subunits, usually a pore-forming α-subunit accompanied by smaller accessory (β) subunits that have an influence on their gating and expression (7). The K^+ channel family can be divided into 4 different subfamilies: a) inwardly-rectifying K^+ channels (K_{ir}), b) voltage-gated K^+ channels (K_v), c) Ca^{2+}-activated K^+ channels (K_{Ca}) and d) two P domain K^+ channels (K_{2P}) (6,8). The pore forming α-subunits of K^+ channels are multimers of four or two monomers. Each monomer contributes to the pore-forming domain (PD) (9), formed by the pore-loop (P) and the surrounding transmembrane domains (TM). The P, which contributes to the permeation of ions and in some channels gating, contains a conserved α-helix of 12 residues, called the pore helix (10), the turret connecting the TM5 and the pore helix, and the signature sequence for a K^+ selective pore (GYGD). The selectivity filter (SF), which makes the channels extremely specific for K^+ ions (at least 10,000 times more than for Na^+ ions (9)) is formed by four signature sequences strategically held in position by interactions with the pore helices (**Figure 1**).

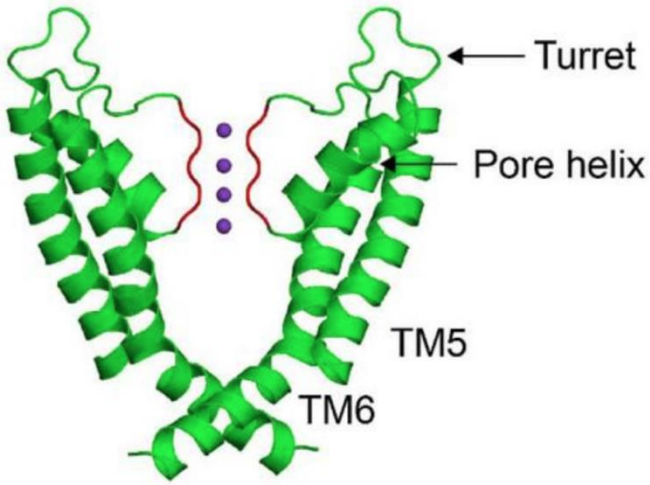

Figure 1. **Representation of the pore domain of a K_v channel**. The image portraits the pore domain of the K_v1.2-2.1 paddle chimera channel (Protein Data Bank: 2R9R), showing two opposite subunits. The selectivity filter is marked in red and the K^+ ions are depicted as purple spheres. Cropped from Figure 1B of (11).

The main difference between the 4 subfamilies lies in the number of Ps and TMs that characterize every K^+ channel monomer (**Figure 2**) (12). By order: 1) K_{ir} channels are tetramers, the monomers are formed by only 2 TMs and 1 P, lying between the two TMs (**Figure 2A**). 2) K_v channels are organized as tetramers of subunits composed of 6 TMs and 1 P, located between TM5 and TM6. Characteristic of these channels is the presence of charged amino acids (mostly Arg) in TM4 and their counter-charges in TM1-TM3. The positive charges in TM4 confer voltage-sensitivity to the channel and the voltage-sensitive domain (VSD) is defined by TM1-TM4 (**Figure 2B**). 3) K_{Ca} channels are tetramers, monomers are characterized by 6 (K_{Ca}2/3, **Figure 2E**) or 7 TMs (K_{Ca}1, **Figure 2D**). To harmonize K_{Ca}1.1 structure/nomenclature with K_v channels the additional TM at the N-terminus of the channels is denoted as TM0. In this way P is conventionally positioned between TM5 and TM6 and VSD is formed by TM1-TM4. K_{Ca}2/3 channel monomers have a similar transmembrane topology to K_v channels except that they lack the positively charged amino acids in TM4 required for voltage sensing. Interestingly, 4) K_{2P} channels (**Figure 2C**) deviate from the tetrameric rule of subunit stoichiometry and are composed of monomers with – as the name suggests – 2 Ps and 4 TMs (12). I give a more detailed description of the channels belonging to the 3rd subfamily below.

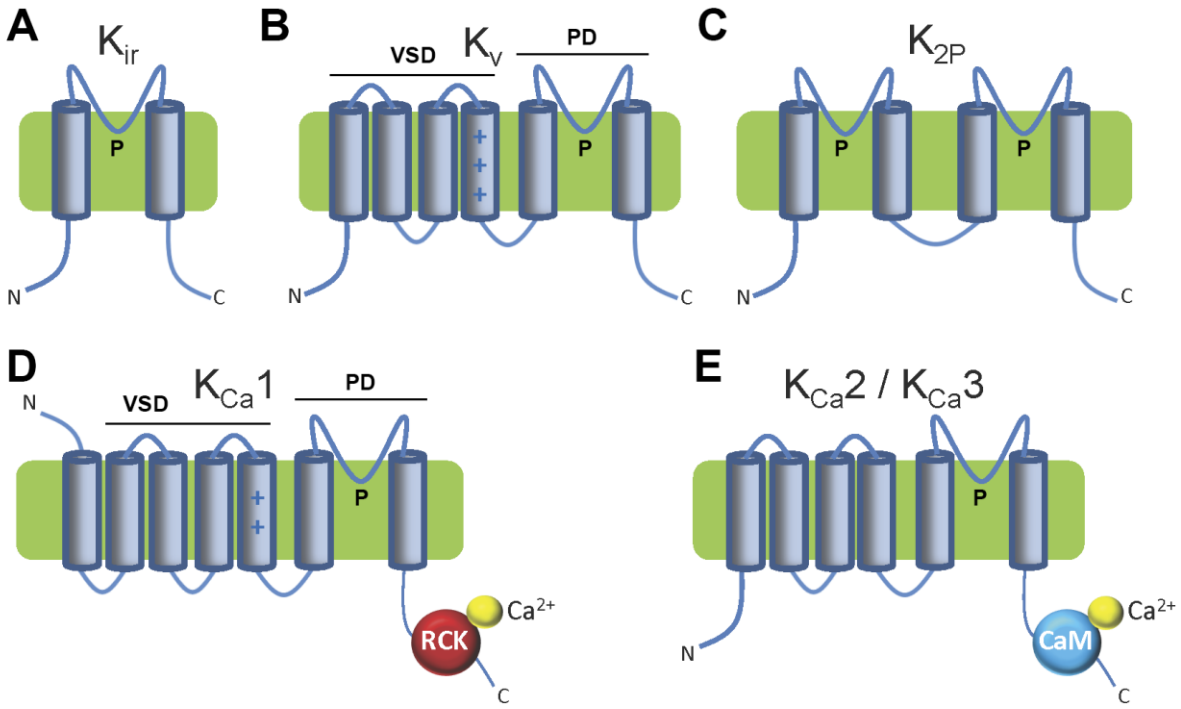

Figure 2. **Schematic structure of the different families of K^+ channels.** The image shows the structure of the α-subunit of each family of K^+ channels, emphasizing the differences in the number of transmembrane helices and showing the position of the pore domains/selectivity filters (P) and the voltage-sensitive domains (VSD). (**A**) Inwardly-rectifying K^+ channels (K_{ir}). (**B**) Voltage-gated K^+ channels (K_v). (**C**) Two-pore domain K^+ channels (K_{2P}). (**D** and **E**) Ca^{2+}-activated K^+ channels (K_{Ca}), in particular big-conductance channels ($K_{Ca}1$) (**D**) and intermediate-small conductance channels ($K_{Ca}2/3$) (**E**). Cropped and modified from Figure 1 of (12).

2.1.3 K_{Ca}: Ca^{2+}-activated K^+ channels

Ca^{2+}-activated K^+ channels (K_{Ca}) can either be small- and intermediate-conductance channels (SK1-3, also known as $K_{Ca}2.1$, $K_{Ca}2.2$, $K_{Ca}2.3$ and IK1, also known as $K_{Ca}3.1$) or big/large-conductance channels (BK, also known as $K_{Ca}1.1$) (6). While $K_{Ca}2.x$ and $K_{Ca}3.1$ have a conductance of 4-14 and 32-39 pS, respectively, the conductance of BK channels is 200-300 pS (13). In contrast to SK and IK, BK channels are structurally different, as stated before (8). Besides the differences in the number of TMs, BK channels are differentiated phylogenetically (14) from the other Ca^{2+}-activated K^+ channels and in other aspects of their structure: BK channels are also voltage-gated due to the charged VSD and they do not need auxiliary proteins to confer Ca^{2+}-dependent gating since they are directly activated by intracellular Ca^{2+} through their "regulator for conductance of potassium" (RCK) domain located in the C-terminal (15). Conversely, the gating of SK1-3, whose similarity lies around 80-90% (16) and IK1, whose sequence is ~40% identical to $K_{Ca}2.x$ channels (17), is completely insensitive to the membrane

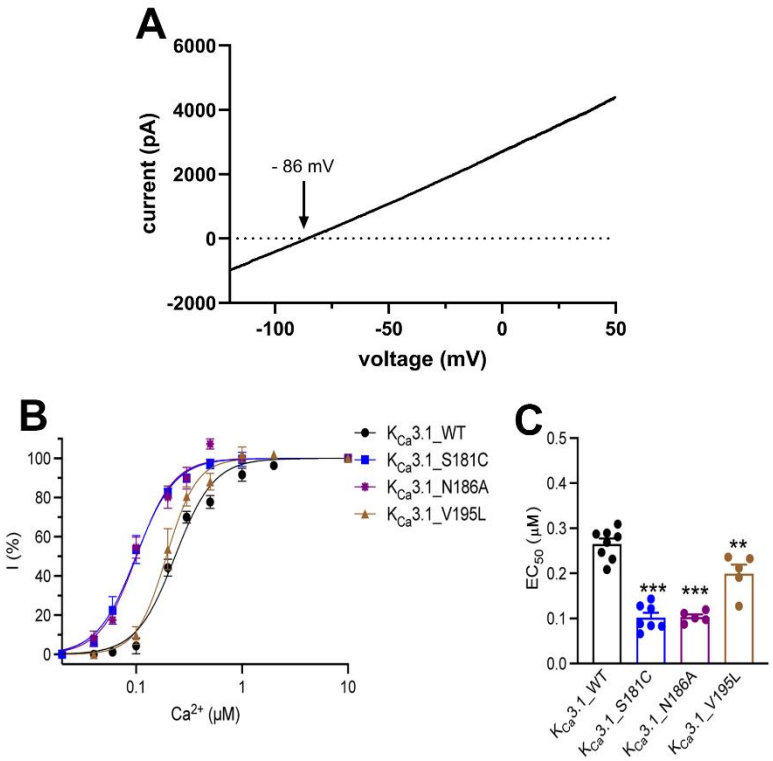

Figure 3. **Representation of a typical K_{Ca}3.1 current**. (**A**) Typical current recorded in a transfected CHO cell using a voltage ramp from -120 mV to +50 mV and an intracellular solution with 1 µM free Ca^{2+}. After the subtraction of its leak component, the current can be seen to be ~ 0 when the applied voltage is equal to equilibrium potential of the K^+ ions (~ -89 mV). (**B** and **C**) The sensitivity of K_{Ca}3.1 to intracellular Ca^{2+} concentrations is well described by a sigmoid curve (**B**, black). EC_{50}, in this case, is 270 nM. Using an intracellular solution with 1 µM free Ca^{2+}, like in (**A**), permits the development of a highly saturated current. Sensitivity to intracellular Ca^{2+} can be modified by specific aminoacidic mutations (**B** and **C**, other colors). (**B** and **C**) are cropped and modified from Figure 3 of (18).

potential (**Figure 3A**). These channels need Calmodulin (CaM), a cytosolic Ca^{2+}-binding protein (15) to confer the Ca^{2+} sensitivity of gating (**Figure 3B, C**). Finally, there is a difference among Ca^{2+}-activated K^+ channels regarding their tissue distribution. K_{Ca}3.1 can be normally localized in blood cells, placenta, pancreas, liver, lungs and vascular smooth and endothelial cells (19,20). K_{Ca}2.x channels mostly reside in the central nervous system (CNS) (20). Contrariwise, BK channels are ubiquitous and can be found both in CNS and in skeletal and smooth muscles (21), but have a role even in the regulation of hormone release (22).

2.1.4 The structure of the SK and IK Ca^{2+}-activated K^+ channels

Until 2018 we had only partial crystal structures of the Ca^{2+}-activated K^+ channels (23). Only recently cryo-electron microscopy (cryo-EM) unveiled new details about the precise structure of the human K_{Ca}3.1 (24). As already mentioned, the members of this sub-family assemble in tetrameric structures and each subunit has 6 TMs, with the PD constituted by the sequence TM5-P-TM6 (8). The P is located between TM5 and TM6 and TM1-4 directly contact

the PD of the same subunit instead of the PD belonging to the adjacent one, as it happens in most K_v1 channels (24). In this sense, $K_{Ca}3.1$ is not domain-swapped whereas all $K_v1.x$ structures indicate domain swapping. Both the N- and the C-terminal are located in the intracellular side. The C-terminus is preceded by three α-helices (HA, HB and HC): while the first two helices run almost parallel to the membrane and anti-parallel to each other, HC takes a 90° turn and, coupled with the other HC domains from the other three subunits, creates a perpendicular column at the bottom of the channel (24) (**Figure 4**). Before 2018 the available crystal structures did not differentiate between the three α-helices and the intracellular C-terminal region was structurally divided into three different sequences: CaMBD1, CaMBD2A and CaMBD2B (which roughly corresponds to what now is defined as HB) (25). This entire subdivision is now considered an unreliable artefact (26). $K_{Ca}2.x$ and $K_{Ca}3.1$ channels are unable to directly sense the intracellular Ca^{2+}, hence they associate intracellularly with four CaM (one per each subunit), a cytosolic protein with two conserved (27) globular lobes connected by a very flexible linker (28). CaM binds constitutively HA and HB with its C-lobe, whereas the N-lobe has more freedom of movement (**Figure 4**) (24). Binding up to 4 Ca^{2+} ions prompts CaM to reach an extended conformation (28,29).

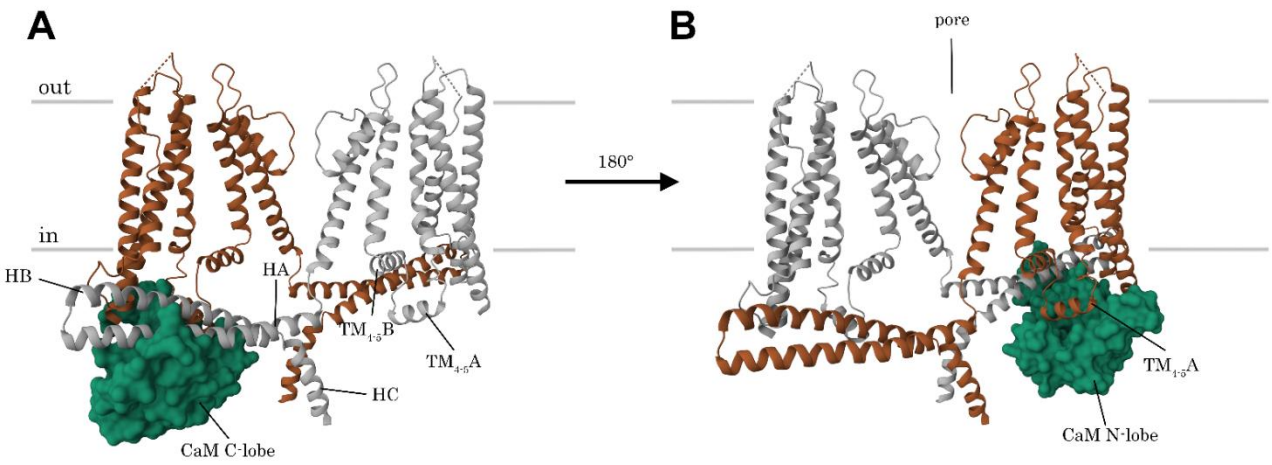

Figure 4. **Structure of hK$_{Ca}$3.1 and CaM**. Cryo-EM structure of the complex hK$_{Ca}$3.1-CaM (Protein Data Bank n. 6CNO), showing how Ca^{2+}-bound-CaM (green) strongly binds HA and HB of an α-subunit (grey) with its C-lobe (**A**) and $TM_{4-5}A$ of an adjacent one (orange) with its N-lobe (**B**). For sake of clarity only two α-subunits and only one CaM are shown. The image has been obtained by using https://www.rcsb.org/3d-sequence/6CNO?assemblyId=1

In $K_{Ca}3.1$ the intracellular linker between TM4 and TM5 is formed by two different α-helices ($TM_{4-5}A$ and $TM_{4-5}B$) which have contacts both with HA and the pore region of the same subunit, in particular TM6 (24). Cryo-EM has shown that $TM_{4-5}A$, which is highly

conserved across the SK channel family, is the portion to which the N-lobe of CaM binds when it is in the Ca^{2+}-bound extended conformation (24). The interaction between CaM and $TM_{4-5}A$ causes a downward pull of $TM_{4-5}B$ and the pore-lining TM6. This will result in the dilation of the cytosolic entrance to the pore from ~1 to 3.5 Å, thereby permitting the partially hydrated K^+ ions to freely flow outside of the cell (24). This is partially in contrast with the historical knowledge about K_{Ca} channels based on the outdated crystal structure, which proposed the N-lobe of CaM to bind the C-terminal of the adjacent subunit in order to move TM6 and open the channel (25).

2.1.5 Positive and negative modulators of Ca^{2+}-activated K^+ channels

Even if the members of the $K_{Ca}2.x$ and $K_{Ca}3.1$ families are structurally similar (17) their sensitivity to positive and negative modulators are remarkably different. Among the pore-blocking peptide toxins, maurotoxin (30) (IC_{50} = ~1 nM for $hK_{Ca}3.1$ (30)) and charybdotoxin (30,31) (IC_{50} = ~10 nM for $hK_{Ca}3.1$ (8)) are selective for $K_{Ca}3.1$, while the bee venom-derived apamin does not inhibit $K_{Ca}3.1$ (30,32), but is specific for $K_{Ca}2.x$ with different affinities (32): $K_{Ca}2.2$ (IC_{50} = ~30-100 pM for $hK_{Ca}2.2$ (33,34) and $rK_{Ca}2.2$ (32)) > $K_{Ca}2.3$ (IC_{50} = ~1-2 nM for $hK_{Ca}2.3$ (32,34)) > $K_{Ca}2.1$ (IC_{50} = ~3-4 nM for $hK_{Ca}2.1$ (32,33)). The potent and $K_{Ca}3.1$-specific small organic molecule inhibitors Clotrimazole (IC_{50} = 70-250 nM), TRAM-34 (IC_{50} = 20 nM) and Senicapoc (IC_{50} = 11 nM) bind to different locations in the inner portion of the pore (35,36). Besides blockers, several activators (henceforth also called enhancers) of Ca^{2+}-activated K^+ channels have been discovered. The first activator, 1-ethyl-2-benzimidazolinone (1-EBIO), pertaining to the family of benzimidazolones, was reported in 1996 (37). 1-EBIO, contrary to the peptide blockers but like several other enhancers, is not very potent and cannot differentiate between the four K_{Ca} channel types, even if it is more specific for $K_{Ca}3.1$ (EC_{50} = ~30-70 μM for $hK_{Ca}3.1$ (38,39)) compared to the members of the $K_{Ca}2.x$ family (EC_{50} = ~650 μM for $hK_{Ca}2.1$ (40) and $rK_{Ca}2.2$ (39), EC_{50} = ~170-1000 μM for $hK_{Ca}2.3$ (41,42) and for $rK_{Ca}2.3$ (43)). In the following years several new molecules have been developed whose structure generally resembles that of 1-EBIO (44), but their $K_{Ca}3.1$ affinity increased dramatically reaching the nanomolar range. For example, the halogenized derivative of EBIO (di-chloro-EBIO) (45) can activate $K_{Ca}3.1$ with an EC_{50} = 1-2 μM and $hK_{Ca}2.x$ channels with an EC_{50} = 10-30 μM (42,46) and the oxime NS309 (47) can activate $hK_{Ca}3.1$ with an EC_{50} = 10-30 nM and $hK_{Ca}2.x$ channels with an EC_{50} = 100-600 nM (42,46). Even if these molecules are potent enough, the fact that they are only 10-15 times more selective for $K_{Ca}3.1$ compared to $K_{Ca}2.x$ can cause CNS-related side effects if applied *in vivo* (48). A new generation of activators (SKA-111, SKA-121), 40-100 times more selective for $K_{Ca}3.1$, gives new hopes

about the clinical utilization of such substances (26). Molecules with more diverse structures were also discovered and they show more complex specificities, e.g. CyPPA and NS13001 recognize only $K_{Ca}2.2$ and $K_{Ca}2.3$, while CM-TPMF and GW542573X are selective only for $K_{Ca}2.1$ (44). In this dissertation we used, as positive modulators, two molecules: SKA-31 and Riluzole. Riluzole is a neuro-protective drug used to inhibit the release of glutamate as a neurotransmitter, but it has been repurposed as an enhancer of Ca^{2+}-activated K^+ channels (49). SKA-31 is one of the molecules obtained using Riluzole as a template (50), but it is a much stronger enhancer (for $hK_{Ca}3.1$ EC_{50} = 1-2 μM for Riluzole and 220-260 nM for SKA-31 (51)).

2.1.6 The mechanism of action of the positive modulators of Ca^{2+}-activated K^+ channels

1-EBIO and the other enhancers are lipophilic substances (52), therefore they are able to cross the plasmatic membrane reaching the intracellular regions of the Ca^{2+}-activated K^+ channels. In 2013 Zhang et al. determined the crystal structure of the CaM-binding domain of $hK_{Ca}2.2$ when bound to either 1-EBIO or NS309 (53,54) and discovered that both these molecules occupy a little pocket between CaM and CaMBD2B, interacting with specific amino acid residues that, when appropriately mutated, transformed the mildly 1-EBIO-sensitive $K_{Ca}2.2$ channel and obtained a new phenotype that is similar to the highly 1-EBIO-sensitive $K_{Ca}3.1$ (53). Other substances like CyPPA and Riluzole were suggested to have their binding site at the same interface (55). Recently the cryo-EM-derived structure of $hK_{Ca}3.1$ (24) has somehow made obsolete the results obtained by the aforementioned X-ray diffraction methods, mostly because the entire C-terminus reported by X-ray diffraction is now considered an artefact (26). With the new cryo-EM structure available, Lee and MacKinnon proposed that the binding pocket is different from the interaction surface of CaMBD2B/HB and the N-lobe of CaM, but the binding is rather between $TM_{4\text{-}5}A$ and the N-lobe of CaM (24). It was believed that the residues involved in the interaction with substances like 1-EBIO were A477 and L480 (**Figure 5A**, $rK_{Ca}2.2$, corresponding to V365 and M368 in $hK_{Ca}3.1$) (53,56), but the new and more accurate structure suggests that the involved residue could be L185 (in $hK_{Ca}3.1$, corresponding to L292 in $rK_{Ca}2.2$) (**Figure 5B**) (24). The involvement of L185, S181 and A184 in the recognition of molecules like SKA-111, SKA-31 and SKA-121 has been confirmed by Wulff's team, that showed that mutating these residues induces a dramatic loss in the efficacy of SKA-111 (26). Recently, Attali's team reached a similar conclusion showing that BA6b9, a structural analogue of 1-EBIO which however acts as a blocker, positions itself in the same pocket as the enhancers do, but contacts different residues (57). Interestingly, even if the new cryo-EM structure revolutionized the knowledge about what part of $K_{Ca}3.1$ is actively

implicated in the recognition of a substance like 1-EBIO, the residues of the N-lobe of CaM that bind the positive modulators are still thought to be essentially the same (F19, I27, L32, M51, I52, E54, V55, I63, F68, M71, M72, K75) (26,53). Constant progression has been made in regard to understanding how the modulators and the channels interact, but it is still not clear what exactly ensues after this interaction. $K_{Ca}3.1$ and the $K_{Ca}2.x$ channels have been reported to have submicromolar Ca^{2+} sensitivity ($K_{Ca}3.1$ EC_{50} = 100-400 nM, $K_{Ca}2.x$ EC_{50} = 300-750 nM) (18,58–61), this means that the physiological intracellular concentration (~100 nM) is normally unable to strongly activate the channels (62). Substances like NS309 (63,64), 1-EBIO (65) and SKA-121 (66) enhance the overall Ca^{2+} sensitivity of the channels so that their open probability increases dramatically even without changing the intracellular Ca^{2+} concentration. How this exactly happens is still not clear. Specific aminoacidic mutations can also positively alter the Ca^{2+} sensitivity of channels like $K_{Ca}2.3$ and get the same effect that would be obtained via the use of the activators (26,67,68).

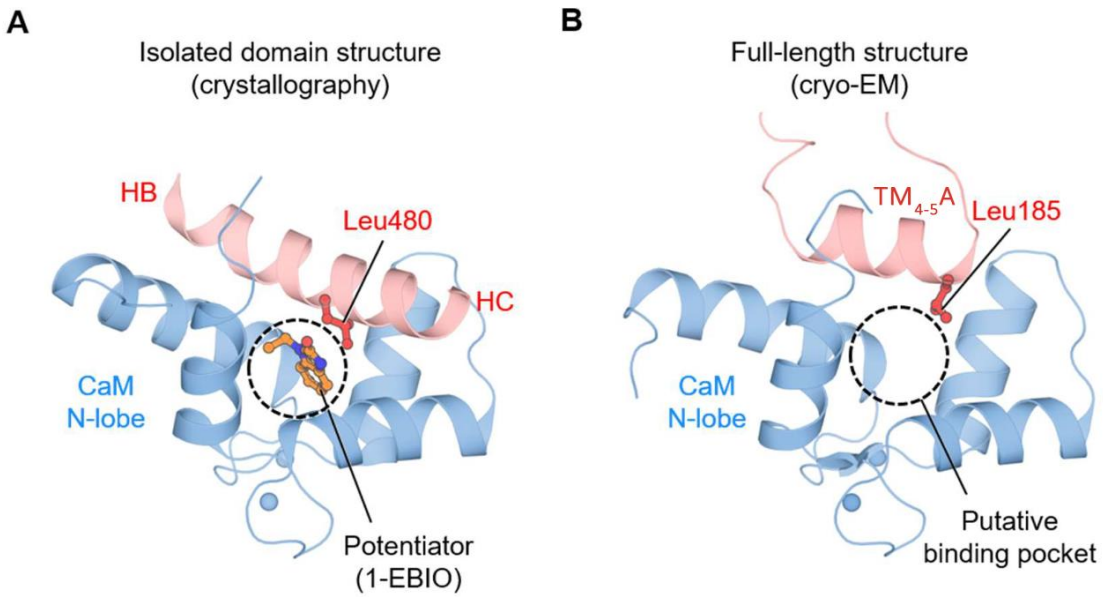

Figure 5. **Location of the putative activator binding pocket in the K_{Ca}-CaM complex**. In an older structure (Protein Data Bank: 4G28) of $K_{Ca}2.2$ obtained via crystallography (**A**) L480 was theorized to mediate the binding with activators like 1-EBIO. A more recent cryo-EM structure of $K_{Ca}3.1$ (**B**) revealed that L185 of the newly resolved helix $TM_{4\text{-}5}A$ occupies a similar location and may be implied in the formation of the binding pocket. Modified from Figure S8 of (24).

2.1.7 H^+ channels: structure and general characteristics

Even if proton currents were recorded since the ‘70s (69), the gene encoding the voltage-gated H^+ channel (H_v1) was independently discovered only in 2006 by the teams led by Yasushi Okamura (70) and David Clapham (71). Despite being widely distributed in nature (72), H_v1 is not redundant and only one gene has been recognized in every species in which it has been

discovered (73). Because of the extremely low amount of free H^+ in the intracellular compartment (40-70 nM), this ion channel needs to be extremely specific and selective and, to date, it has not been proven that H_v1 can let other ions pass across the membrane other than H^+ (72). The strikingly perfect selectivity of H_v1 is accompanied by a peculiar structure: while most voltage-gated channels have a region (usually comprising TM5 and TM6) that serves as a pore-forming domain and a selectivity filter, H_v1 has only 4 TMs out of the 6 usually present and they constitute both the voltage sensor and the permeation pathway for H^+ (72) (**Figure 6A**). While functional as a monomer, H_v1 is usually expressed as a dimer (**Figure 6B**). The 4 TMs of each protomer organize themselves as an hourglass with a narrow constriction in the middle capable of selecting only for H^+ ions thanks to the residue Asp^{112}, implying that each protomer has its own conduction pathway (74) (**Figure 6B**). This is peculiar, but not completely unique, since it has been proven that even the non-conducting TM1-4, comprising VSD of K_v and Na_v channels, can be transformed into structures akin to H^+-selective channels when the real pore domain (TM5-6) is removed or when they are opportunely mutated (74). The same applies to water-conducing aquaporins, which also start letting out protons after specific mutations (74). As the name "H_v1" states, the proton channel is voltage-sensitive and the positive charges (3 Arg residues) important for voltage sensing are in TM4 (75). Since the crystal structure of the open channel is still not available, not much is known about what exactly happens when the depolarization alters the structure of the channel (74). The voltage threshold of H_v1, id est when the channel starts conducting H^+ ions, is directly linked to ΔpH ($pH_o - pH_i$).

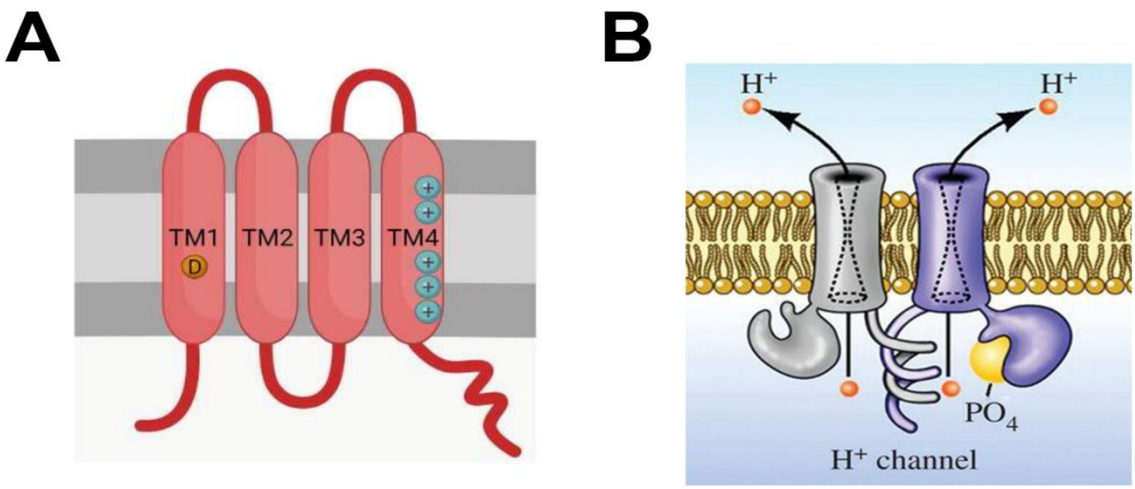

Figure 6. **Schematic structure of H_v1**. (**A**) Each protomer of the channel is made of 4 different TMs. Important residues for gating and selectivity can be found in TM1 (the highly conserved and H^+ selective Asp^{112}, identified with a yellow D) and in TM4 (several basic Arg part of the voltage-sensitive domain, identified with blue +). (**B**) The proton channel H_v1 is usually a dimer constituted by two equally conducting protomers organized in hourglass shapes. The C-termini interact through a coiled coil mechanism while the N-termini can be phosphorylated at the residue Thr^{29} enhancing the overall activity of the channel. Cropped from Figure 4 of (87) (**A**) and Figure 1 of (74) (**B**).

A unique feature of this channel is that the TM4 of H_v1 is extremely sensitive to ΔpH more than to pH itself (75). The voltage threshold when ΔpH ~ 1 is around 0 mV, but it becomes +40 mV when ΔpH ~ 0. In any case the H^+ currents through H_v1 are very slow and take several seconds to develop fully (76). The excess of protons on the intracellular side, id est a more acidic intracellular compartment, stabilize the activated state of the channel along with the membrane depolarization (75). Voltage-clamp fluorometric (VCF) recordings demonstrated that changing pH_i while keeping pH_o constant (hence lowering ΔpH) caused a movement in the TM4. This movement did not happen if ΔpH was kept constant, i.e. changing pH_o as well, proving that TM4 is able to sense the difference between the pH outside and the pH inside, but does not perceive the absolute change either of the intracellular or the extracellular pH (75). pH itself has, anyway, an influence on the activation and deactivation kinetics of the channel. In particular, the ON-gating current decay time constants depend on the internal and external pH values instead of ΔpH. This could be explained by dependence of the conformation of certain portions of the protein like TM4 depends on both pH_i and pH_e (75,77).

2.1.8 Localization and role of H_v1

H_v1 is mostly expressed in cells belonging to the immune system, such as T cells (78), B cells (79), macrophages (80), eosinophils (81), neutrophils (81), plasmacytoid dendritic cells (82) and microglia (83), but it can be found in completely different cells as well, like sperm cells (84). The major role of H_v1 in these cells is to contribute to the "respiratory burst" (85). Phagocytes, in order to destroy what they incorporate in their phagosomes, produce several highly reactive oxygen species (ROS). One of the most abundant and most reactive species is the superoxide anion ($O_2^{-\cdot}$), which is produced by the activity of the transmembrane protein NADPH oxidase, also called NOX. NOX transfers electrons from the cytosolic NADPH to O_2, generating $O_2^{-\cdot}$ in the inside of the phagosome and $NADP^-$ + H^+ in the cytoplasm ($NADPH + O_2 \rightarrow NADP^+ + O_2^{-\cdot} + H^+$) (86).

The accumulation of H^+ will inevitably lead to the acidification of the cytoplasm from a value of 7.4 to ~6 in as low as 10 minutes (88). H_v1 channels, aided by the Na^+/H^+ antiport exchangers, have the leading role of removing the excess of H^+ generated by the NOX-lead respiratory burst and bring back the pH_i to values close to 7.4 (88). Myeloid-derived suppressor cells (MDSCs) exploit several redundant pathways to exert their immune-suppressive and pro-tumoral skills (89) and one of these is the generation of ROS (90) and reactive nitrogen species (RNS) (91). The latter upon direct cell-to-cell contact may cause the nitration of the tyrosine

residues on T cell receptors (TCRs) and CD8 proteins residing on the membrane of infiltrating $CD8^+$ T cells, making them useless and unable to direct their action against the tumor cells (92).

2.1.9 Inhibitors of H_v1

Because of its odd structure and the relative novelty of its discovery, specific blockers of this channel have not been discovered yet. Classical inhibitors of H_v1 are divalent metal ions like Zn^{2+} and Cu^{2+} (69). It has been shown that H_v1 may host two different cooperative binding sites for Zn^{2+} (K_d = 2 μM for hH_v1). At low doses (<1 μM) Zn^{2+} binds to the first site, inhibiting the opening of the channel. At high doses (>1 μM) it occupies the second site as well, inhibiting the outward movement of TM4 (93). Recently the family of guanidine derivatives have been identified as H_v1 blockers as well (94). Contrary to several other pore-blockers which act extracellularly, the guanidine derivatives recognize a spot located in the intracellular side of the pore region. The first molecule synthesized for this purpose was 2-guanidinobenzimidazole (2-GBI) (95). 2-GBI presumably is uncapable of crossing the plasma membrane, hence if applied extracellularly it does not elicit any inhibition (95), moreover because of its positive charges its K_d depends on the membrane potential (from ~110 μM at +20 mV to ~30 μM at +130 mV) (95). A modified version of 2-GBI, named 5-chloro-2-guanidinobenzimidazole (ClGBI), is able to cross the membrane and inhibits hH_v1 with a K_d of ~20 μM (96,97). Even if in the last decade several other proton channel blockers have been discovered and published, both of the family of peptides like Corza-6 (98) and of the family of small molecules like PNX52429/PNX61442 (99) or HIF (100), ClGBI is still one of the most frequently used substances to pharmacologically demonstrate the presence of functional H_v1 ion channels (76,101–104). It must be acknowledged, however, that ClGBI is a "dirty drug" (105), id est an extremely unspecific substance, hence its use is not advisable in an *in vivo* model or in an *in vitro* cell-based model when the cell expresses more than one type of ion channels. As a matter of fact, ClGBI can strongly suppress K^+ currents through ion channels such as $K_v11.1$ and $K_v1.3$ and even Na^+ currents (96). This makes it impossible to study H_v1 using ClGBI in T cells where $K_v1.3$, the principal ion channel regulating activation and proliferation, is also inhibited by ClGBI (96).

2.2 The relationship between the immune system, cancer and ion channels

2.2.1 General information about the immune system

Our body has two ways of protecting itself against invasive pathogens: the innate and the adaptive immune system. The innate immune system is unspecialized and comprises a large number of different types of cells, such as neutrophils, mastocytes, macrophages, natural killer cells, and dendritic cells, capable of recognizing a large spectrum of pathogens. Contrariwise, the B and T lymphocytes that constitute the adaptive immune system are highly specific: every cell is a different clone and is designed to recognize a different antigen. Antigen presenting cells (APCs) like dendritic cells and macrophages have the role of internalizing an antigen and presenting it to T cell through a transmembrane protein complex called MHC (major histocompatibility complex). As a result of the encounter between a MHC-presented antigen and the specific T cell receptor (TCR), circulating naïve T cells will be activated and develop both into clonally proliferating short-lived effector T cells and into memory T cells (106).

2.2.2 The role of K^+ channels in the activation of T cells

The activation of T cells is the result of an intricated phosphorylation cascade that ensues the binding between TCR and the antigen-presenting MHC on APCs (106). The contact between the APC and the T cell causes the formation of an immune synapse, id est the aggregation all the machinery required for the transmission of the signal into a single spot in and below the membrane. Several TCR-associated Tyr-kinases will phosphorylate a series of adaptor proteins activating multiple pathways. The major pathway consists of the phosphorylation and recruitment of PLCγ1, a cytosolic enzyme that will identify its substrate phosphatidylinositol 4,5-bisphosphate (PIP_2) in the inner leaflet of the plasma membrane and hydrolyze it into diacylglycerol (DAG) and inositol 1,4,5-triphosphate (IP_3). DAG is a membrane molecule and acts as a docking point for protein kinases C (PKCs), which will phosphorylate and activate several transcription factors such as NF-κB. IP_3, on the contrary, is a small soluble molecule which diffuses in the cytosol and activates the IP_3 receptor located in the endoplasmic reticulum, freeing the entrapped Ca^{2+} ions and causing a sudden burst of the intracellular Ca^{2+} concentration. The depletion of Ca^{2+} inside the endoplasmic reticulum is sensed by STIM1 and STIM2, two endoplasmic reticulum membrane proteins, which oligomerize with the plasma membrane ORAI1 channel to create a functional Ca^{2+}-release activated Ca^{2+} channel (CRAC). The Ca^{2+} influx through CRAC increases even more the intracellular Ca^{2+} concentration (106,107). Ca^{2+} will ultimately provoke, through the activation of phosphatases like calcineurin, the dephosphorylation and translocation of the transcription

factor NFAT, which contributes to the activation of specific genes involved in the T cell activation (106). The influx of Ca^{2+} from the extracellular side must be balanced by the efflux of another positive ion: T cells use $K_v1.3$ and $K_{Ca}3.1$ to conduct outward K^+ fluxes, thereby avoiding an excessive depolarization of the plasma membrane, which would halt the Ca^{2+} ingress (108). In spite of the fact that the aforementioned process is common to all activating T cells, the number of $K_v1.3$ and $K_{Ca}3.1$ channels on the membrane will be different according to the fate that the cell faces: while naïve T cells present ~300 $K_v1.3$ and ~10 $K_{Ca}3.1$ channels per cell, central memory T cells can upregulate $K_{Ca}3.1$ channels up to ~500 units per cell and effector memory T cells can increase the number of their $K_v1.3$ channels up to 1500 per cell (108). When $K_v1.3$ is knocked down, T cells become unable to produce cytokines like IFN-γ and TNF-α and revert to a predominantly naïve-like state (109). Similarly, $K_{Ca}3.1$-knocked out T cells struggle producing any IFN-γ, TNF-α and IL-2 even after being strongly activated with a mix of CD3 and CD28 (110). The immuno-suppressing effect of genetically deleting $K_v1.3$ or $K_{Ca}3.1$ in T cells can be pharmacologically mirrored by blocking either of these two channels. Margatoxin, a potent $K_v1.3$ peptide blocker, halts the activation of T cells (111) just like TRAM-34, a small molecule blocking specifically $K_{Ca}3.1$, slows down the proliferation of lymphocytes and their production of IL-2 (112). Overstimulating $K_{Ca}3.1$ with 1-EBIO, on the other hand, enhances the ability of T cells to produce cytokines, almost doubling the amount of the generated IFN-γ (113). Based on the crucial role of K^+ channels in T cell activation, understanding the pharmacological properties of $K_v1.3$ and $K_{Ca}3.1$ channels is utmost important. Several *in vitro* and *in vivo* animal experiments showed the applicability of $K_v1.3$ inhibitors in the management of autoimmune diseases (114,115), and the use of $K_{Ca}3.1$ activators to boost anti-cancer immunity (see below).

2.2.3 The immune system and the tumor

Tumor tissue can be considered a broadly inflamed structure that promotes inflammation and that, in turn, is promoted by inflammation, which is tightly bound to the immune system (116). We can find almost all types of infiltrating immune cells in tumor tissues, from the innate ones like macrophages, neutrophils, and dendritic cells, to the adaptive ones like T and B lymphocytes (117). B cells and antibodies do not contribute to the anti-tumor fight substantially and their presence has even been considered, in some cases, a pro-tumorigenic factor (118). On the contrary, infiltrating T cells gain more and more importance in contemporary oncology (119). In particular, cytotoxic $CD8^+$ T cells are almost always a favorable prognosis factor (119) because of their ability to recognize neo-antigens and other proteins on the tumor plasma membrane and subsequently attack the cancerous mass thanks to

the secretion of several cytotoxins (106). On the other hand, myeloid cells are a family of both anti-tumor and pro-tumor elements dwelling in the TME and deeply influencing its evolution (120). Activated neutrophils and activated macrophages, in this case called tumor-associated macrophages (TAMs), usually show an anti-tumor activity but are often overshadowed by a close family of pathologically activated pro-tumor cells, mostly known as myeloid-derived suppressor cells (MDSCs), branched in monocytic-MDSCs (Mo-MDSCs) and polymorphonucleate-MDSCs (PMN-MDSCs) (120).

2.2.4 Myeloid-derived suppressor cells (MDSCs)

MDSCs exert their action in several different ways, both through direct contact with other immune cells and by the production of molecules that have an impact on the tumoral landscape in which these cells live (**Figure 7**) (121). Just like macrophages and neutrophils, MDSCs produce several ROS and RNS. Instead of directing these against pathogens, it is thought that MDSCs can cause the oxidation and nitration of specific residues of the TCR/CD8 complex present on cytotoxic T cells, altering the overall capacity of the immune system to recognize the tumor antigens (122). Even if this is the main way through which the inhibition occurs, the cell-cell interaction between MDSCs and T cells is much more complex and variegated than expected. It has recently been shown that one of the byproducts of the metabolism of MDSCs, the α-dicarbonyl radical methylglyoxal, can be easily transported from the myeloid cells to the neighboring T cells in the context of a tumor. The accumulation of methylglyoxal in the cytoplasm of T cells reacts with L-Arginine and causes its depletion (123). L-Arginine is an essential amino acid for T cells and plays an important role in their activation, proliferation, cytokine production (124) and in their survival rate in harsh IL-2-poor conditions (125). MDSCs deplete extracellular L-Arginine as well as L-Tryptophan and L-Cysteine through the overexpression of the enzymes ARG-1 and IDO1/2 and this inhibits T cell proliferation (121). The strong oxidative properties shown by MDSCs can even have an effect on their own phospholipids, in an effect known as lipid peroxidation (126). Myeloperoxidase (MPO), an enzyme extremely abundant in PMN-MDSCs, can create oxidized lipids that, in a similar manner to methylglyoxal, can be passed from the plasma membrane of myeloid cells to the plasma membrane of close dendritic cells, impairing their cross-presentation of tumor antigens to lymphocytes, worsening the inability of the immune system to properly respond to the tumor (127). Apart from targeting anti-tumor cytotoxic T cells and dendritic cells, MDSCs can also produce cytokines and other molecules that enhance the tumor cell stemness, induce angio- and vasculogenesis and promote extravasation and metastasis (121). Unfortunately, the lack of specific surface biomarkers makes it difficult to distinguish, especially *in vivo*, one

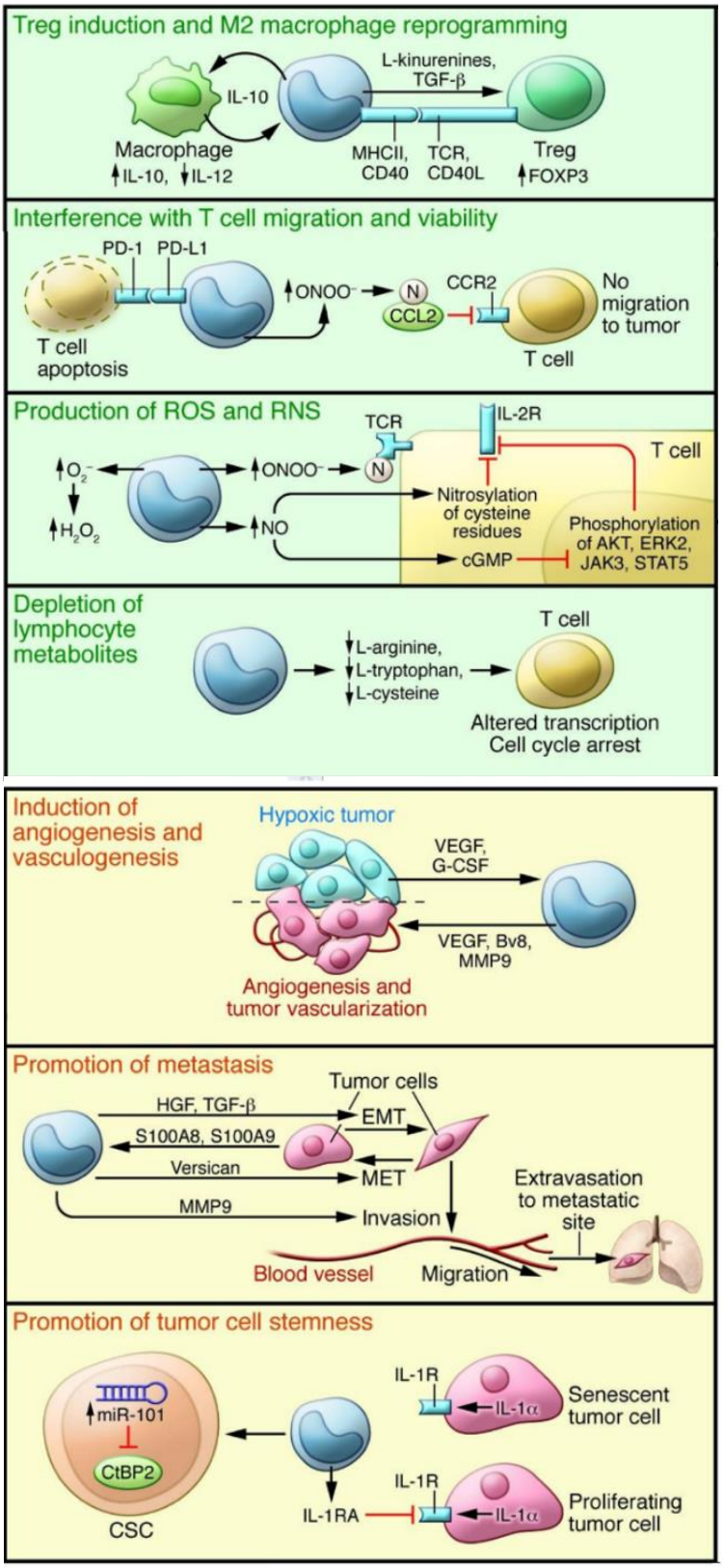

Figure 7. **MDSCs in the context of tumor progression**. MDSCs (blue cells) can promote the advancement of the tumor both influencing directly the local immune system (top) and modeling the TME and the tumor itself (bottom). MDSC can induce T_{reg} profiles and the reprogramming of macrophages; they can cause oxidation and nitrosylation damage to the TCR, to several cytokine and cytokine receptors; they can deplete the metabolites used by lymphocytes. MDSCs can also induce angio- and vasculogenesis; they can promote invasion, migration and metastasis and they can induce cell stemness in tumor cells. Cropped and modified from Figure 3 of (121).

subtype of myeloid cells from another, hindering the research on tumor-associated MDSCs (120). Because of this, even if progress has been made, a specific treatment that can stop pro-tumor MDSCs from exerting their activity is yet to be discovered (120). As compared to T cells (see 2.2.2), relatively less is known about the channelome of MDSCs. Both *in vitro*-generated and *ex vivo* MDSCs present the purinoceptor P2X7R, which can detect extracellular ATP. Consequently, the tumor milieu, rich in ATP (see next chapter 2.2.5 for more details), can activate these channels prompting MDSCs to produce CCL-2, a strong chemokine usually associated with an unfavorable outcome (128), ARG-1, ROS and TGF-β1 (129). MDSCs may express TRPV1 as well, but this has been observed only in a hepatitis model (130).

2.2.5 The positive modulators of Ca^{2+}-activated K^+ channels can counteract high K^+ and high adesonine concentration in the tumor microenvironment

Infiltrating T cells, attracted by the inflammation-related cytokines secreted in the tumor, end up in a unique environment. The TME is a complicated network of cellular and acellular elements, all contributing to the advancement of the tumor itself. The cancer cells are able to influence the TME and, as a consequence, the TME will influence the cancer cells' behavior, their survival rate and their malignancy (131). Rapidly growing tumors are characterized by hypoxia and nutrient deficit, which causes the development of necrotic foci usually associated with poor prognosis (132). Cancer cells will die in big numbers and release their intracellular content in the extracellular tumoral milieu contributing to the development of a chemically pro-tumoral landscape (132). It has been extensively shown, for example, that tumor interstitial fluid is rich mostly in K^+ ions, which directly derive from the local high necrotic rate (133).

The high extracellular K^+ concentration will cause an impairment in the ionic homeostasis of TILs, leading to an increase in their intracellular K^+ concentration (from ~130 mM to 150-160 mM when the extracellular K^+ concentration was increased by 40-50 mM (134,135)). This high K^+ condition hinders T cells from correctly exerting their role, mostly by blocking the TCR-induced cascade of phosphorylations (135) and other pivotal metabolic pathways (136) (135). The removal of K^+ from the cytoplasm of tumor-infiltrating lymphocytes (TILs) reverts them to an unimpaired condition (135). This could be achieved either by overexpressing K^+ channels like $K_v1.3$ and $K_{Ca}3.1$, or by activating $K_{Ca}3.1$ with an enhancer molecule like 1-EBIO (135) or SKA-346 (137). Because of this groundbreaking discovery, Chandy and Norton proposed the positive modulators of Ca^{2+}-activated K^+ channels as potential drugs capable of rescuing lymphocyte functions in impaired tumoral milieux (138).

Necrotic and dying tumor cells also release their intracellular ATP, whose concentration is normally 2-10 mM in the cytosol (139,140). Contrariwise, the extracellular concentration of ATP is rather low: in normal pancreas, for example, it is ~100 nM (141), but it rises to 10 μM in case of cancerous transformation (141) (in other organs it has been reported to generally be ~10 nM (140), which becomes hundreds of micromolars in case of ovarian carcinoma and melanoma (142)). ATP concentration will increase in parallel with tumor progression (129). The more ATP pours out of the cells, the more AMP and adenosine accumulate in the tumoral stroma thanks to two enzymes, CD39 and CD73, which are overexpressed in pancreatic ductal adenocarcinoma (PDAC) (143,144) and other cancers (145,146) and which catalyze the reaction ATP → AMP → adenosine. Adenosine, which normally has a concentration of ~13 nM in the human blood (147), can rise to 10 μM in the tumoral microenvironment (148). This has a great impact on tumor-infiltrating lymphocytes (TILs), which are known to host several adenosine receptors with a predominance of $A_{2A}R$ (149). Conforti's team carefully analyzed the impact of head and neck squamous cell carcinoma (HNSCC) on the K^+ channels of circulating and infiltrating T cells. While $K_v1.3$ currents measured in circulating T cells obtained from cancer patients and healthy subjects are very similar (150,151), $K_v1.3$ currents measured in biopsy-derived TILs are significantly lower. Moreover biopsy-derived TILs stop proliferating and producing cytotoxins like granzymes and cytokines like IL-2 (150). On the contrary, compared to healthy subjects, $K_{Ca}3.1$ currents are less prominent in peripheral $CD8^+$ T cells of cancer patients (151) and this is not due to a decrease in the surface expression of the channel (113,151). Peripheral $CD8^+$ T cells obtained from tumor-bearing patients seem unable to upregulate their CaM level after being activated, resulting in less coupling of CaM with $K_{Ca}3.1$ in the plasma membrane and, therefore, lower $K_{Ca}3.1$ activation and smaller currents (113). Even if the mere lack of intracellular CaM does not alter the production of cytokines like IFN-γ [49] and the mere presence of extracellular adenosine has only a small impact on the motility of normal T cells (113,151), the two conditions together create a synergistic effect that hinders the motility of T cells and limits their ability to correctly respond to chemotactic stimuli induced by CXCL-12 (113). Thus, the binding of adenosine to $A_{2A}R$, which triggers the activation of the cAMP-PKA cascade (152), has a detrimental effect mostly if the T cell is already impaired in its $K_{Ca}3.1$ activity because of the lack of CaM. However, it is not known yet why T cells obtained from cancer patients display downregulated CaM content. In addition, adenosine acts as a $K_{Ca}3.1$ blocker and it can quickly and temporarily block the $K_{Ca}3.1$ current, but the molecular mechanism of the block is still unclear (152). The inhibition of $K_{Ca}3.1$ by adenosine in the tumoral microenvironment could contribute to the detrimental effect on anti-

cancer immunity that has been already described. Just like Eil et al. demonstrated that the imbalance of intracellular K^+ can be pharmacologically salvaged using $K_{Ca}3.1$ activators (135,137), Conforti's team showed that an activator like 1-EBIO can rescue the $K_{Ca}3.1$ currents and consequently restore the motility of HNSCC $CD8^+$ T cells (113,151), strengthening the possibility of using these drugs as potential aids in immune-compromised environments like the tumor one.

2.2.6 The tumor microenvironment and acidosis

Besides the accumulation of adenosine and K^+ ions, the TME is also characterized by a severe dysfunction of the pH homeostasis (153). Solid cancers, in particular, because of their stiffness and rapid growth, soon face hypoxia and nutrient deprivation. Cancer cells counter this unlivable environment switching towards a more glycolysis-dependent metabolism and triggering the so called "Warburg effect" (154). The physiological extracellular pH (pH_e) of human tissues is around 7.2-7.5, but the large amount of lactate and H^+ released during the cancer growth drive it towards values of 6.5-6.9 (155,156). On the other hand, the usual intracellular pH does not steer away from 6.9-7.2 (157), but in cancer cells it can reach more alkaline values, hitting 7.3-7.6 (158), hence reversing the physiological pH gradient (from $pH_e > pH_i$ to $pH_e < pH_i$) (159). The pH_e in PDAC for example, which is one of the stiffest and most malignant carcinomas can reach a pH of 6.4 after just 7 days of growth in mice (160). Similarly, the pH_e in breast cancer implanted in mice can reach values between 6.3 and 6.9 and liver cancer has an average pH_e of 6.8-6.9, which is lower compared to 7.1-7.2 of their healthy counterparts (155). The alteration of the extracellular pH can directly affect the behavior of T cells *in loco* (161). Decreasing the extracellular pH to 6.5-6.6 will temporarily impair the activation and the proliferation of both human and murine T cells, mostly because of the down-regulation of the TCR proteins, causing less IL-2, IFN-γ and TNF-α production (162,163) and a decreased perforin- and granzyme-based cytotoxic activity (164). In this way the tumor forges a double-edged sword: on one side the extracellular acidity promotes certain malignant traits of the tumor itself, like epithelial-to-mesenchymal transition (165), motility and migration (166) and overall metastatic tendencies (167); on the other side the immune system, mostly represented by $CD8^+$ T cells, is suppressed and immobilized because of its inability to cope with the acidic environment. Even if not directly proven, it is also possible that extracellular acidosis aids certain pro-tumoral immune cells in promoting the release of matrix metalloproteinases (MMPs) (168), enzymes that reshape the TME in favor of the tumor itself. Among the many ways with which MDSCs help the tumor growth there is the secretion of MMPs (169), which has also been strictly linked to the expression of H_v1 (170). Therefore, it does not come as a

surprise that we and another team (101) discovered that MDSCs express mostly only H_v1 as a plasma membrane ion channel.

2.2.7 The effects of acidity on K^+ channels of immune cells

Ion channels, as proteins, are sensitive to different kinds of stresses. Some of them respond to mechanical inputs (171), many to changes in temperature (172) and others to pH variations (173). $K_v1.3$, along with other K_v channels (174), is very sensitive both to temperature and pH. Increasing the temperature from 5 to 42 °C has a positive effect on the conductance and the open probability of the channel and causes a dramatic acceleration in its activation, inactivation, and recovery kinetics as well (175). Similarly, an increase in the whole-cell current and acceleration in the activation and inactivation kinetics of $K_v1.3$ can be observed when the extracellular solution shifts from an acidic pH of ~5 to a basic pH of ~8 (176). On the other hand, intracellular pH variations have a big impact on the amplitude of $K_v1.3$ currents, but not on their kinetics (176). Despite being as important as $K_v1.3$, $K_{Ca}3.1$ has been less studied and almost nothing is known about how pH_e and pH_i influences these currents. Nothing is known either about the sensitivity of its positive modulators to pH_e and pH_i. If $K_{Ca}3.1$ enhancers like Riluzole, 1-EBIO or one of the many other similar substances are intended for use to boost the anergic immune system in the tumoral milieu, it must be known whether a perturbed pH could dampen or potentiate the effect of such drugs.

3 AIMS OF THE STUDY

3.1 Isolation and ion channel characterization of murine tumor-associated myeloid-derived suppressor cells

MDSCs are a common component of the immunosuppressive tumor microenvironment. Although the channelome to most immune cells is well characterized, the ion channel expression and the function of ion channels in MSDSc was not known. To address this, we inoculated Lewis Lung Carcinoma cells subcutaneously in mice and collected MDSCs for electrophysiological studies. Our aims were:

1. To isolate MDSCs from freshly excised tumors and categorize them into subfamilies through flow cytometry and immunofluorescence.
2. To characterize the ion channel repertoire of MDSCs subfamilies through patch-clamping, and define the biophysical (kinetics, pH sensitivity) and pharmacological properties of the measured ion currents.

3.2 Analysis of the sensitivity of $K_{Ca}3.1$ and of its positive modulators Riluzole and SKA-31 to intracellular and extracellular pH variations

$K_{Ca}3.1$ is an important ion channel in the immune system and has a role in promoting anti-cancer immunity. Moreover, several enhancers of its activity have been proposed as possible useful tools against cancer. Extra- and intracellular pH regulation is dramatically altered in cancer, however, neither the pH sensitivity of $K_{Ca}3.1$ nor that of $K_{Ca}3.1$ activators is known. To address these our aims were:

1. To characterize the sensitivity of $K_{Ca}3.1$ to intra- and extracellular pH combinations both using peripheral blood lymphocytes and transfected CHO cells.
2. To characterize the sensitivity of the positive modulators Riluzole and SKA-31 to intra- and extracellular pH combinations

4 MATERIALS AND METHODS

4.1 Cell cultures

Human venous blood from anonymized healthy donors was obtained from a blood bank. The peripheral blood lymphocytes (PBLs) were isolated through Histopaque1077 (Sigma-Aldrich Hungary, Budapest, Hungary) density gradient centrifugation. Cells obtained were resuspended in RPMI 1640 medium containing 10% fetal calf serum (Sigma-Aldrich), 100 µg/mL penicillin, 100 µg/mL streptomycin, and 2 mM L-glutamine, seeded in a 24-well culture plate at a density of 5 x 10^5 cells per mL, and grown in a 5% CO_2 incubator at 37°C for 2–5 days. Phytohemagglutinin A (PHA, Sigma-Aldrich) was added in 5, 7 or 10 µg/mL concentrations to the medium to boost the K^+ channel expression.

Chinese hamster ovary (CHO) cells (gift from Yosef Yarden, Weizmann Institute of Science, Rehovot, Israel) were maintained by culturing in Dulbecco's modified Eagle medium (DMEM, Gibco) supplemented with 2 mM L-glutamine, 10% FBS, 100 µg/mL streptomycin and 100 U/mL penicillin G (Sigma-Aldrich) at a density of $0.5 - 1 \times 10^6$ cells per mL in a humidified incubator at 37°C and 5% CO_2. Cells were passaged 3 times in a week following a 2–5 min incubation in 0.05% trypsin-EDTA solution at 37°C. Cultures were used up to passage number 20. PCR-based tests were routinely used to detect mycoplasma infection, only mycoplasma-free cultures were used for experiments.

CHO cells (that do not express endogenous voltage-gated ion currents (177)) were transiently transfected with the following plasmids encoding hK_{Ca}3.1 and turboGFP in a pCMV6-AC-GFP (OriGene Technologies) vector; H192A-hK_{Ca}3.1 in a pEGFP-C1 vector (a kind gift from Bernard Attali, Tel Aviv University, Israel); hK_{Ca}2.2 in a pCDN3 plasmid (a kind gift from Bernard Attali, Tel Aviv University, Israel) and T79D-rCaM in a pcDNA3 plasmid (a kind gift from Bernard Attali, Tel Aviv University, Israel). TurboGFP is a modified version of ppluGFP2, derived from *Pontellina plumata*, and is characterized by a fluorescence up to three times higher than EGFP (178). Transfections were performed using the Lipofectamine 2000 kit (Invitrogen, Carlsbad, CA) following the manufacturer's protocol. The cells were grown under standard conditions (see CHO cell culturing). GFP-positive transfectants were identified using Nikon TMS fluorescence microscope (Nikon, Tokyo, Japan), and currents were recorded 24 to 48 h post transfection.

CH12 B cell lymphoma cells were grown in RPMI 1640 medium supplemented with 10% FBS, 1% GlutaMAX, 1% penicillin-streptomycin. The Lewis lung carcinoma cell line (LLC) was a kind gifts from László Nagy (Department of Biochemistry and Molecular Biology,

Faculty of Medicine, University of Debrecen, Hungary). Cells were grown in RPMI 1640 medium supplemented with 10% FBS, 1% GlutaMAX, and 1% penicillin-streptomycin.

4.2 Tumor model and cell sorting

LLC cells (3×10^6/0.1 mL PBS) were injected subcutaneously on the right flank of syngeneic 8- to 12-week-old male C57BL/10 wild-type mice. Tumors were excised and cut into small pieces in isolation buffer (RPMI 1640 medium) followed by protease digestion using enzyme mixture (collagenase I (CLSS-1, Worthington, Columbus, OH, USA, 10 U/mL), collagenase IV (CLSS-4, Worthington, 400 U/mL), and DNase I (DCLS, Worthington, 30 U/mL)) for 30 min at 37°C. Cells were filtered through a 70 μm strainer and the red blood cells were lysed in ACK (Ammonium Chloride Potassium) lysing buffer. After washing and spinning, cells were resuspended in Hanks' Balanced Salt Solution (HBSS) buffer and stained with live/dead stain (Fixable Viability Dye eFluor 506, eBiocience, San Diego, CA, USA, 1 μg/mL) in HBSS for 30 min at 4°C to exclude the dead cells. After washing, cells were preincubated in MACS buffer (phosphate buffered saline (PBS) pH 7.2, supplemented with 0.5% BSA and 2 mM EDTA) with rat anti-mouse CD16/CD32 FcγR blocking antibody (for 5 min at 4 °C and stained for 30 min at 4°C with appropriate antibodies, in order to sort the PMN-MDSCs and Mo-MDSCs, using BD FACSAria III sorter (BD Biosciences, San Hose, CA, USA). Details regarding the antibodies, flow cytometry and sorting are in the original publication as this analysis is not part of the dissertation (179).

4.3 Western blot

The sorted cells were lysed in 2x Laemmli buffer supplemented with proteinase (Sigma/Merck KGaA, Darmstadt, Germany, cat #P8340) and phosphatase inhibitor (Sigma, cat #P5726) cocktail followed by a denaturation step at 98°C for 5 min. Fifteen μg protein per sample was run on 7.5% polyacrylamide gel and transferred to a nitrocellulose membrane (Bio-Rad Laboratories, Hercules, CA, USA). The non-specific binding sites were blocked by incubating the nitrocellulose membrane in 5% w/v non-fat dry milk in Tris-Buffered Saline (TBS) supplemented with 0.2% v/v Tween (TBST) for 1 h. Next, the nitrocellulose membrane was incubated with primary antibodies (anti-H_v1 and -β-actin) diluted in 2.5% w/v non-fat dry milk in TBST overnight at 4 °C. After washing for 3 × 7 min in TTBS, the nitrocellulose membrane was incubated with donkey anti-rabbit IgG-HRP linked secondary antibody for detection of H_v1 protein. Sheep anti-mouse IgG-HRP linked secondary antibody was used for the detection of actin. The chemiluminescence signal was detected using an Azure c300 Gel Imaging System (Azure Biosystems, Dublin, CA, USA). CH12 B cell lymphoma lysate was used as a positive control. The Western blot analysis was performed on sorted cells from 3

different experiments. The relative H_v1 protein level was calculated using Azure Spot Pro Analysis software and expressed as H_v1/actin ratio.

4.4 Electrophysiology and pharmacology

Electrophysiology measurements were carried out using the patch-clamp technique in voltage-clamp mode. Whole-cell currents were recorded using a Multiclamp 700B amplifier connected to a DigiData 1440A digitizer (Molecular Devices, Sunnyvale, CA, USA). Micropipettes were pulled from GC 150 F-15 borosilicate capillaries (Harvard Apparatus Kent, UK) resulting in 3 to 5 MΩ resistance in the bath solution. Current traces were lowpass-filtered through the built-in analog 4-pole Bessel filters of the amplifiers and sampling frequency was set at least twice the filter cutoff frequency. Currents are either shown as absolute values or expressed as current density obtained by dividing the currents measured in pA with the cell capacitance in pF to yield pA/pF. Recordings were carried out at room temperature (20–25°C), The patch-clamped cell was perfused with control and test solutions using a gravity-driven custom-built perfusion system and excess bath solution was removed constantly by vacuum suction.

4.4.1 Recording whole-cell currents in murine PMN- and Mo-MDSCs

Voltage ramps (2000 ms long from −60 mV to +150 mV, every 15 s) were used to demonstrate qualitatively the dependence of the activation threshold of the H_v1 currents at various pH_e values. Traces were filtered (lowpass boxcar, 25 smoothing points), off-line leak-corrected manually point-by-point. Linear regression line was fit to the data points below the activation threshold of the H^+ current (between 50 ms to 330 ms, corresponding to −60 mV and −30 mV) and the fitted parameters were used to subtract the non-specific leak. The leak-corrected currents between +145 mV and +146 mV were extracted, averaged, and considered as the peak current. The average currents of two or three stable traces at a given pH_e condition defined one data point.

The current–voltage (I–V) relationships and the activation threshold voltage of the currents (V_{thr}) were determined using 2 s long step depolarizations from a holding potential of −80 mV to +100 mV in +10 mV increments. The protocol was applied every 15 s; the sampling rate was 5 kHz. For the I-V curves, every trace was filtered (lowpass boxcar, 25 smoothing points) and leak-corrected manually. Peak currents were calculated as the average of the last 18 points (i.e., between 2051.1 and 2051.9 ms) at the end of the depolarizing pulses. For the V_{thr} determination, leak correction was performed using the first 5 (pH_e 7.4), 7 (pH_e 6.4 and 6.2), and 10 peak currents of the I-V relationship (i.e., between −80 and −50/−30/+10 mV) and the

SD was calculated using the first 5 values in the I-V (i.e., between −80 and −50 mV). The V_{thr} was selected as the membrane potential at which the current was above 2 × SD.

For recording tail currents, the H_v1 current was fully activated using 500 ms long single-step depolarizations from a holding potential of −80 mV to +100 mV. The tail currents were recorded upon stepping back from this potential in 20 mV decrements to −60 mV, and the currents were recorded for 250 ms at the back-step potentials. The protocol was applied every 15 s with a sampling rate of 20 kHz. The traces were leak-corrected manually and filtered (lowpass boxcar, 25 smoothing points). To test the presence of voltage-gated K^+ currents, 15 ms long depolarization steps were applied to +50 mV from a holding potential of −100 mV every 15 s, with a sampling rate of 20 kHz. Voltage ramps, as specified above, were also used to study the presence of voltage-gated ion currents in MDSCs over an extended membrane potential range and depolarization duration in physiological salt solutions.

4.4.2 Recording whole-cell $K_{Ca}3.1$ currents in peripheral blood lymphocytes and transfected CHO cells

The cells were held at −85 mV holding potential to minimize the holding current and allow the calculation of the leak conductance. 150-ms-long voltage ramps (from −120 to +50 mV, in 150 ms) were applied every 10 s to evoke the $K_{Ca}3.1$ currents.

For offline leak correction and the calculation of the K^+ conductance a Python based custom written program was used. The algorithm averaged the holding current (I_{hold}) for n=600 data points at –85 mV, which is close to the K^+ equilibrium potential calculated from the Nernst equation (E_K= –89 mV). I_{hold} was considered as leak current and used to calculate G_{leak} as I_{hold}/–85 mV. Every data point was corrected for linear leak using $I_K=I_m – (G_{leak}\times E_m)$, where I_K is the leak subtracted K^+ current, I_m is the measured membrane current at E_m membrane potential. I_K was then displayed as a function of E_m during the ramp and the region for linear current-voltage relationship was selected and G_K was calculated as the slope of the straight line fitted to the I_K data points ($G_K = \Delta I_K/\Delta V$). The linear region was typically between –120 mV and –60 mV for lymphocytes, at more depolarized membrane potentials the activation of the $K_v1.3$ current caused a significant deflection from the linear I-V relationship.

The following parameters were derived from the leak subtracted G_K data:

$G_{K,200}/G_{K,0}$: ratio of the K^+ conductances determined at a time point t >200 s ($G_{K,200}$) in standard extracellular solution (S-ECS) over G_K at the beginning of the experiment (0 s) in S-ECS ($G_{K,0}$) in the absence of $K_{Ca}3.1$ activators;

$G_{K,x}/G_{K,7.4}$: normalized conductance, G_K values determined in various pH_e solutions ($G_{K,x}$, where x is the pH_e) in a given cell normalized to $G_{K,7.4}$ recorded at pH_e=7.4 in the same cell;

$G_{K,act}/G_K$: "fold increase in conductance", K^+ conductance measured in the presence of the activator at a given concentration ($G_{K,act}$) divided by the K^+ conductance in the drug-free solution (G_K)

"fold increase normalized to 7.4": "fold increase in conductance" caused by the activator at a given pH_i and pH_e combination normalized to the "fold increase in conductance" measured with the activators in S- ECS at pH_e=7.4.

$G_{K,end}/G_{K,start}$: $G_{K,end}$ and $G_{K,start}$ are the activator-enhanced K^+ conductance at the end of the experiment (≥ 800 s) and the activator-enhanced K^+ conductance at the beginning of the experiment, respectively.

The activator concentration-response curves were fit using:

$$\text{fold increase in conductance} = \text{Bottom} + \frac{(Top-Bottom)\times[X]^{n_H}}{[X]^{n_H}+EC_{50}{}^{n_H}}$$

where "fold increase in conductance" is defined above, [X] is the activator concentration, EC_{50} is the concentration of agonist that gives a response halfway between Bottom (min value of "fold increase in the conductance") and Top (maximum value of the "fold increase in conductance"), and n_H is the Hill slope.

4.4.3 Data acquisition and analysis tools

The pClamp 10.5, 10.7, and 11.2 software packages were used to acquire the data. The pClamp 10.7 and 11.1 software packages (Molecular Devices Inc., Sunnyvale, CA, USA) were used to analyze the data. Statistical analyses were performed with GraphPad Prism 8.4.3 (GraphPad Software, Inc., San Diego, CA, USA). Bar graphs represent mean ± SEM, the individual data points used for the calculation of the mean are displayed in all bar graphs. The number of independent observations is indicated as a number in the bar or stated in the figure legends.

Statistical comparisons were performed using the following principles. Data were tested for normal distribution, and parametric test were used only if normality test (Kolmogorov-Smirnov test) passed at $p > 0.05$. When two groups were compared Student's t test was used given equal variances of the two groups. If equal variance test (F test, $p = 0.05$) failed then t-test was performed with Welch's correction. When multiple groups were compared one-way ANOVA was applied. If groups were statistically different ($p < 0.05$) then groups different from others were isolated using all pairwise multiple comparisons with Bonferroni correction. Single

normalized datasets (e.g. **Figure 23D**) were analyzed using one-sample t-test (against H_0: $\mu_0 = 1$ hypothesis). In general, normalized datasets were tested using against H_0: $\mu_0 = 1$ hypothesis. The p values used for decision making are indicated by asterisks (*p < 0.05, **p < 0.01, ***p < 0.001, ****p < 0.0001., n.s.: p > 0.05).

Linear regression was performed using the built-in algorithm of Prism (simple linear regression) and the goodness of fit was evaluated by R^2 (e.g. **Figure 13**) The built in algorithm of Python was used an when the slope of the current-voltage relationship was determined to obtain conductance (e.g. conductances obtained from the insets of **Figure 16A** and displayed in **Figure 16B**) directly from the Axon ABF data (see 4.4.2).

The built in non-linear least square algorithm of Prism without weighting was used to fit the concentration-response curves in **Figure 18**. The parameters of the 4-parameeter Hill equation were constrained to $EC_{50} > 0$ and "bottom" > 0. The goodness of fit was evaluated by R^2.

4.5 Solutions

The standard extracellular solution used to study H_v1 (for a quick recapitulation see **Table 1**) at $pH_e = 7.4$ contained 180 mM HEPES, 75 mM N-Methyl-D-Glucamine (NMDG), 15 mM glucose, and 3 mM $MgCl_2$ (titrated with CsOH), whereas in the extracellular solutions at pH_e = 6.4/6.2/5.7, 180 mM HEPES buffer was substituted with 180 mM MES (2-(N-morpholino)ethanesulfonic acid, titrated with CsOH or HCl). The standard intracellular solution at $pH_i = 6.2$ contained 180 mM MES, 75 mM NMDG, 15 mM glucose, 3 mM $MgCl_2$, and 1 mM EGTA (ethylene glycol-bis(β-aminoethyl ether)-N,N,N',N'-tetraacetic acid, titrated with CsOH). To explore the presence of other voltage-gated currents, we used a Na^+-based extracellular solution at pH_e = 7.35 containing 145 mM NaCl, 5 mM KCl, 1 mM $MgCl_2$, 2.5 mM $CaCl_2$, 5.5 mM glucose, and 10 mM HEPES and a K^+-based intracellular solution at pH_i = 7.22 containing 140 mM KF, 2 mM $MgCl_2$, 1 mM $CaCl_2$, 10 mM HEPES, and 11 mM EGTA. The pH of the solutions was checked before every experiment, and all salts and components of the solutions were purchased from Sigma-Aldrich Budapest, Hungary.

The S-ECS used to study K_{Ca} channels (for a quick recapitulation see **Table 2**) was a Na^+-aspartate (Na^+Asp^-)-based solution with 2.5 mM $CaCl_2$, and 10 mM HEPES titrated to pH_e=7.4 with NaOH. The extracellular solution having pH_e=8.0 (8.0-ECS) was buffered with 10 mM HEPES whereas those having pH_e=6.0 (6.0-ECS); pH_e=6.5 (6.5-ECS) or pH_e=6.9 (6.9-ECS) were buffered using 10 mM MES, pH was titrated to the desired value with NaOH. The standard intracellular solution (S-ICS) was a K^+-aspartate (K^+Asp^-)-based solution with 8.5 mM $CaCl_2$, 10 mM EGTA and 10 mM HEPES (titrated to pH_i=7.2 with Tris). This solution has an estimated free Ca^{2+} concentration of ~1-2 μM based on the MaxChelator program WEBMAX-

C software (C. Patton, Stanford University, retrieved here: https://somapp.ucdmc.ucdavis.edu/pharmacology/bers/maxchelator/webmaxc/webmaxcE.htm). Since pH has a strong effect on the affinity of EGTA for Ca^{2+} we substituted EGTA with BAPTA, a less pH-sensitive Ca^{2+} chelator (180), when the pH of the intracellular solution was titrated to various levels. To keep the free Ca^{2+} concentration around ~1-2 μM the pipette-filing solution titrated to pH_i=6.5 (6.5-ICS) contained 11 mM BAPTA whereas the one titrated to pH_i=8.0 (8.0-ICS) contained 10 mM BAPTA. For the experiments in which we used the $K_{Ca}3.1$ activators at pH=7.2 we set the free Ca^{2+} concentration in the pipette-filing solution to ~250 nM (7.2-ICS-250), as suggested by (181) and Ca^{2+} was buffered using EGTA (10 mM EGTA and 5.7 mM $CaCl_2$). When the pH of the pipette-filling solution, with 250 nM Ca^{2+} concentration, was set to pH_i=6.5 (6.5-ICS-250) or pH_i=8.0 (8.0-ICS-250) the amount of BAPTA was set to 10 mM, but the concentration of $CaCl_2$ was adjusted to reflect the pH-dependence of the buffer capacity of BAPTA. More precisely, in case of pH_i=6.5 we used 3.25 mM $CaCl_2$ and for pH_i=8.0 we used 4.3 mM $CaCl_2$. All pipette-filling solutions were titrated with Tris. All titrations were done at 25°C and the pH of solutions was checked before every experiment.

	Extracellular	Intracellular	Na^+/K^+ extracellular	Na^+/K^+ intracellular
NMDG	75	75	-	-
NaCl	-	-	145	-
KF	-	-	-	140
KCl	-	-	5	-
$MgCl_2$	3	3	1	2
$CaCl_2$	-	-	2.5	1
Glucose	15	15	5.5	-
EGTA	-	1	-	11
HEPES	180*	-	10	10
MES	180*	180	-	-
pH	5.7/6.2/6.4/7.4 (w/ CsOH)	6.2 (w/ CsOH)	7.35 (w/ NaOH)	7.22 (w/ KOH)
Free Ca^{2+}	-	-	(2.5 mM)	(45 μM)

*Depending on their final pH, the solutions either contained HEPES (7.4) or MES (5.7/6.2/6.4).

Table 1. **Components of the intra- and extracellular solutions used for patch-clamping of H_v1 channels.**

	Standard Extracellular	Standard intracellular	Intracellular 8.0	Intracellular 6.5	Intracellular 6.5 w/ activators	Intracellular 7.2 w/ activators	Intracellular 8.0 w/ activators
Na^+Asp^-	145	-	-	-	-	-	-
K^+Asp^-	-	145	145	145	145	145	145
KCl	5	-	-	-	-	-	-
$MgCl_2$	1	2	2	2	2	2	2
$CaCl_2$	2.5	8.5	8.5	8.5	3.25	5.7	4.3
Glucose	5.5	-	-	-	-	-	-
HEPES	10*	10	10	-	-	10	10
MES	10*	-	-	10	10	-	-
EGTA	-	10	-	-	-	10	-
BAPTA	-	-	10	11	10	-	10
pH	6.5/6.9/7.4/8.0 (w/ NaOH)	7.2 (w/ Tris)	8.0 (w/ Tris)	6.5 (w/ Tris)	6.5 (w/ Tris)	7.2 (w/ Tris)	8.0 (w/ Tris)
Free Ca^{2+}	(2.5 mM)	~1 μM	~1-2 μM	~1-2 μM	~250 nM	~250 nM	~250 nM

*Depending on their final pH, the solutions either contained HEPES (7.4/8.0) or MES (6.5/6.9).

Table 2. **Components of the intra- and extracellular solutions used for patch-clamping of $K_{Ca}3.1$ channels.**

5 RESULTS

5.1 The voltage-gated H_v1 H^+ channel is expressed in tumor-infiltrating myeloid-derived suppressor cells

Myeloid-derived suppressor cells are a large component of the tumor milieu promoting tumor invasion and metastasis through several mechanisms (182). Even if the tumor microenvironment is very dynamic and ever-changing, it is usually characterized by hypoxia, nutrient poverty and acidity, features that do not seem to hinder MDSCs, which are able to adapt their metabolism to these extreme conditions, survive and act as pro-tumor agents (183). As a fact, tumor-derived lactic acid has been directly linked to positive regulation of MDSCs activity in murine pancreatic cancer (184). In this section of my dissertation, I will explain how we obtained fresh murine MDSCs, how we characterized them and determined their ion channel repertoire that may provide a tool for pH adaptation.

5.1.1 MDSCs are a large component of Lewis lung cancer

LLC, a murine model representing non-small cell lung carcinoma, is recognized for harboring a minimal count of $CD4^+$ and $CD8^+$ T lymphocytes, while boasting a significant presence of myeloid cells such as macrophages, neutrophils, and dendritic cells. This characteristic renders it immunologically classified as a 'cold' tumor (185). MDSCs were isolated from LLC-tumor-bearing mice according to Materials and Methods and MDSC subfractions were sorted using flow cytometry. This part of the analysis has been mainly conducted by Éva Korpos, Adrienn Gyöngyösi and other colleagues of the Department of Immunology of the University of Debrecen, hence it will be explained briefly. For details (antibody used, flow cytometry and sorting and confocal microscopy), please see the original publication (179).

Myeloid cells were identified using a combination of morphology, singlet, and viability gates in combination with the myeloid marker $CD11b^+$. In order to differentiate between the main two sub-populations (polymorphonuclear MDSCs and monocytic MDSCs) we used the markers Ly6G and Ly6C: PMN-MDSCs were defined as $CD11^+/Ly6G^+$ cells, while Mo-MDSCs as $CD11b^+/Ly6G^-/F4/80^-/MHCII^-/Ly6C^+$ cells. These two populations were not present with the same proportions: PMN-MDSCs were more abundant (60% of $CD11^+$ cells) and Mo-MDSCs less abundant (10% of $CD11^+$ cells). Since these cell surface markers are not unequivocally identifying MDSC sub-populations, but are also expressed by other immune cell types, the only way to define these cells as MDSCs is to carry out T cell proliferation suppression assays, defined by the specialists as the “gold standard” technique (186). We showed that Mo-MDSCs had suppressive capacity when they were co-cultured with murine

splenocytes in 1:1 and 1:2 ratios, whereas PMN-MDCSs failed to demonstrate immunosuppressive properties. Mo-MDSCs could suppress the proliferation of both $CD4^+$ and $CD8^+$ splenocytes. Interestingly, it is common to other tumor models the fact that the scarce population of Mo-MDSCs is also one of the most immunosuppressive, while the abundant PMN-MDSCs show less or no immunosuppressive activity (187).

5.1.2 Both tumor-derived Mo- and PMN-MDSCs express H_v1 at mRNA and protein level

Normally, both monocytes (188) and neutrophils (189) express H_v1, whose role is to support ROS production and maintenance of the intracellular pH homeostasis (190). Recently it has been shown that *in vitro* differentiated murine MDSCs express H_v1 as well (190). Inspired by this observation, we conducted qPCR to examine the expression of the H_v1 transcript in PMN- and Mo-MDSCs obtained from the LLC tumor (**Figure 8A**). Although both MDSC subpopulations showed H_v1 gene expression, we observed a higher level of expression in PMN-MDSCs compared to Mo-MDSCs. This pattern was consistent when we analyzed H_v1 protein levels using Western blotting (WB) (**Figure 8B, C**). To gain more insight into the *in situ* expression of H_v1 in MDSCs infiltrating the LLC tumors, Éva Korpos performed immunofluorescence staining of LLC tumor sections using the H_v1-specific antibody validated in WB analysis. As expected, the H_v1 signal was much stronger in PMN-MDSCs compared to Mo-MDSCs. PMN-MDSCs in the tumor showed focal distribution whereas the Mo-DSCSs are more sparsely distributed (**Figure 8D** (179)).

5.1.3 Ion currents in MDSCs

MDSCs acquired by cell sorting from the tumor mass underwent analysis via single-cell electrophysiology (patch-clamp) to assess the expression of whole-cell ion currents utilizing different combinations of intra- and extracellular solutions (**Figure 9**). Initially, we employed intracellular solutions based on K^+ and extracellular solutions based on Na^+, enabling the recording of voltage-gated K^+ and Na^+ currents. When either Mo- or PMN-MDSCs were subjected to 15 ms-long voltage steps from −100 mV holding potential to +50 mV test potential (**Figure 9A, C**), we could not detect any classical voltage-gated ion currents in the outward direction. On the other hand, using voltage ramps, we detected a voltage-gated outward current that activated at depolarized membrane potentials (**Figure 9B, D**) and was sensitive to the extracellular pH (**Figure 9B**). The presence of the proton current was observed more clearly when the recording solutions lacked conventional permeating cations and contained reduced Cl^- concentration to eliminate outward currents other than the proton current (using NMDG-

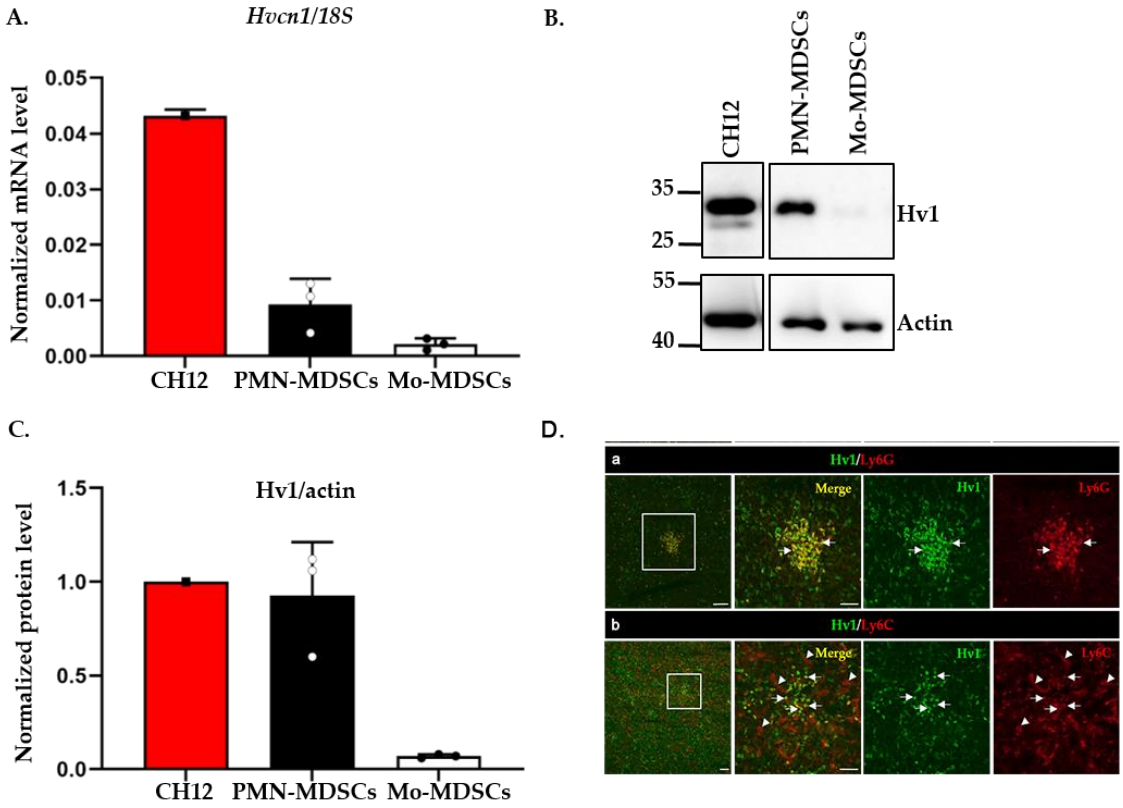

Figure 8. **Expression of H_v1 proton channel by murine PMN-MDSCs and Mo-MDSCs at mRNA and protein level**. (**A**) H_v1 RNA level relative to 18S RNA expressed by MDSCs using RT-qPCR. The individual data points (empty or filled circles) show the average of duplicates. RNA extracted from the CH12 B cell lymphoma cell line was used as a positive control. Bars and error bars indicate mean ± SD (PMN-MDSCs, n = 3; Mo-MDSCs, n = 3). (**B**) Western blot analysis of H_v1 proton channel protein from the sorted MDSCs: protein lysate from CH12 B cell lymphoma was used as a positive control and actin as a housekeeping protein. (**C**) Densiometric analysis of H_v1 protein level expressed by PMN- and Mo-MDSCs relative to actin expression. Densitometric data were obtained for 3 independent sets of sorted cells. Bars and error bars indicate mean ± SD (PMN-MDSCs, n = 3; Mo-MDSCs, n = 3). (**D**) Immunofluorescence staining of LLC cryosections to detect H_v1^+/$Ly6G^+$ PMN-MDSCs (a) and H_v1^+/$Ly6C^+$ Mo-MDSCs (b). Boxed areas in the 1st column are shown in higher magnification to the right. Scale bars: 100 µm for the lower and 50 µm for the higher magnification images. $Ly6G^+$ (red) marks PMN-MDSCs, $Ly6C^+$ (red) marks Mo-MDSCs, the H_v1 signal is in green. $Ly6C^+$-$Ly6G^+$/H_v1+ co-expressing myeloid cells are in yellow in the merged images (arrows). Ly6C additionally marks the blood vessels (arrowheads).

based solutions) and rich in non-volatile buffers in order to keep both pH_i and pH_e stable (**Figure 10A, B**).

5.1.3.1 Voltage-ramp analysis of the whole-cell H^+ currents in MDSCs

Voltage-ramp-evoked currents in **Figure 10** were recorded while the pH_i was maintained at 6.2 and the extracellular pH was changed to different values ranging from pH_e=5.7 to pH_e=7.4. The acidic pH_i was chosen for the recordings to mimic intracellular acidity that may happen in the TME (161). Moreover, this also facilitated the recordings as generation of the pH gradient across the membrane required to activate H_v1 could be achieved even at normal extracellular pH value. **Figure 10A, B** show several features characteristic of H_v1. First,

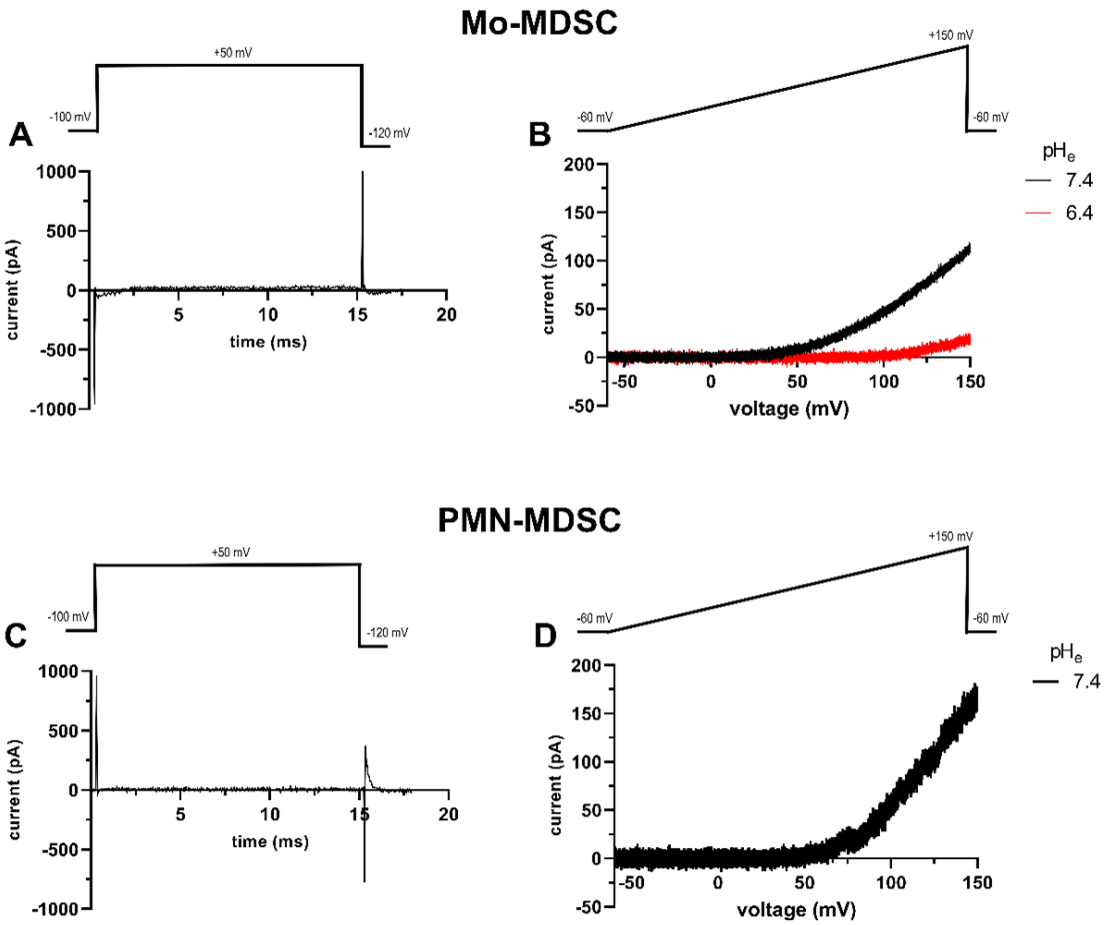

Figure 9. **Ion currents measured in Mo- and PMN-MDSCs**. Whole-cell patch-clamp records were obtained in Na^+-based extracellular and K^+-based pipette filling solutions. The pH of the pipette filling solution was pH_i=7.2 and that of the extracellular solution was pH_e=7.4 (black traces) or pH_e=6.4 (red trace). Voltages steps from the holding potential of -100 mV to +50 mV or voltage ramps from the holding potential of -60 mV to +150 mV were applied to elicit currents (see insets). Currents were recorded every 15 s. Representative current traces are shown for Mo-MDSCs (**A**, **B**), and for PMN-MDSCs (**C**, **D**).

the smaller the pH gradient across the membrane [$\Delta pH_{e-i} = (pH_e - pH_i)$] the more depolarized the V_{thr} (threshold voltage). V_{thr} was estimated in voltage-ramp experiments by the membrane potential at which the whole cell current deviated from leak (see later for more precise determination of the threshold potential). The estimated V_{thr} values for pH_e=7.4 and pH_e=6.4 are indicated in **Figure 10A, B** by arrows. The large difference in the V_{thr} values as a function of pH_e is clearly demonstrated for both types of MDSCs. Second: the larger the pH gradient, the larger the currents are at identical membrane potentials. Plotting the current of each sweep at +145 mV as a function of the sequentially numbered sweep numbers (the time interval between the sweeps is 15 s) shows that changing the extracellular pH induces rapid and reversible effects on the current amplitude (**Figure 10C, D**). Even if the capacitance measurements suggest that Mo-MDSCs are bigger than PMN-MDSCs (1.83 ± 0.14 (*n* = 40) vs.

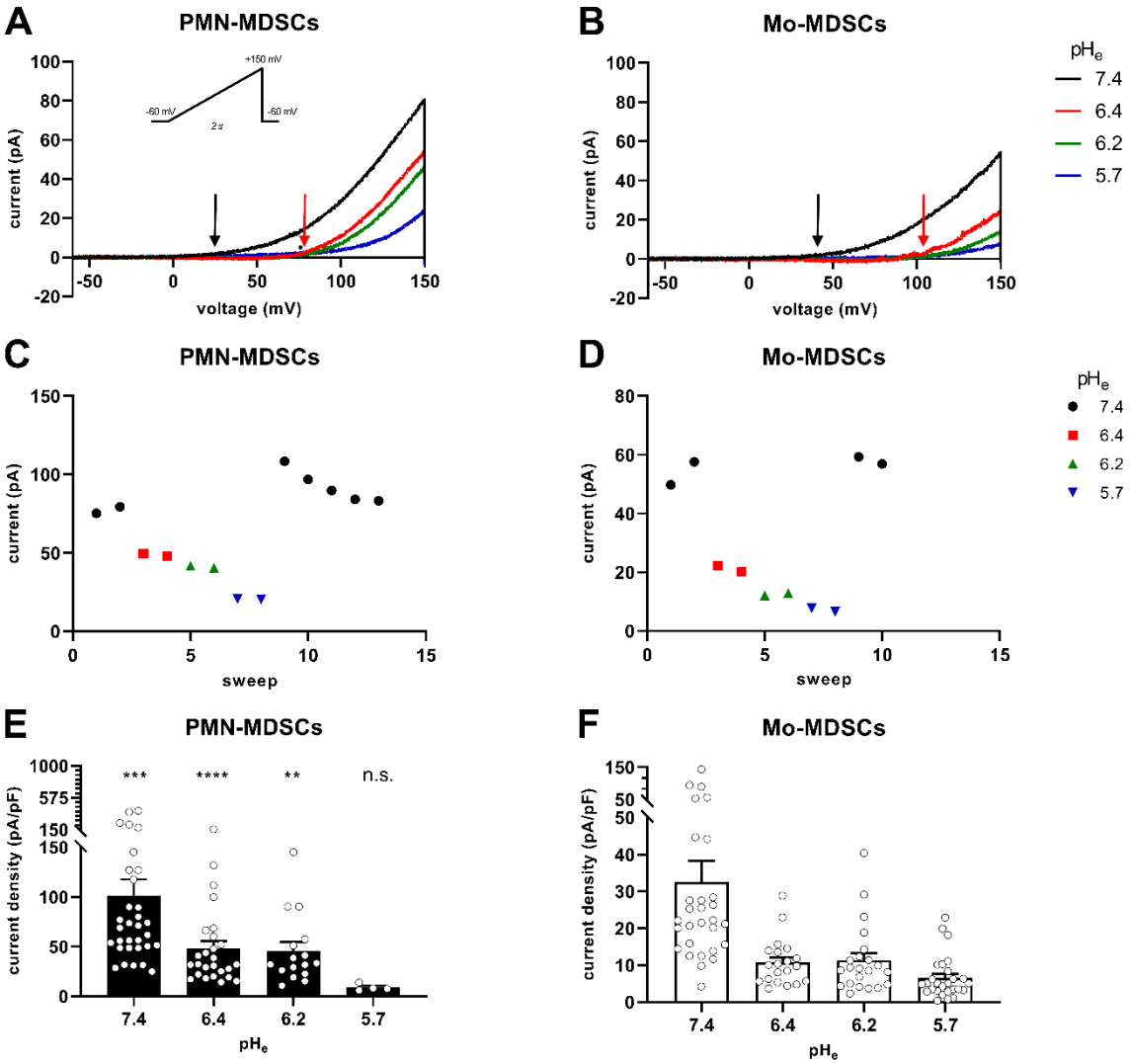

Figure 10. **pH_e-induced shift of H_v1 currents in murine PMN- and Mo-MDSCs**. (**A**–**D**) Representative whole-cell current traces evoked by voltage ramps ranging from −60 to +150 mV, lasting 2 s and repeated every 15 s (see inset) in a PMN- (**A**) and a Mo-MDSC (**B**) freshly isolated from murine LLC. The currents at +145 mV were determined for every trace (see Materials and Methods) and plotted as a function of the sweep number. The arrows indicate approximately the V_{thr} for two conditions (pH_e = 7.4 (black) and 6.4 (red)). Currents obtained at different pH_e values for PMN- (**C**) and Mo-MDSCs (**D**) are represented by different colors and symbols (black circle: pH_e 7.4; red square: 6.4; green up triangle: 6.2; blue down triangle: 5.7). (E, F) Current density was calculated as the ratio of the current at +145 mV and the capacitance of the cell in pF determined from the readout of the amplifier whole-cell capacitance compensation circuit for each cell individually. Bars and error bars indicate the mean ± SEM (PMN-MDSCs–7.4: n = 32, 6.4: n = 26, 6.2: n = 16, 5.7: n = 4; Mo-MDSCs–7.4: n = 29, 6.4: n = 20, 6.2: n = 22, 5.7: n = 27) of the current densities of PMN- (E) and Mo-MDSCs (F) obtained at different pH_e values as indicated. Data between PMN- and Mo-MDSCs for every pH_e condition were compared via Student's unpaired t-test with Welch's correction and indicated in (E) (**, $p < 0.01$; ***, $p < 0.001$; ****, $p < 0.0001$).

3.13 ± 0.14 pF (n = 39), mean ± SEM, $p < 0.0001$), the H^+ current density in PMN-MDSCs was ~3 times bigger compared to Mo-MDSCs at pH_e = 7.4 (**Figure 10E, F**).

5.1.3.2 Voltage-step analysis of the whole-cell H^+ currents in MDSCs and the quantitative determination of the threshold potential for activation

The V_{thr} shift can be quantitatively inferred from the current–voltage relationships shown in **Figures 11** and **12**. The families of whole-cell currents in **Figure 11 A-D** were obtained in a single PMN-MDSC upon applying 2000 ms-long step voltage depolarizations in 10 mV increments. The intracellular pH was maintained at pH_i=6.2 and the extracellular pH ranged from pH_e=7.4 (**Figure 11A**) to pH_e=5.7 (**Figure 11D**) with 6.4 (**Figure 11B**) and 6.2 (**Figure 11C**) as intermediate values. While larger depolarizations resulted in currents with quicker activation kinetics, 2 s-long pulses did not suffice to achieve current saturation. This phenomenon is commonly observed in H_v1 currents (76). The same experiments, with the same extra- and intracellular pH, were done on Mo-MDSCs.

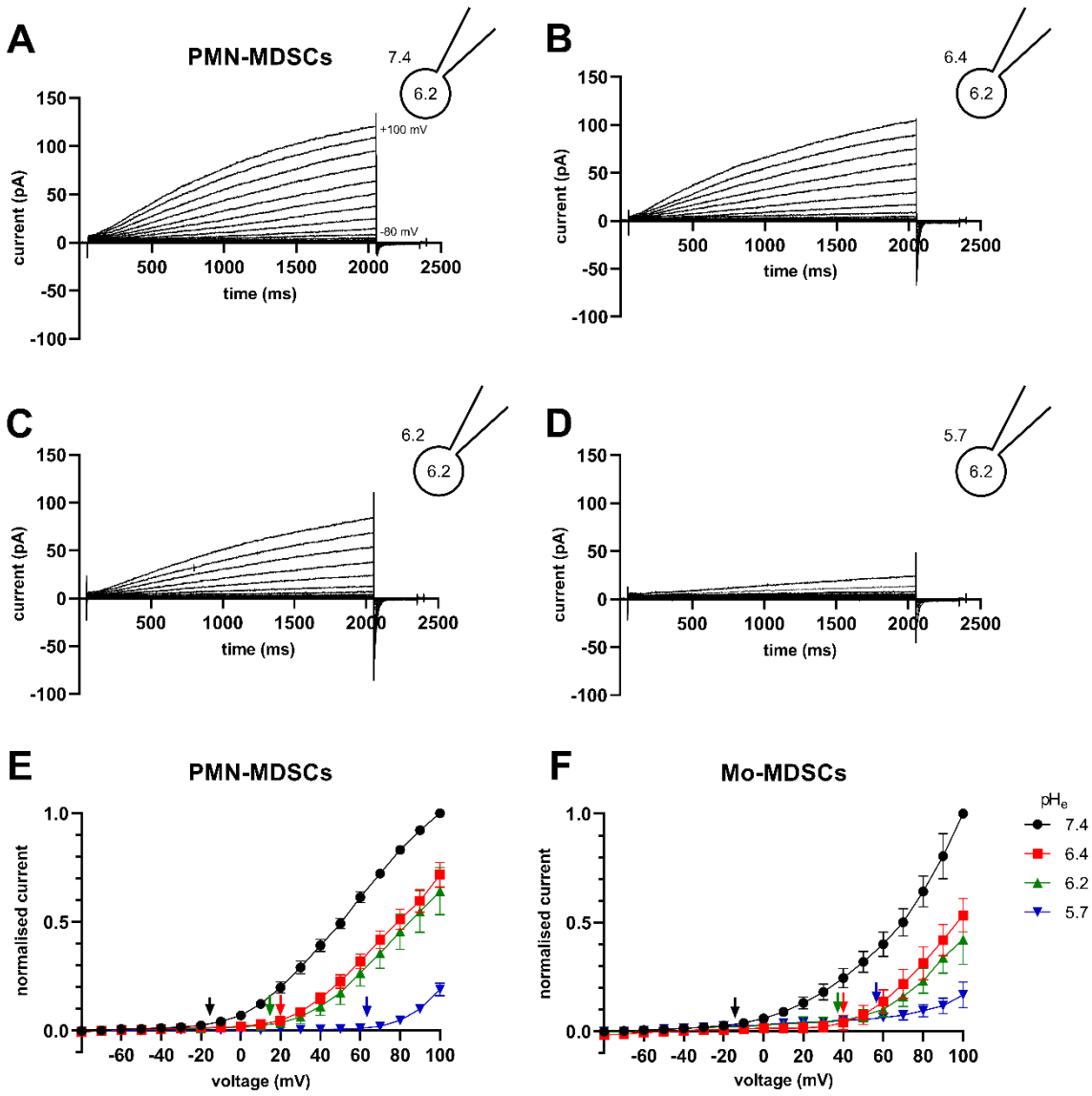

Figure 11. **Families of H^+ currents and I-V curves in murine PMN- and Mo-MDSCs**. (**A**–**D**) Representative family of whole-cell H^+ currents in murine PMN-MDSCs isolated freshly from LLC. Depolarizing 2 s long pulses

were applied from a holding potential of −80 mV to +100 mV in 10 mV increments. While the internal solution was maintained constantly in the micropipette at pH_i 6.2, the cell was locally perfused at different pH_e (7.4 (**A**), 6.4 (**B**), 6.2 (**C**) and 5.7 (**D**)). Representative of 11 (**A**), 8 (**B**), 4 (**C**) and 3 (**D**) similar families of currents. Every trace has been filtered with a 25-point boxcar filter. (**E**, **F**) I–V curves for PMN- (**E**) and Mo-MDSCs (**F**) were built using the peak currents of every trace in every condition (black: pH_e 7.4; red: 6.4; green: 6.2; blue: 5.7) normalized to their respective current at +100 mV/pH_e = 7.4. The V_{thr} for every pH_e condition was calculated (see Materials and Methods, data analysis) and subsequently pointed out in the plot using an arrow with the associated color. Every value with its error bar indicates the mean ± SEM ((**E**)–7.4: n = 10–11, 6.4: n = 7–8, 6.2: n = 4, 5.7: n = 3. (**F**)–7.4: n = 5–9, 6.4: n = 4, 6.2: n = 2–4, 5.7: n = 4–5). The representative traces of Mo-MDSCs (**F**) are in **Figure 12**.

The whole-cell currents recorded in Mo-MDSCs (**Figure 12A-D**) showed similar features to the ones recorded in PMN-MDSCs (**Figure 11**). **Figure 11E, F** show the average normalized peak currents as function of the membrane potential obtained at four pH_e values. The shift of the I-V to more depolarized membrane potentials with the decrease in the pH_e is markedly demonstrated for both PMN-MDCs (**Figure 11E**) and Mo-MDSCs (**Figure 11F**). The V_{thr} values were determined for each cell individually from the peak current-voltage using the statistical criteria explained in detail in the Materials and Methods and indicated by arrows.

Similarly to what we observed in **Figure 10A, B**, the V_{thr} values are shifted to more depolarized membrane potentials as pH_e became more acidic while keeping the intracellular pH at pH_i = 6.2. For statistical analysis, the V_{thr} values were individually determined on a cell-by-cell basis and plotted as a function of the extracellular pH in **Figure 13A** and as a function of ΔpH in **Figure 13B**. The values of V_{thr} for PMN-MDSCs were −16.7 ± 3.1 mV at ΔpH_{e-i} = 1.2; +20 ± 5 mV at ΔpH_{e-i} = 0.2; +15.0 ± 6.5 mV at ΔpH_{e-i} = 0; and +63.3 ± 3.3 mV at ΔpH_{e-i} = −0.5. For Mo-MDSCs, the V_{thr} was −14.4 ± 5.5 mV for ΔpH_{e-i} = 1.2; +40.0 ± 10.8 mV at ΔpH_{e-i} = 0.2, +38.0 ± 9.2 mV for ΔpH_{e-i} = 0; and +57.5 ± 7.5 mV at ΔpH_{e-i} = −0.5.

The linear regression analysis of the V_{thr}-ΔpH_{e-i} relationship did not deviate from the "rule of forty", i.e., (~40 mV shift per one unit ΔpH change) for either PMN- or Mo-MDSCs (191), however, the V_{thr}-ΔpH_{e-i} is shifted to depolarized potentials for the currents recorded in Mo-MDSCs.

5.1.3.3 H^+ selectivity and pharmacology of the whole-cell H^+ currents in MDSCs

The H^+ selectivity of currents in PMN-MDSCs was assessed by deriving the reversal potential (E_{rev}) through analyzing whole-cell tail currents. Cells were depolarized to +100 mV for 500 ms to initiate the current, succeeded by repolarizations to diverse membrane potentials (ranging from −60 to +100 mV) to elicit the tail currents (**Figure 14A-D**).

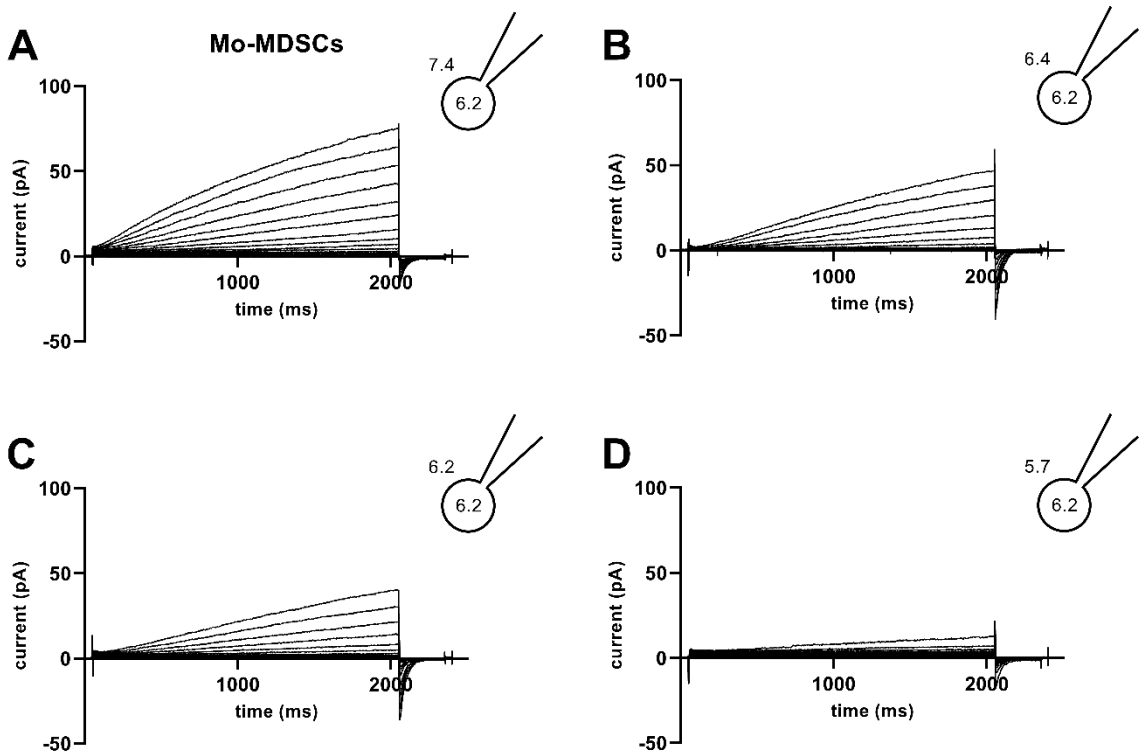

Figure 12. **Families of H^+ currents and I-V curves in murine Mo-MDSCs**. Whole-cell H^+ currents were recorded in a murine Mo-MDSC freshly isolated from an LLC tumor. 2-s-long depolarizing pulses were applied from a holding potential of -80 mV to +100 mV in 10 mV increments. While the internal solution was maintained constantly in the micropipette at pH_i = 6.2, the cell was locally perfused at different pH_e values (7.4 (**A**), 6.4 (**B**), 6.2 (**C**) and 5.7 (**D**)). Representative of 5 (**A**), 5 (**B**), 4 (**C**) and 5 (**D**) similar families of currents. Every trace has been filtered with a 25-point boxcar filter.

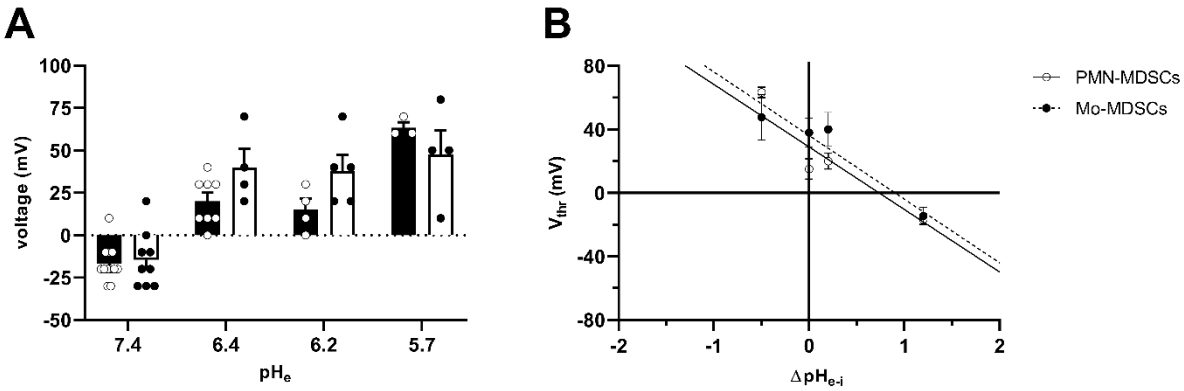

Figure 13. **Effect of pH_e on the activation threshold (V_{thr}) of H_v1 in murine PMN- and Mo-MDSCs**. (A) Bars and error bars indicate the mean ± SEM (PMN-MDSCs–7.4: n = 12, 6.4: n = 8, 6.2: n = 4, 5.7: n = 3; Mo-MDSCs–7.4: n = 9, 6.4: n = 4, 6.2: n = 5, 5.7: n = 4) of the voltage threshold (V_{thr}) calculated using the family of currents for each pH_e condition (see Materials and Methods and **Figure 11E,F).** The pH of the pipette filling solution was pH_i = 6.2. Symbols indicate individual data points obtained in PMN-MDSCs (empty circles and black-filled bars) and Mo-MDSCs (black-filled circles and empty bars). (B) V_{thr} plotted against ΔpH_{e-i} ($pH_e - pH_i$) in PMN-MDSCs (empty circles) and Mo-MDSCs (black-filled circles). The shift in V_{thr} by moving pH_e of one unit was determined by the slope of the linear intercept (PMN-MDSCs: −39.36 mV/ΔpH, R^2 = 0.7769; Mo-MDSCs: −40.07 mV/ΔpH, R^2 = 0.6465). Every value with its error bar indicates the mean ± SEM.

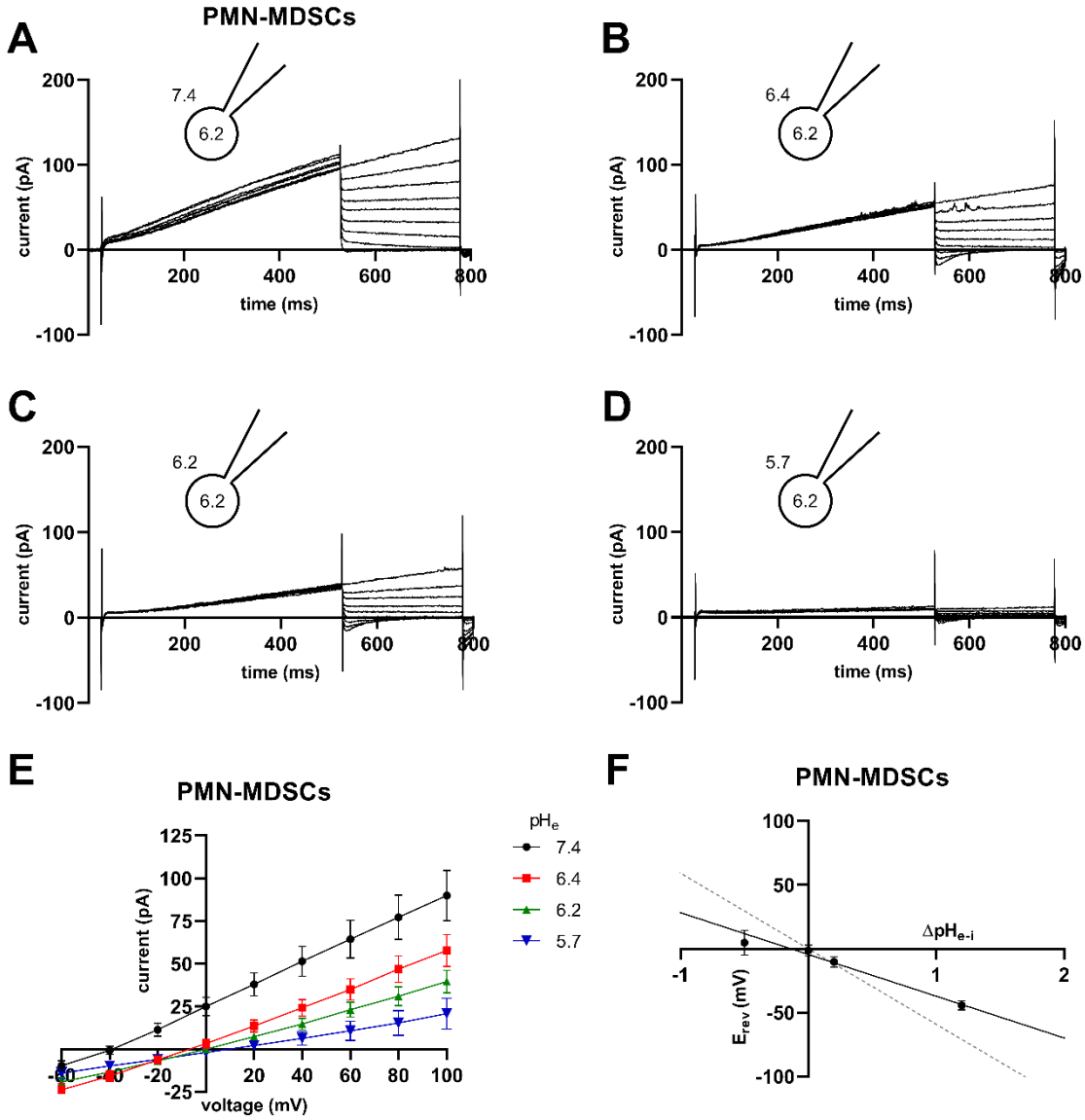

Figure 14. **Tail currents and E_{rev} in PMN-MDSCs.** (**A**–**D**) Representative families of currents obtained using the tail current protocol in a PMN-MDSC cell. The cell was depolarized from a holding potential of −80 mV to +100 mV for 500 ms followed by repolarizations to various potentials (from −60 to +100 mV in 20 mV increments). The pH of the internal solution was maintained pH_i = 6.2, and the cell was locally perfused with solutions having different pH_e of 7.4 (**A**), 6.4 (**B**), 6.2 (**C**) and 5.7 (**D**). (**E**) Selected tail currents from (**A**–**D**) are illustrated at increased time and amplitude resolution. The tail currents corresponding to E_{rev} are indicated in red. The dashed lines correspond to 0 pA current. (**F**) The reversal potentials (E_{rev}) were determined individually for each cell at each ΔpH_{e-i}, averaged (mean ± SEM, 7.4: *n* = 18, 6.4: *n* = 11, 6.2: *n* = 11, 5.7: *n* = 4), and plotted as a function of ΔpH_{e-i}. The best fit linear regression (solid line, slope: −41.8 mV/ΔpH, R^2 = 0.99) and the theoretical relationship calculated from the Nernst equation for H^+ (dashed line, slope: −59.2 mV/ΔpH) are indicated.

The membrane potential where the polarity of the tail current reversed was defined as the reversal potential. Selected traces are depicted in **Figure 14E** with more accurate amplitude resolution. The gradient of the best-fit linear regression line illustrates that E_{rev} shifts by −42 mV for each one-unit alteration in the extracellular pH (**Figure 14F**). Nevertheless, this slope differs from that of a perfectly selective H^+ conductance (−59.16 mV per one unit ΔpH change)

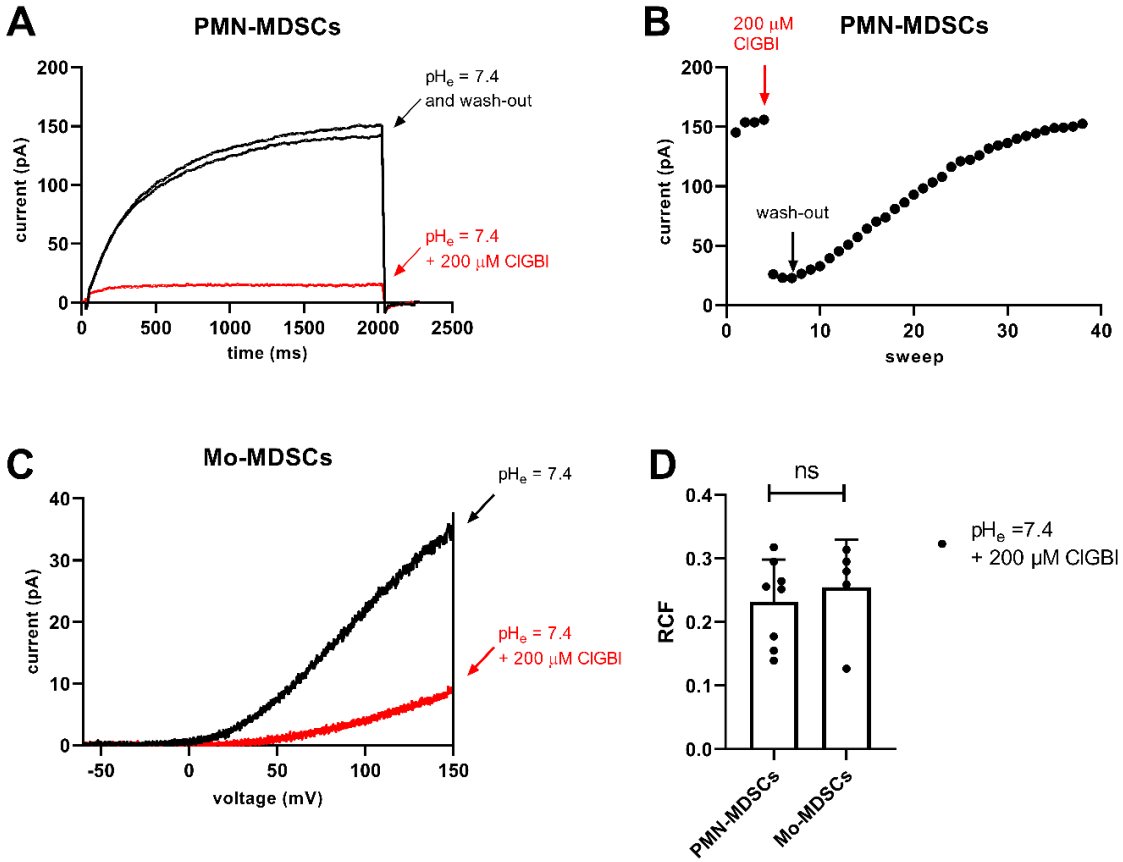

Figure 15. **Inhibition of H_v1 currents in murine PMN- and Mo-MDSCs by ClGBI**. (**A**) Representative whole-cell currents in a PMN-MDSs (holding potential: −80 mV, depolarization to +100 mV, every 15 s) prior to the application of ClGBI (black), at equilibrium block by 200 µM ClGBI (red) and following was-out (black). The pH_i and the pH_e were 6.2 and 7.4, respectively. (**B**) Representative time course of the onset and the recovery of the H_v1 current inhibition for the cell shown in panel **A**. Peak currents were determined as the average of the last 18 data points at +100 mV (see Materials and Methods); red and black arrows indicate the start of ClGBI application and the wash-out by ClGBI-free solution, respectively. (**C**) Representative whole-cell currents in a Mo-MDSCs (holding potential: −80 mV, voltage-ramp from −60 mV to +150 mV, every 10 s) prior to the application of ClGBI (black) and at equilibrium block by 200 µM ClGBI (red). Representative of 8 (**A**, **B**) and 5 (**C**) similar cells. Every trace has been filtered with a 25-point boxcar filter. (**D**) Remaining current fractions (RCF) in the presence of 200 µM ClGBI. Peak currents were determined for voltage-steps (PMN-MDSCs) and voltage-ramps (Mo-MDSCs) as described in the Materials and Methods. RCF was calculated as I/I_0 where I_0 and I are the peak currents in the absence and in the presence of 200 µM ClGBI upon reaching equilibrium block, respectively. Bars and error bars indicate the mean ± SEM, data points are determinations of RCF values in individual cells (PMN-MDSCs, n = 8; Mo-MDSCs, n = 5). Data were compared using Student's t-test with Welch's correction (p = 0.591, ns = not significant).

as anticipated by the Nernst equation (dashed line in **Figure 14F**). The currents in Mo-MDSCs were too minimal to allow for a reliable tail current analysis.

The literature frequently relies on the sensitivity to guanidine derivatives, especially ClGBI, as a pharmacological criterion for identifying H_v1 currents (76,190). In **Figure 15A**, it is evident that 200 µM ClGBI almost entirely inhibited the whole-cell current in a PMN-MDSC, and this inhibition was reversible as the current reverted to its original level after rinsing the recording chamber with ClGBI-free extracellular solution. The onset of inhibition was rapid, whereas it required more than 30 cycles in a ClGBI-free solution to wash out the effect (**Figure 15B**).

Contrary to PMN-MDSCs, we were able to do pharmacological experiments in Mo-MDSCs only using repeated application of a voltage-ramp protocol where long exposure to depolarized test potentials can be avoided (**Figure 15C**). Regardless of the voltage protocol used (i.e., step depolarization vs. voltage ramp), the application of 200 µM ClGBI reduced the magnitude of the current significantly, ~80% reduction in PMN-MDSCs and 75% in Mo-MDSCs (**Figure 15D**).

5.2 Intracellular acidity impedes $K_{Ca}3.1$ activation by Riluzole and SKA-31

The tumor microenvironment is a complex system inhabited by pro- and anti-tumor cells whose fine balance is easily disrupted. We have seen that pro-tumor MDSCs rely on H_v1 as their main ion channel and H_v1 is characterized by a strong sensitivity to pH. On the other side, anti-tumor infiltrating T cells rely on $K_v1.3$ and $K_{Ca}3.1$ to exert their function. Virtually nothing is known about the influence of pH on $K_{Ca}3.1$ and on its positive modulators. In this section of my dissertation, I will explain how we studied the effect of pH on $K_{Ca}3.1$ in two different expression systems and the effect of pH on two modulators of the aforementioned channel, Riluzole and SKA-31.

5.2.1 Extracellular pH variations minimally influence K^+ currents through $K_{Ca}3.1$ expressed endogenously in PBLs

The expression of $K_{Ca}3.1$ is transcriptionally up-regulated when T cells are stimulated with mitogens (192). We took advantage of this and induced T cell proliferation with phytohemagglutinin A (PHA) to enhance $K_{Ca}3.1$ expression. Alongside PHA activation of T cells, we supplemented the pipette filling solution with a Ca^{2+} (1 µM concentration) to ensure complete activation of the $K_{Ca}3.1$ current. PHA treatment also increases the expression of the voltage-gated $K_v1.3$ K^+ channel in T cells. Isolated $K_{Ca}3.1$ currents in activated T cells can be recorded by either pharmacological separation, achieved through the inhibition of $K_v1.3$ current using peptide toxins (193), or by analyzing whole-cell currents below the activation threshold of $K_v1.3$. We opted for the latter approach.

The threshold for the activation of $K_v1.3$ typically falls between −30 and −40 mV (194,195), although this can be cell- and recording condition-dependent and some authors extend the range to −60 mV to −50 mV (196). Moreover, as it can be easily observed (**Figure 16A**), V_{thr} for $K_v1.3$ activation is sensitive to changes in pH_e: acidification of the extracellular pH causes a right shift of V_{thr} (176,197). This latter phenomenon can also be used to confirm the solution exchange in the extracellular medium (**Figure 16A, C, E**). Because of all these reasons, we have assigned the currents to $K_{Ca}3.1$ in the region between −120 mV and −60 mV to avoid contamination of the analysis of $K_{Ca}3.1$ currents by a $K_v1.3$ component. The inset to

Figure 16A indicates that the current-voltage relationship is linear within this range. Therefore, the slopes of the straight lines fitted to the highlighted section of the traces were utilized to ascertain the $K_{Ca}3.1$-specific K^+ conductance, denoted as G_K thereafter (calculated as $G_K = \Delta I/\Delta V$). The reversal potential (E_{rev}) of the leak-corrected currents falls within the range of −75 mV to −100 mV, indicating the potassium (K^+) selectivity of the current. The theoretical E_{rev} of a K^+ selective conductance, calculated from the Nernst equation, is E_K= −89 mV. **Figure 16A** and its inset qualitatively demonstrate that $K_{Ca}3.1$ currents recorded at various pH_e values ranging from pH_e=8.0 to pH_e=6.0 overlap when the S-ICS (pH=7.2) was employed as the pipette filling solution. **Figure 16B** displays the G_K obtained at different pH_e values using S-ICS in the pipette (in the same experiment as in **A**). **Figure 16B** indicates that changing of pH_e alters minimally but fully and readily reversibly G_K. The same set of experiments as in **Figure 16A** and **Figure 16B** were repeated using pipette-filling solution having pH_i=8.0 (8.0-ICS) and pH_i=6.5 (6.5-ICS). The results were essentially the same as at pH_i=7.2 (**Figure 16C-F** and **Figure 16H**): at pH_i=7.2 and pH_i=8.0 there is a slight yet noteworthy reduction in the normalized conductance occurred with the transition to acidic extracellular pH values, while the conductances remained essentially unchanged when the pH_i was 6.5, irrespective of variations in pH_e. Moreover, G_K values at pH_e=7.4 are relatively constant throughout a given experiment, regardless of the pH_i. Taking the ratio of the K^+ conductances determined at a time point t >200 s ($G_{K,200}$) in S-ECS over G_K at the beginning of the experiment (0 s) in S-ECS ($G_{K,0}$) resulted in $G_{K,200}/G_{K,0}$ ~1 thereby indicating the stability of the whole-cell $hK_{Ca}3.1$ currents (**Figure 16G**).

5.2.2 Extracellular pH variations minimally influence K^+ currents through $K_{Ca}3.1$ expressed heterologously in CHO cells

We repeated the same set of experiments using cells transfected with the $hK_{Ca}3.1$ gene. We decided to use the commonly used epithelial Chinese Hamster Ovary (CHO) cell line since these cells do not express $K_v1.3$ or other K_v channels (198), therefore one can minimize the contamination of the data by other K^+ conductances.

However, since the channels are overexpressed in this cell model, we observed currents reaching several nA of amplitude, which is several folds greater than what we observed in PBLs at identical intracellular Ca^{2+} concentration (compare **Figures 16A** and **17A**). Pharmacological data obtained using overexpressed ion channels due to the increased $K_{Ca}3.1$ conductance are

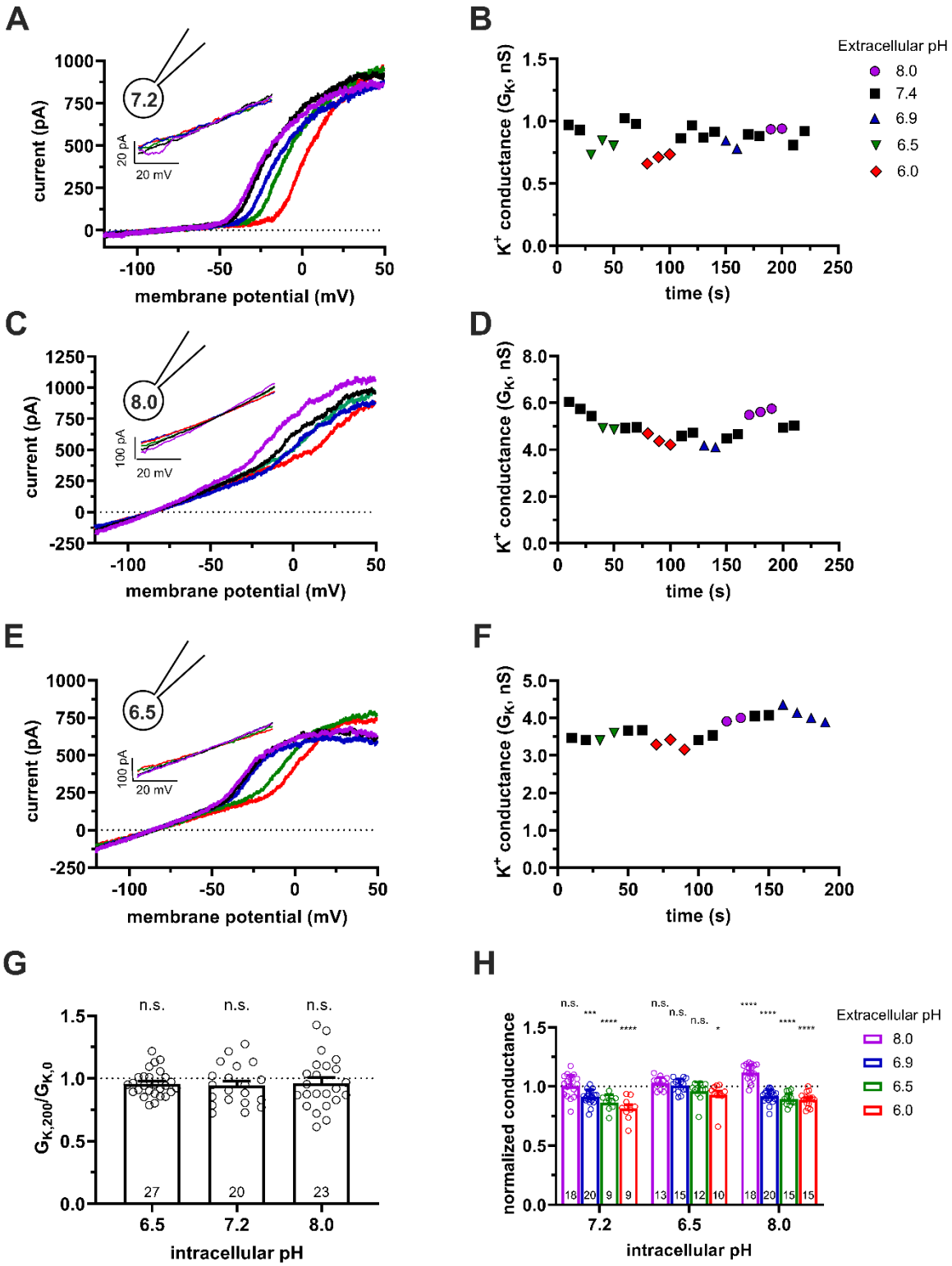

Figure 16. **Effect of the extra- and intracellular pH on $K_{Ca}3.1$ currents in human PBLs.** (**A**, **C**, **E**) Representative current traces were evoked by 150-ms-long voltage ramps, ranging from –120 to +50 mV in whole-cell patch-clamped human peripheral T cells. Voltage ramps were repeated every 10 seconds, the holding potential was –85 mV between pulses. The pipette filling solutions were S-ICS (pH_i=7.2, panel **A**), 8.0-ICS (pH_i=8.0, panel **C**), and 6.5-ICS (pH_i=6.5, panel **E**), the cells were perfused with extracellular solutions having pH_e=6.0 (6.0-ECS, red), pH_e=6.5 (6.5-ECS, green), pH_e=6.9 (6.9-ECS, blue), pH_e=7.4 (S-ECS, black), and pH_e=8.0 (8.0-ECS, purple). Insets show the $K_{Ca}3.1$-specific K^+ current measured below the activation threshold of $K_v1.3$, between –120 mV and –60 mV. (**B**, **D**, **F**) $K_{Ca}3.1$-specific K^+ conductance (G_K) was determined by fitting straight lines to the traces in the insets in panels **A**, **C**, and **E** and plotted as a function of time for pH_i=7.2 (**B**, same cell as in **A**),

pH_i=8 (**D**, same cell as in **C**) and pH_i=6.5 (**F**, same cell as in E). The color of the symbols indicates the pH of the extracellular solutions. (**G**) The ratio of the K^+ conductances determined at t >200 s ($G_{K,200}$) in S-ECS over G_K at the beginning of the experiment (t=0 s) in S-ECS ($G_{K,0}$), indicated as $G_{K,200}/G_{K,0}$. The pH_i of the pipette-filling solutions is indicated. Bars and error bars indicate the mean ± SEM, symbols show individual values, and numbers in the bars indicate the number of cells. (**H**) Normalized K^+ conductance was calculated as $G_{K,x}/G_{K,7.4}$, where $G_{K,x}$ and $G_{K,7.4}$ are the $K_{Ca}3.1$-specific K^+ conductances at pH_e=x and pH_e=7.4, respectively. Bars are grouped by the pH of the pipette-filling solution (pH_i). Bars and error bars indicate the mean ± SEM, symbols show individual values, numbers in the bars indicate the number of cells. Statistical analysis (**G**, **H**) was performed using one-way ANOVA (against H_0:μ_0=1 hypothesis) with multiple comparisons (Bonferroni). *p < 0.05, ***p < 0.001, ****p < 0.0001, n.s., not significant (p > 0.05). Extracellular pH was represented in all cases with the same colors: purple for 8.0, black for 7.4, green for 6.9, blue for 6.5, and red for 6.0.

more reliable since the effect of leak on the whole-cell K^+ conductance is minimized. Similarly to human lymphocytes, $K_{Ca}3.1$ currents recorded at pH_e values ranging from pH_e=8.0 to pH_e=6.0 in CHO cells are superimposable when the S-ICS (pH=7.2) was used as the pipette filling solution (**Figure 17A**). **Figure 17B** indicates that changing of pH_e alters G_K minimally but fully and readily reversibly. The same set of experiments as in **Figures 17A** and **17B** were repeated using pipette-filling solution having pH_i=8.0 (8.0-ICS, **Figures 17C** and **17D**) and pH_i=6.5 (6.5-ICS, **Figures 17E** and **17F**). **Figure 17G** enables us to reach a similar conclusion as that obtained for human peripheral blood lymphocytes, indicating that G_K values remain relatively constant at pH_e=7.4 across the duration of an experiment, irrespective of the pH_i. The bar graph in **Figure 17H**, representing normalized conductance ($G_{K,x}/G_{K,7.4}$) values, illustrates a slight yet significant decrease in normalized conductance at specific combinations of pH_i and pH_e.

5.2.3 Normal and basic intracellular pH do not interfere with activation of the $K_{Ca}3.1$ current either by Riluzole or by SKA-31

Riluzole and its more potent derivative SKA-31 (199) are positive modulators of the $K_{Ca}3.1$ currents in micro- and nanomolar-range concentrations, respectively. To determine the experimental EC_{50} values, i.e. the concentrations at which the substances causes half maximal activation of the current, we applied increasing concentrations of Riluzole or SKA-31 to transfected CHO cells (**Figure 18A-D**) and measured G_K. When we use an intracellular concentration of 1 µM Ca^{2+} (as shown in **Figures 16** and **17**) the currents through $K_{Ca}3.1$ are already saturated (see **Figure 3B**), hence a pharmacological enhancement cannot be fully appreciated. Given that the enhancement of the $K_{Ca}3.1$ current by the activators is more prominent at lower cytosolic Ca^{2+} concentrations compared to the ~1 µM Ca^{2+} concentration utilized previously, we employed pipette filling solutions containing 250 nM Ca^{2+} concentration (7.2-ICS-250) in this series of experiments (181). The G_K values under this condition gradually increased with the concentration of SKA-31 (**Figure 18A**) or Riluzole (**Figure 18C**).

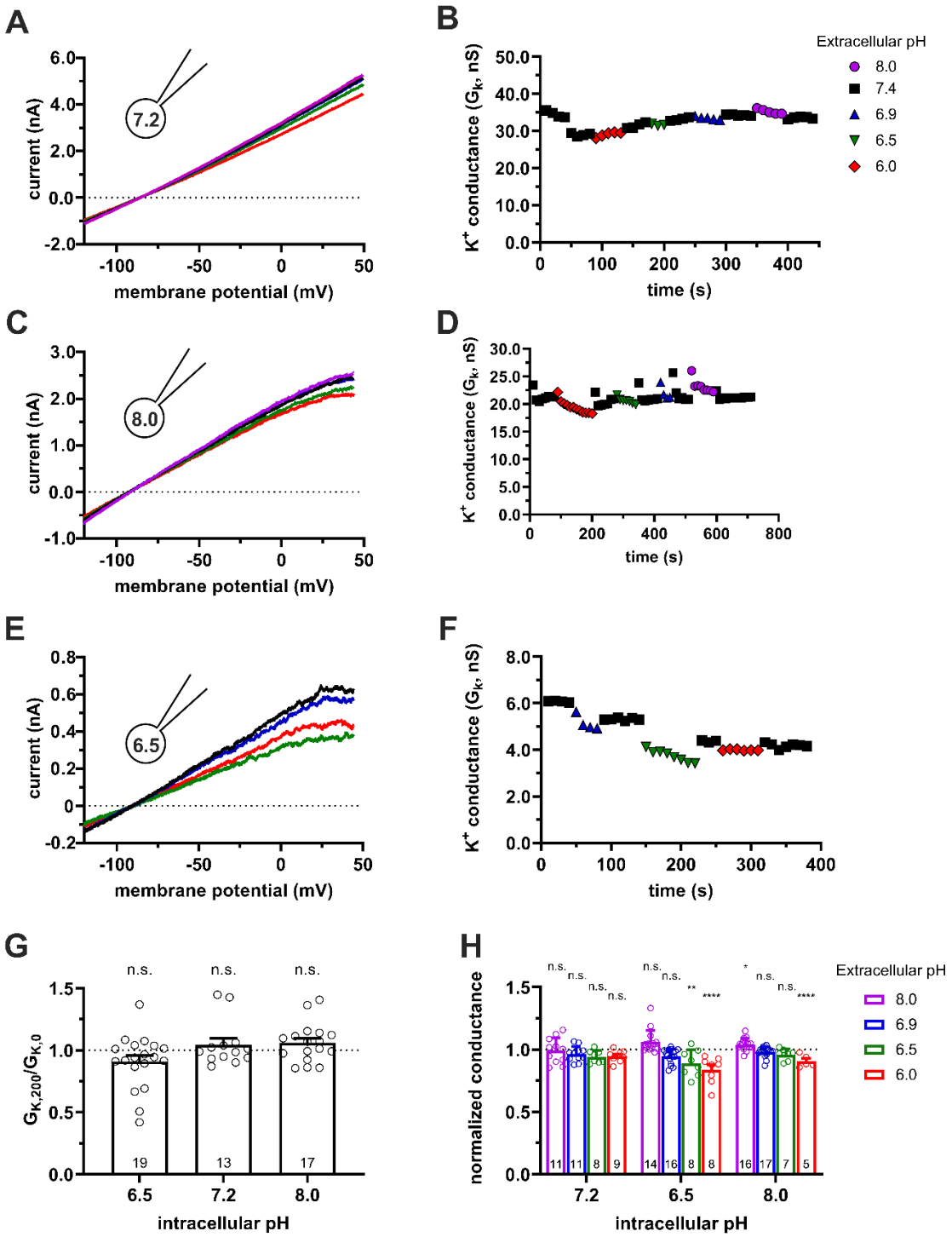

Figure 17. **Effect of the extracellular and intracellular pH on currents generated in CHO cells transfected with turboGFP-hK$_{Ca}$3.1.** (**A**, **C**, **E**) Representative current traces were evoked by 150-ms-long voltage ramps, ranging from −120 to +50 mV in whole-cell patch-clamped CHO cells expressing hK$_{Ca}$3.1 channels. Voltage ramps were repeated every 10 seconds, the holding potential was −85 mV between pulses. The pipette filling solutions were S-ICS (pH$_i$=7.2, panel **A**), 8.0-ICS (pH$_i$=8.0, panel **C**) and 6.5-ICS (pH$_i$=6.5, panel **E**) and perfused with extracellular solutions having pH$_e$=6.0 (6.0-ECS, red), pH$_e$=6.5 (6.5-ECS, green), pH$_e$=6.9 (6.9-ECS, blue), pH$_e$=7.4 (S-ECS, black), and pH$_e$=8.0 (8.0-ECS, purple). (**B**, **D**, **F**) K^+ conductance (G_K) was determined by fitting straight lines to the traces in panels **A**, **C**, **E** and plotted as a function of time for pH$_i$=7.2 (**B**, same cell as in **A**), pH$_i$=8 (**D**, same cell as in **C**) and pH$_i$=6.5 (F, same cell as in E). The color of the symbols indicates the pH of the extracellular solutions. (**G**) Ratio of the K^+ conductances determined at t >200 s ($G_{K,200}$) in S-ECS over G_K at the beginning of the experiment (t=0 s) in S-ECS ($G_{K,0}$), indicated as $G_{K,200}/G_{K,0}$. The pH$_i$ of the pipette-filling solutions are indicated. Bars and error bars indicate the mean ± SEM, symbols show individual values, numbers

in the bars indicate the number of cells. (**H**) Normalized K^+ conductance was calculated as $G_{K,x}/G_{K,7.4}$, where $G_{K,x}$ and $G_{K,7.4}$ are the K^+ conductances at pH_e=x and pH_e=7.4. Bars are grouped by the pH of the pipette-filling solution (pH_i). Statistical analysis was performed using one-way ANOVA (against H_0:μ_0=1 hypothesis) with multiple comparison (Bonferroni) (**G**, **H**). *p < 0.05, **p < 0.01, ****p < 0.0001, n.s., not significant (p > 0.05).

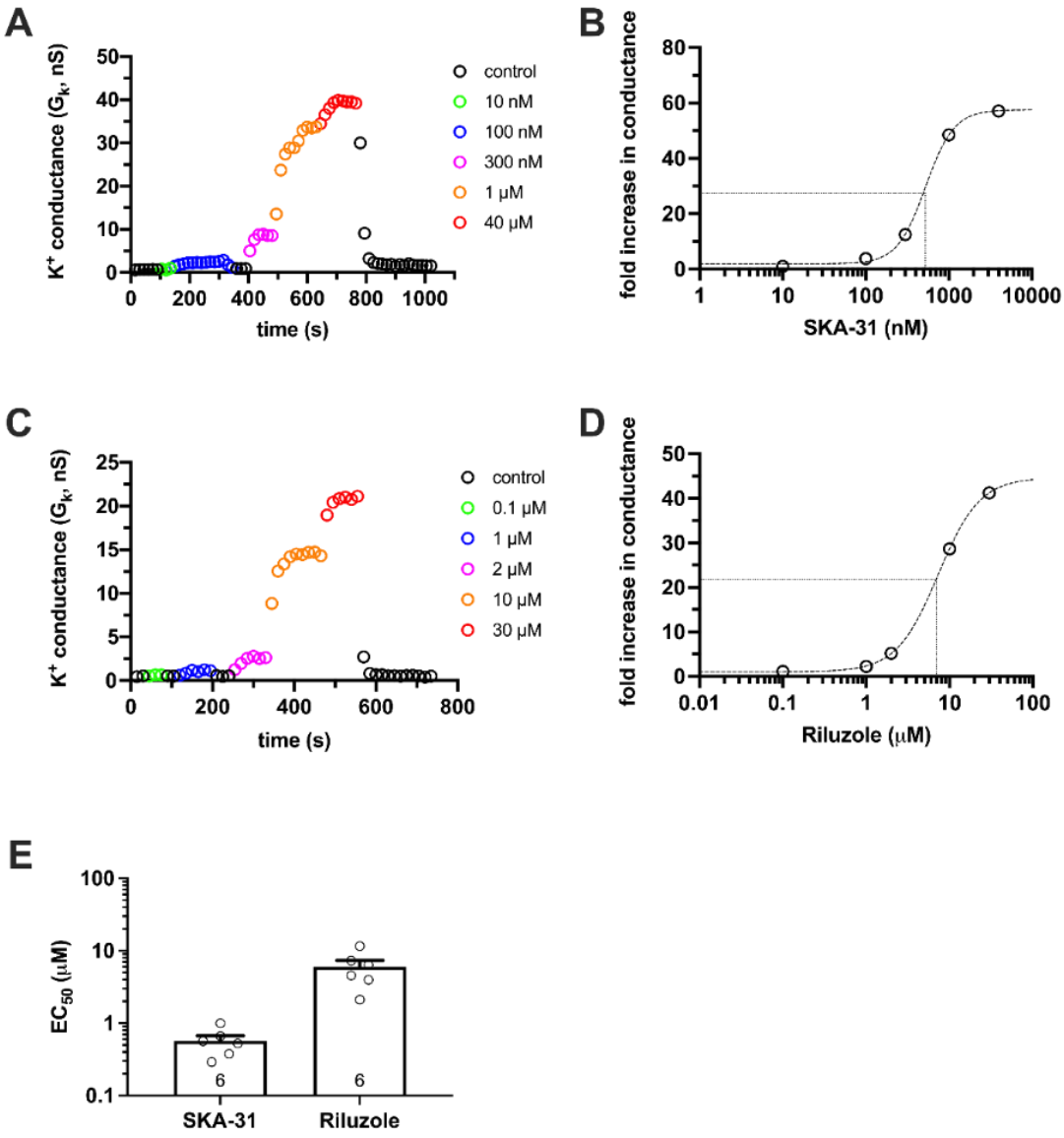

Figure 18. **Activator concentration-response for SKA-31 and Riluzole in CHO cells**. $K_{Ca}3.1$ currents were recorded in CHO cells transfected with turboGFP-h$K_{Ca}3.1$ using S-ECS bath solution (pH_e = 7.4) and 7.2−ICS−250 pipette filling solution (250 nM free Ca^{2+} concentration, pH_i = 7.2). The activators at the indicated concentrations were diluted in S-ECS. (**A**) $K_{Ca}3.1$ currents were evoked by voltage ramps ranging from −120 mV to +50 mV, K+ conductance was determined from the slope of the current-voltage relationship and plotted as a function of time. Colored symbols represent the indicated concentrations of SKA-31. (**B**) Activator concentration-response for SKA-31 for the cell shown in panel A. Fold increase in the conductance was calculated as $G_{K,act}/G_K$, where $G_{K,act}$ and G_K are the K^+ conductance measured in the presence and the absence of the activator in S-ECS, respectively. The dashed line is the best-fit Hill equation with EC_{50} = 526.4 nM, n_H = 2.5. The half maximal activation and the EC_{50} are indicated by the dotted lines. (**C**) Same experiment as in panel **A**, except the indicated concentrations of Riluzole were used. (**D**) The activator concentration-response Riluzole for the cell shown in panel **C**, see details in panel **B**. EC_{50} = 7.37 µM, n_H = 1.74 were obtained. (**E**) EC_{50} values determined from fitting individual activator concentration-response relationships for Riluzole and SKA-31. Symbols in the bar graph (mean ± SEM) show individual values, and numbers in the bar indicate the number of cells.

To construct the concentration-response curve, we calculated the fold increase in conductance caused by the activators as suggested in the literature ((51) and see Materials and Methods) and plotted this variable as a function of the activator concentration (**Figure 18B, D**). The EC_{50} values for Riluzole and SKA-31 were, respectively, 6.0 ± 1.3 μM and 570 ± 101 nM as calculated by averaging the EC_{50} values determined individually cell-by-cell (**Figure 18E**).

To examine the influence of extracellular pH on the effects of $K_{Ca}3.1$ activators, Riluzole (5 μM) or SKA-31 (1 μM) were introduced into extracellular solutions spanning a pH_e range from 6.0 to 8.0. The activator concentrations were chosen to be close to the EC_{50} of the substances (**Figure 18E**). Meanwhile, the intracellular pH of whole-cell patch-clamped PBLs was adjusted and buffered at pH_i=7.4, pH_i=8.0, or pH_i=6.5 using the suitable intracellular solution (as detailed in **Table 2**).

The raw current traces produced by voltage ramps in **Figure 19A** and **Figure 19C** indicate that the baseline $K_{Ca}3.1$ currents are nearly negligible. Upon perfusing the recording chamber with the activators in the S-ECS there is a significant increase in the slope of the current-voltage relationship.

Additionally, the slopes of the current traces recorded in the presence of activators at various pH_e values exhibit substantial overlap. The $K_{Ca}3.1$ conductance is instantaneously increased upon perfusion with either 1 μM SKA-31 (**Figure 19A, B**) or 5 μM Riluzole (**Figure 20A, B**), regardless of the extracellular solution's pH_e, and the removal of activators reduces the current within 2-4 episodes, corresponding to 20-40 s. The reversible effect of the activators can be repeatedly observed over prolonged periods with no significant decline in $K_{Ca}3.1$ conductance. In this analysis we calculated the $G_{K,end}/G_{K,start}$ where $G_{K,end}$ and $G_{K,start}$ represent the modulator-enhanced K^+ conductance at the end of the experiment (≥ 800 s) and the beginning of the experiment, respectively (**Figure 19E**, left side). Similar qualitative outcomes were observed when using the 8.0-ICS-250 pipette filling solution (**Figure 19C, D**, **Figure 20C, D** and **Figure 19E**, right side). The quantitative analysis presented in **Figure 19F and G** corroborated the aforementioned findings. To compare the impact of the activators, we initially computed the "fold increase in conductance" (as shown in **Figure 19B**) induced by the activator at specific pH_i and pH_e combinations, then normalized it to the "fold increase in conductance" observed with the activators in S-ECS at pH_e=7.4. The resulting "fold increase normalized to 7.4" values, obtained in this manner, consistently clustered around 1 for both Riluzole (**Figure 19F**) and SKA-31 (**Figure 19G**), regardless of the pH_i (7.2 or 8.0) or the pH_e (8.0, 6.9, 6.5, or 6.0).

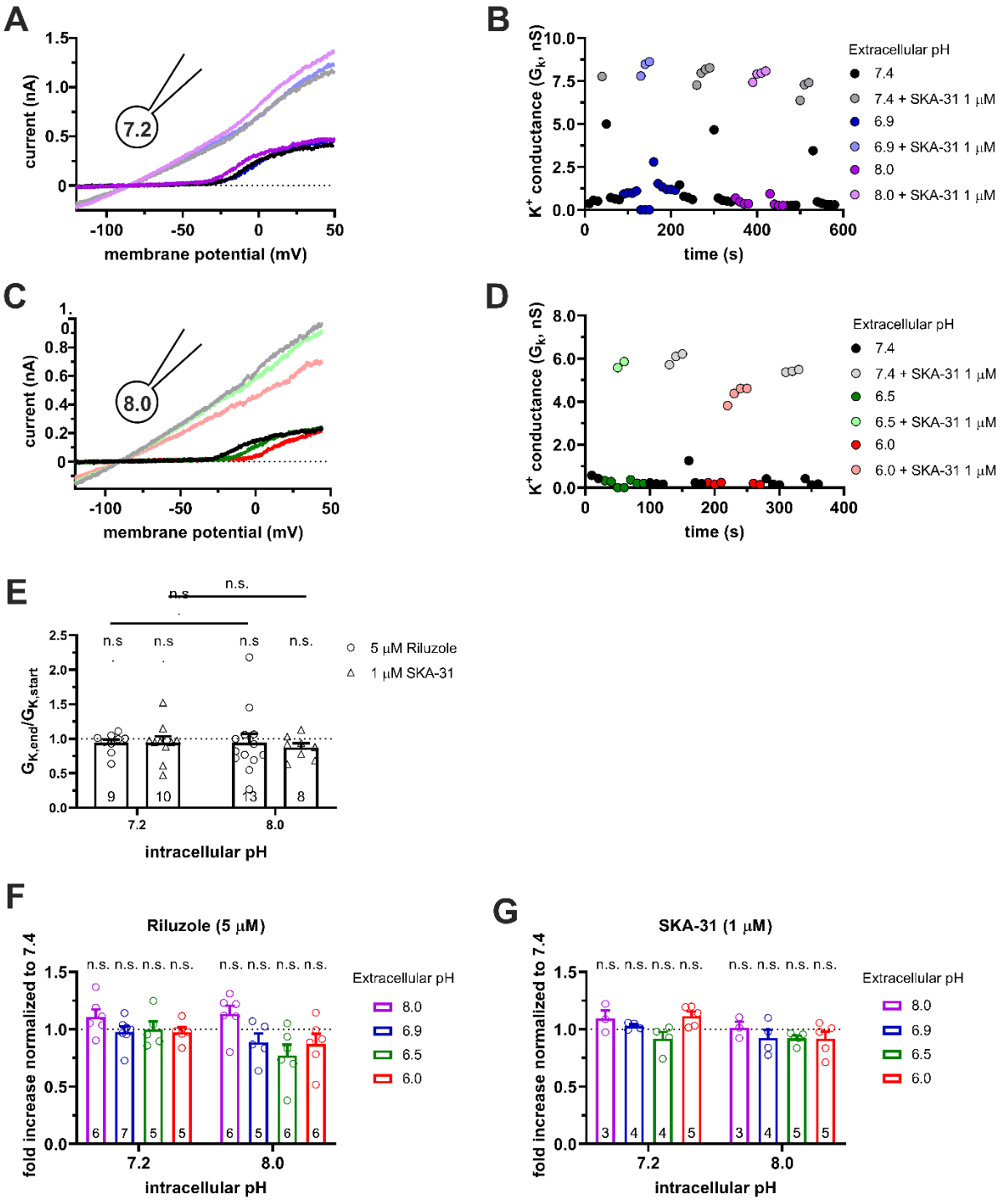

Figure 19. **Effect of SKA-31 on the $K_{Ca}3.1$ currents in PHA-activated PBLs at different pH_e and pH_i combinations.** (**A**, **C**) Representative current traces were evoked by 150-ms-long voltage ramps, ranging from –120 to +50 mV in whole-cell patch-clamped human peripheral T cells. Voltage ramps were repeated every 10 seconds, the holding potential was –85 mV between pulses. The pipette filling solutions were 7.2-ICS-250 (pH_i=7.2, panels **A** and **B**) or 8.0-ICS-250 (pH_i=8.0, panels **C** and **D**). The cells were perfused with extracellular solutions having pH_e=6.0 (6.0-ECS, red), pH_e=6.5 (6.5-ECS, green), pH_e=6.9 (6.9-ECS, blue), pH_e=7.4 (S-ECS, black), and pH_e=8.0 (8.0-ECS, purple). The corresponding lighter colors display traces obtained in the presence of the modulator. (**C**, **D**) $K_{Ca}3.1$-specific K^+ conductance (G_K) was determined by fitting straight lines to the traces below the activation threshold of $K_v1.3$ in panels **A** and **B** and plotted as a function of time. **B**: Data from panel **A**: pH_i=7.2. pH_e and 1 μM SKA-31 as indicated. **D**: Data from panel **B**: pH_i=8.0, pH_e and 1 μM SKA-31 as indicated. (**E**) Loss of the potency of the modulators was expressed as $G_{K,end}/G_{K,start}$ ratio ($G_{K,end}$ and $G_{K,start}$ are the averaged

K^+ conductances with the presence of the activator in S-ECS at the end and at the beginning of the experiment, respectively), calculated for each cell and plotted as a bar graph (mean ± SEM). Symbols show individual values, numbers in the bar indicate the number of cells. (**F**, **G**) The "fold increase normalized to 7.4" was calculated dividing the activator-induced "fold increase in conductance" (see e.g. **Figure 3B** and in the Materials and Methods) at a given pH_i and pH_e combination by the "fold increase in conductance" measured with the activators in S-ECS at pH_e=7.4. Statistical analysis was performed using one-way ANOVA (against H_0:μ_0=1 hypothesis) with multiple comparison (Bonferroni) (**E**, **F**, **G**) and Student's unpaired t-test (Riluzole 7.2 vs. SKA-31 7.2, Riluzole 8.0 vs. SKA-31 8.0) (**E**). n.s., not significant ($p > 0.05$). The representative traces of Riluzole at pH_i = 7.2 and 8.0 are in **Figure 20**.

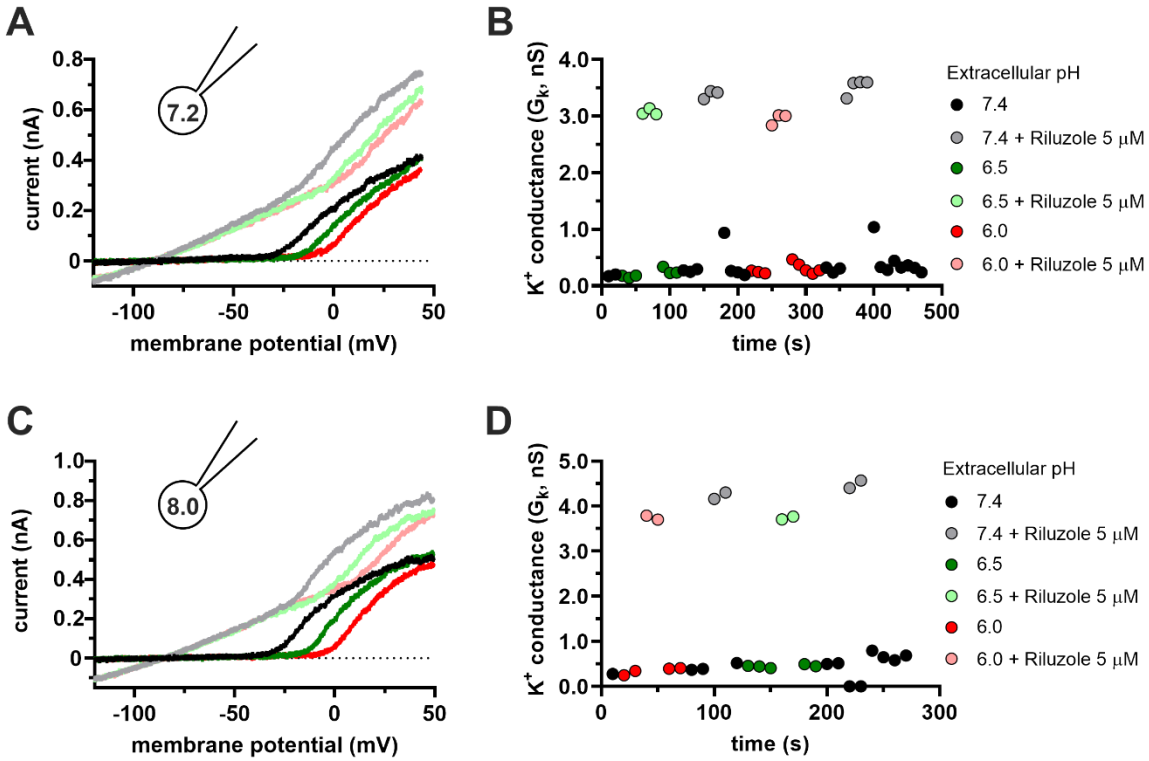

Figure 20. **Effect of Riluzole on the K_{Ca}3.1 currents in PHA-activated PBLs at different pH_e and pH_i combinations.** (**A**, **C**) Representative current traces were evoked by 150-ms-long voltage ramps, ranging from −120 to +50 mV in whole-cell patch-clamped human peripheral T cells. Voltage ramps were repeated every 10 seconds, the holding potential was −85 mV between pulses. The pipette filling solutions were 7.2-ICS-250 (pH_i=7.2, panels **A** and **B**) or 8.0-ICS-250 (pH_i=8.0, panels **C** and **D**). The cells were perfused with extracellular solutions having pH_e=6.0 (6.0-ECS, red), pH_e=6.5 (6.5-ECS, green), pH_e=7.4 (S-ECS, black). The corresponding lighter colors display traces obtained in the presence of the modulator. For the sake of simplicity only representative traces at pH_e = 6.0 and 6.5 are shown for both pH_i = 7.2 and 8.0, while traces at pH_e = 6.9 and 8.0 are not shown.

We have shown that the enhancements of the K_{Ca}3.1 current by Riluzole and SKA-31 exhibit similar characteristics under identical experimental conditions. Consequently, we focused our subsequent experiments on SKA-31, which is more potent and selective. We replicated the same series of experiments in CHO cells expressing K_{Ca}3.1. **Figure 21A, B** show whole-cell currents recorded in a CHO cell using 7.2-ICS-250 pipette filling solution. The current in the absence of SKA-31 (dark-toned colors) increases robustly upon perfusing the

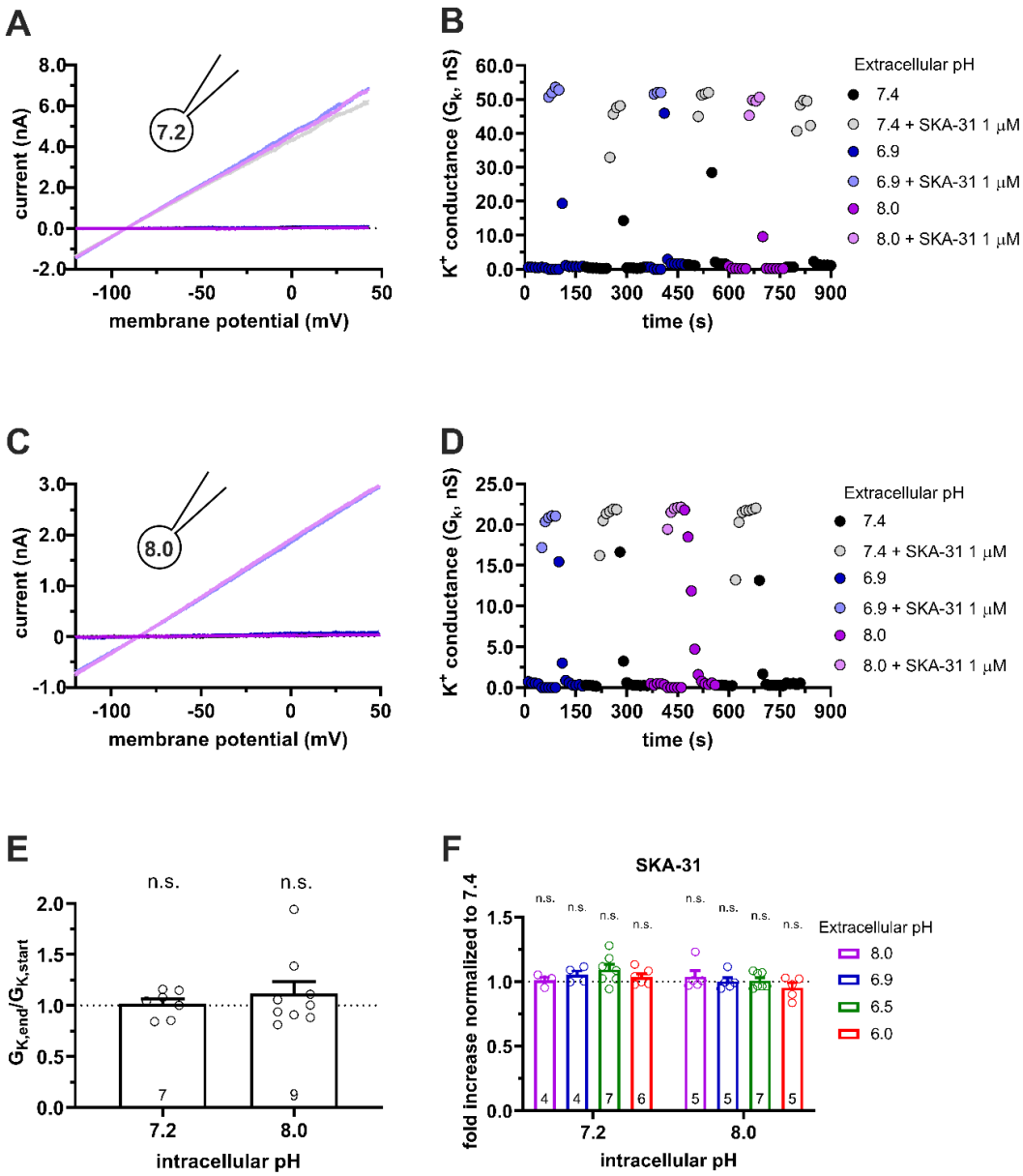

Figure 21. **Effect of SKA-31 on the $K_{Ca}3.1$ currents expressed in CHO cells at different pH_e and pH_i combinations.** (**A**, **C**) Representative current traces were evoked by 150-ms-long voltage ramps, ranging from –120 to +50 mV in whole-cell patch-clamped CHO cells. Voltage ramps were repeated every 10 seconds, the holding potential was –85 mV between pulses. The pipette filling solutions were 7.2-ICS-250 (pH_i=7.2, panel **A**) or 8.0-ICS-250 (pH_i=8.0, panel **C**). The cells were perfused with extracellular solutions having pH_e=6.9 (6.9-ECS, blue), pH_e=7.4 (S-ECS, black), and pH_e=8.0 (8.0-ECS, purple). The corresponding lighter colors display traces obtained in the presence of the modulator. (**B**, **D**) $K_{Ca}3.1$-specific K^+ conductance (G_K) was determined by fitting straight lines to the traces panels **A** and **C** and plotted as a function of time. **B**: data from panel **A**, pH_i=7.2. pH_e and 1 µM SKA-31 as indicated. **D**: data from panel **B**, pH_i=8.0, pH_e and 1 µM SKA-31 as indicated. (**E**) Loss of the potency of SKA-31 was expressed as $G_{K,end}/G_{K,start}$ ratio ($G_{K,end}$ and $G_{K,start}$ are the averaged K^+ conductances with the presence of the activator in S-ECS at the end and at the beginning of the experiment, respectively), calculated for each cell and plotted as a bar graph (mean ± SEM). Symbols show individual values, numbers in the bar indicate the number of cells. (**F**) The "fold increase normalized to 7.4" was calculated dividing the activator-induced "fold increase in conductance" (see e.g. **Figure 3B**) at a given pH_i and pH_e combination by the "fold increase in conductance" measured with the activators in S-ECS at pH_e=7.4. Statistical analysis was performed using one-sample t-test (E) and one-way ANOVA (against H_0:μ_0=1 hypothesis) with multiple comparison (Bonferroni) (**F**). n.s., not significant ($p > 0.05$). Extracellular pH was represented in all cases with the same colors: purple for 8.0, blue for 6.9, green for 6.5 and red for 6.0. For the sake of simplicity only representative traces at pH_e = 8.0, 7.4 and 6.9 are shown for both pH_i = 7.2 and 8.0, while traces at pH_e = 6.5 and 6.0 are not shown.

cells with solutions of different pH_e and supplemented with 1 µM SKA-31 (lighter-toned colors). The currents recorded in various pH_e values are superimposable, i.e., the potency of SKA-31 was the same regardless of the pH_e.

The characteristics of the enhancement of the $K_{Ca}3.1$ current by SKA-31 remained consistent throughout the experiment when the activator was administered repeatedly to a cell (**Figure 21A, B**). A qualitatively similar phenomenon was recorded when the cell was patch-clamped using an 8-ICS-250 pipette filling solution (**Figure 21C, D**). It is important to emphasize here that G_K was repeatedly activated by SKA-31 to the same extent at both pH_i values over an extended period of time following the start of the activator application. The analysis of the ratio $G_{K,end}/G_{K,start}$ supports this in **Figure 21E** where ratio is scattered around 1 suggesting that the potency of the activators throughout the experiment remained constant with both pH_i=7.2 and pH_i=8.0 pipette filling solutions. The quantitative demonstration of SKA-31's independence from the pH_e of the recording solution is depicted in **Figure 21F**. The variable "fold increase normalized to 7.4" shows values clustering around 1, mirroring observations made for PBLs.

5.2.4 Activation of the $K_{Ca}3.1$ current either by Riluzole or by SKA-31 gradually decreases in time when the intracellular pH is acidic

The behavior of the $K_{Ca}3.1$ current in response to Riluzole and SKA-31 in PBLs contrasts starkly with the previous scenario (see **Figure 20**) when the pipette-filling solution was 6.5-ICS-250, corresponding to a pH_i of 6.5. The effectiveness of both Riluzole and SKA-31 gradually diminishes with prolonged application of either drug (**Figure 22A**). To characterize this decline in potency over time, we utilized the $G_{K,end}/G_{K,start}$ ratio (see above). The decline in conductance was consistent when administering either 5 µM Riluzole (**Figure 22A**) or 1 µM SKA-31 (**Figure 22B**) repeatedly, and this phenomenon was unaffected by the pH_e: in other words, it continued unabated across all pH_e values until reaching saturation at approximately 20% of the conductance elicited by the activator at the beginning of the experiment (**Figure 22C**).

Similarly to the findings in PBLs, the $K_{Ca}3.1$ conductance gradually diminished with repeated administration of SKA-31 to the same transfected CHO cell at pH_i=6.5 (6.5-ICS-250). In **Figure 23A** it is illustrated that the gradual decline of SKA-31-induced conductance persisted at a seemingly consistent rate regardless of the pH_e of the extracellular solution. Additionally, the K^+ conductance remained unrecoverable upon re-administration of SKA-31 in the control S-ECS solution with pH_e=7.4. This loss of potency phenomenon was also evident

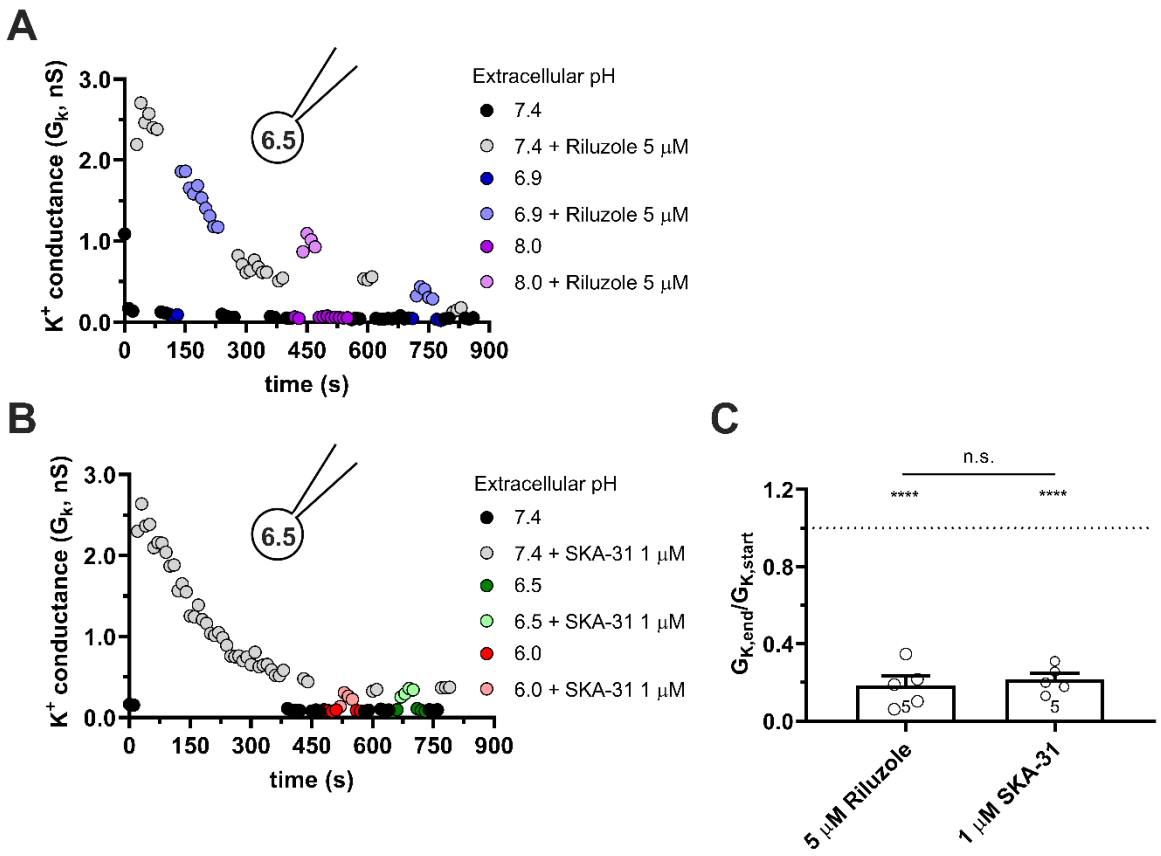

Figure 22. **Progressive loss of the potency of Riluzole and SKA-31 in activating $K_{Ca}3.1$ currents of PBLs at intracellular acidic condition**. Representative time courses of the effect of Riluzole (**A**) and SKA-31 (**B**) when the intracellular solution was kept at pH_i=6.5 (6.5-ICS-250) and cells were perfused with extracellular solutions having different pH_e values (ranging from 6.0 to 8.0) and modulators (**A**: 5 µM Rilozole, **B**: 1 µM SKA-31), as indicated. The current traces were evoked by 150-ms-long voltage ramps, ranging from -120 to +50 mV in whole-cell patch-clamped human peripheral T cells. Voltage ramps were repeated every 10 seconds, the holding potential was -85 mV between pulses. (**C**) Loss of the potency of the modulators was expressed as $G_{K,end}/G_{K,start}$ ratio ($G_{K,end}$ and $G_{K,start}$ are the averaged K^+ conductances with the presence of the activator in S-ECS at the end and at the beginning of the experiment, respectively), calculated for each cell and plotted as a bar graph (mean ± SEM). Symbols show individual values, numbers in the bar indicate the number of cells. Statistical analysis was performed using unpaired Student's t-tests (Riluzole vs. SKA-31) (**C**) and one-sample t-tests (against H_0:μ_0=1 hypothesis) (**C**). ****$p < 0.0001$, n.s., not significant ($p > 0.05$). Extracellular pH was represented in all cases with the same colors: purple for 8.0, black for 7.4, blue for 6.9, green for 6.5 and red for 6.0. The corresponding lighter colors display traces obtained in the presence of the modulator.

when the extracellular solution remained constant (S-ECS) while pH_i was slightly more alkaline (pH_i=6.7, as shown in **Figure 23B**) or more acidic (pH_i=6.2 as depicted in **Figure 23C**).

The loss of the K^+ conductance over the time-course of the experiment was characterized quantitatively using the $G_{K,end}/G_{K,start}$ ratio as described for PBLs (see **Figure 19E** for details). The bar chart in **Figure 23D** shows that the cells showing loss-of-potency phenotype upon repeated SKA-31 application displayed a large scatter in $G_{K,end}/G_{K,start}$ ratio with a median of 0.17.

To gain deeper insights into the nature of the loss-of-potency phenomenon, we investigated the response of the currents to SKA-31 at a constant pH_e of 7.4 (S-ECS) and pH_i

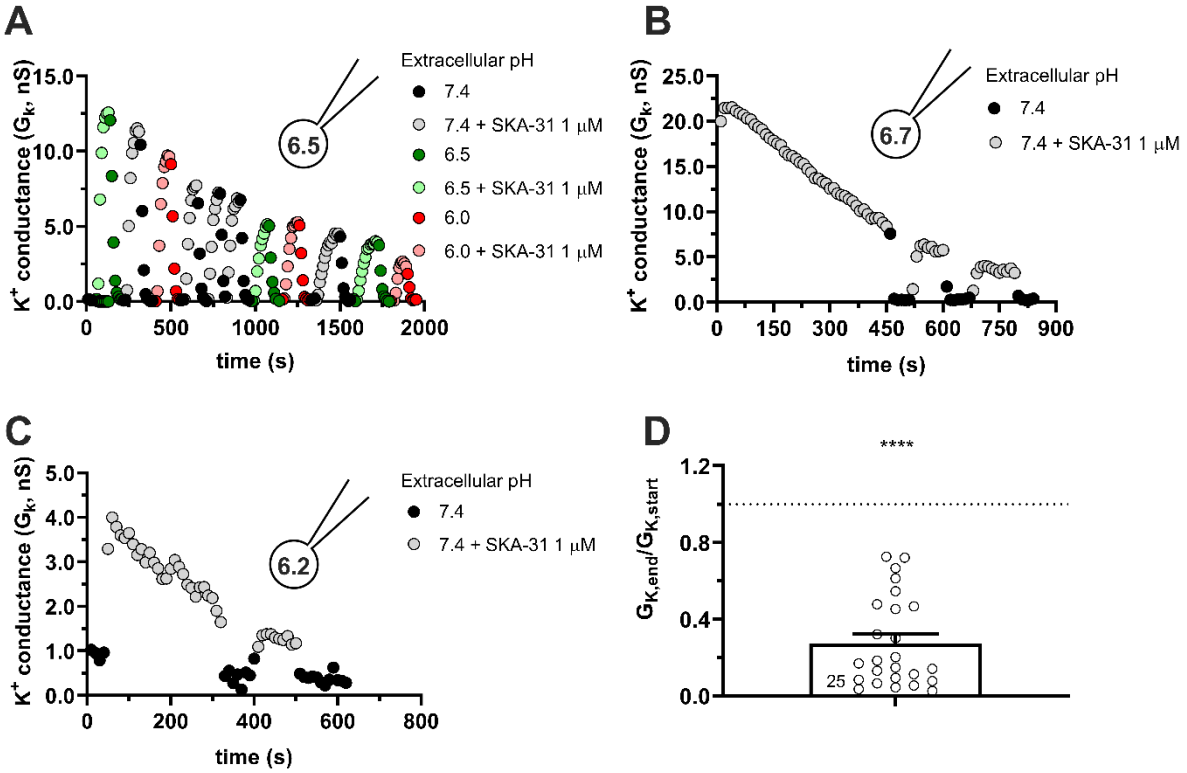

Figure 23. **Progressive loss of the potency of SKA-31 in activating $K_{Ca}3.1$ currents CHO at intracellular acidic conditions**. (**A**) Representative time course of the effect of SKA-31 when the intracellular solution was kept at pH_i=6.5 (6.5-ICS-250) and the cell was perfused with extracellular solutions having different pH_e values (ranging from 6.0 to 7.4) and supplemented with 1 μM SKA-31, as indicated. $K_{Ca}3.1$ current traces were evoked by 150-ms-long voltage ramps, ranging from –120 to +50 mV in whole-cell patch-clamped CHO cells transfected with $K_{Ca}3.1$ channels. (**B**, **C**) Representative time course of the effect of SKA-31 when the intracellular solution was kept at pH_i=6.7 (**B**) or pH_i=6.2 (**C**) and the cell was perfused with S-ECS (pH_e=7.4) and supplemented with 1 μM SKA-31, as indicated. Voltage protocol and other conditions as in panel A. (**D**) Loss of the potency of SKA-31 was expressed as $G_{K,end}/G_{K,start}$ ratio ($G_{K,end}$ and $G_{K,start}$ are the averaged K^+ conductances with the presence of the activator in S-ECS at the end and at the beginning of the experiment, respectively), calculated for each cell and plotted as a bar graph (mean ± SEM). Symbols show individual values, numbers in the bar indicate the number of cells. Statistical analysis was performed using one-sample t-test (against H_0:μ_0=1 hypothesis) (**D**). (**D**) contains the pooled data at pH_e = 6.2, 6.5 and 6.7. ****p < 0.0001. Extracellular pH was represented in all cases with the same colors: black for 7.4, green for 6.5 and red for 6.0. The corresponding lighter colors display traces obtained in the presence of the modulator.

of 6.2 while varying the pattern of SKA-31 application. The first experimental "pattern" protocol involved SKA-31 administration at the onset of the experiment, followed by a washout phase (**Figure 24A**). Subsequently, the cell underwent repeated depolarization using voltage ramps every 10 seconds for 400 seconds in the absence of SKA-31. After this interval, SKA-31 was reapplied, yet it failed to potentiate the current to the same extent as observed during its initial application to this cell.

The $G_{K,end}/G_{K,start}$ ratio (**Figure 24B**) is significantly below 1, indicating a decrease in the potentiation of K^+ conductance by the end of the experiments. Consequently, the loss-of-potency phenotype persists despite the introduction of a drug-free period into the protocol, during which voltage ramps are repeatedly applied. In the second special "pattern" protocol

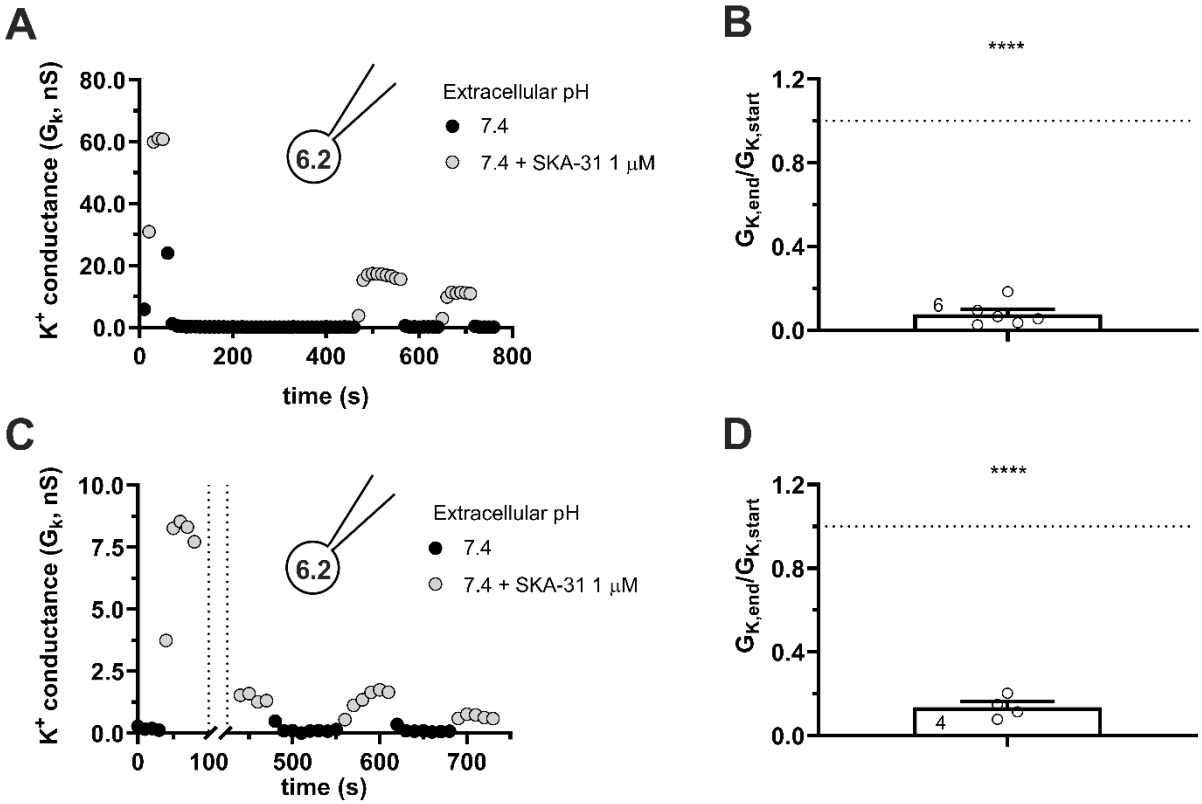

Figure 24. **Progressive loss of the potency of SKA-31 in activating K_{Ca}3.1 currents during special SKA-31 administration protocols**. K_{Ca}3.1 current traces were evoked by 150-ms-long voltage ramps, ranging from −120 to +50 mV in whole-cell patch-clamped CHO cells transfected with K_{Ca}3.1 channels. Voltage ramps were repeated every 10 seconds, the holding potential was −85 mV between pulses. The pipette filing solution was based on the 6.5-ICS-250 solution except that the pH_i was titrated to 6.2, the extracellular solution was S-ECS with or without 1 μM SKA-31 as indicated. (**A**) Representative time course of the effect of SKA-31 when the application of SKA-31 was interrupted for 400 s. (**B**) Loss of the potency of SKA-31 was expressed as $G_{K,end}/G_{K,start}$ ratio ($G_{K,end}$ and $G_{K,start}$ are the averaged K^+ conductances with the presence of the activator in S-ECS at the end and at the beginning of the experiment, respectively), calculated for each cell and plotted as a bar graph (mean ± SEM). Symbols show individual values, numbers in the bar indicate the number of cells. Panel **B** refers to panel **A**. (**C**) Representative time course of the effect of SKA-31 when the application of the voltage ramps was interrupted for 360 s in the continuous presence of 1 μM SKA-31. (**D**) Loss of the potency of SKA-31 relative to panel **C**. Except the pulse protocol, all other details are the same as in Panel **B**. Panel **D** refers to panel **C**. Statistical analysis was performed using one-sample t-test (against H_0:μ_0=1 hypothesis) (**B**, **D**). ****$p < 0.0001$.

(**Figure 24C**), the K_{Ca}3.1 conductance was initially potentiated by SKA-31 application. Following this, while the solution containing SKA-31 was continuously perfused onto the cell, the delivery of voltage ramps was halted for 360 seconds, and the cell was maintained at a holding potential of −85 mV during this interval. Subsequently, the voltage ramps were resumed. **Figure 24C** illustrates that the SKA-31-induced K_{Ca}3.1 conductance was considerably reduced after the interruption in recording compared to the beginning of the experiment. The $G_{K,end}/G_{K,start}$ ratio (**Figure 24D**) is markedly below 1, unequivocally affirming the loss-of-potency phenotype by the conclusion of the experiments. Consequently, neither the incorporation of a voltage-ramp-free period nor a drug-free period into the protocol can forestall

the decline in the potency of SKA-31. This suggests that the loss-of-potency phenotype must be ascribed to the acidic pH_i.

5.2.5 $K_{Ca}2.2$ activation is sensitive to intracellular pH_i similarly to $K_{Ca}3.1$

$K_{Ca}2.x$ channels, akin to $K_{Ca}3.1$, are triggered by intracellular Ca^{2+} and respond to the same modulators (200). However, $K_{Ca}2.x$ channels exhibit approximately tenfold lower sensitivity to compounds such as Riluzole and SKA-31. We selected $K_{Ca}2.2$ as the representative channel from this family and evaluated the efficacy of SKA-31 at a higher concentration of 5 µM in activating the current under neutral and acidic intracellular pH conditions. At a pH_i of 7.2 (**Figure 25A, B**), robust activation of $K_{Ca}2.2$ by SKA-31 could be consistently induced with minimal decline in the modulator's effectiveness over time. Conversely, when the intracellular solution was adjusted to pH_i=6.5, a rapid and irreversible decline in the potency of SKA-31 to activate $K_{Ca}2.2$ was observed (**Figure 25C**, **D**), mirroring the findings observed for $K_{Ca}3.1$.

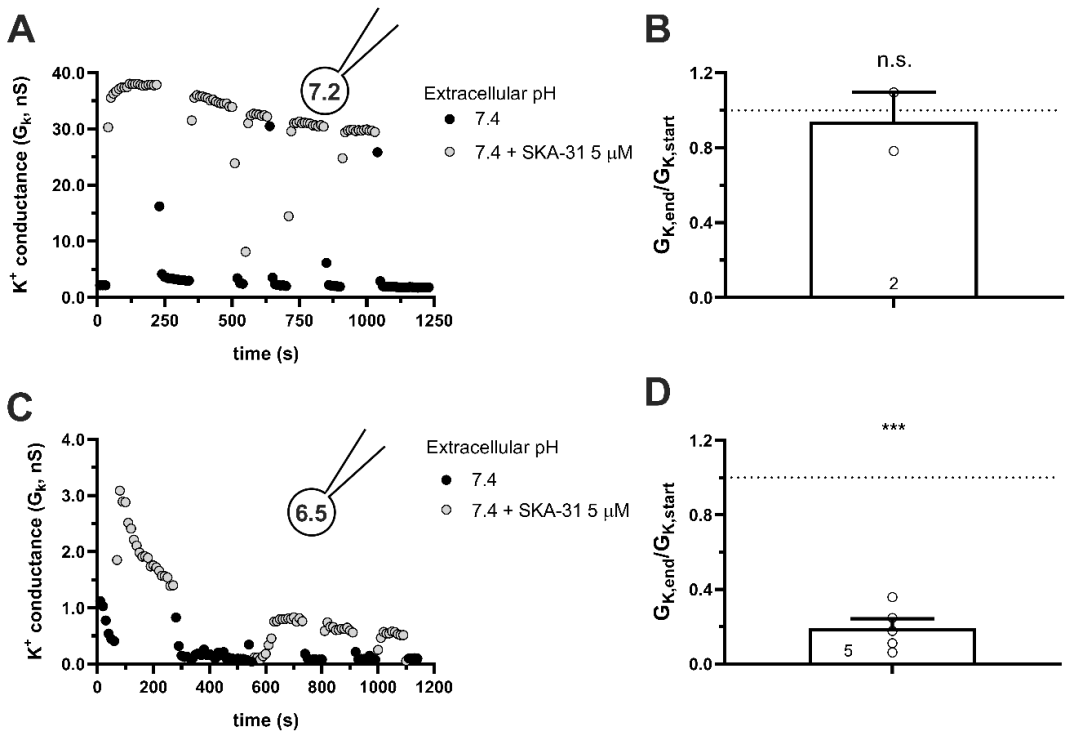

Figure 25. **Effect of SKA-31 on currents generated in CHO cells transfected with h$K_{Ca}2.2$ and GFP at different intracellular pH**. (**A**, **C**) $K_{Ca}3.1$ current traces were evoked by 150-ms-long voltage ramps, ranging from –120 to +50 mV in whole-cell patch-clamped CHO cells transfected with $K_{Ca}3.1$ channels. Voltage ramps were repeated every 10 seconds, the holding potential was –85 mV between pulses. The pipette filing solution was either pH_i=7.2 (7.2-ICS-250) (**A**) or pH_i=6.5 (6.5-ICS-250) (**C**). The extracellular solution was S-ECS with or without 5 µM SKA-31 as indicated. (**B**, **D**) Loss of the potency of SKA-31 was expressed as $G_{K,end}/G_{K,start}$ ratio ($G_{K,end}$ and $G_{K,start}$ are the averaged K^+ conductances with the presence of the activator in S-ECS at the end and at the beginning of the experiment, respectively), calculated for each cell and plotted as a bar graph (mean ± SEM). Symbols show individual values, numbers in the bar indicate the number of cells. **B** refers to **A** and **D** refers to **C**. Statistical analysis was performed using one-sample t-test (against H_0:μ_0=1 hypothesis) (**B**, **D**). ***p < 0.001, n.s., not significant (p > 0.05).

5.2.6 Mutations H192A in hK$_{Ca}$3.1 and T79D in CaM do not influence the loss-of-potency phenotype at acidic intracellular pH

Protonation of histidine residues in acidic environments can disrupt the ability of toxins to bind to ion channels, making the toxins less or non-functional (201). The recent cryo-EM-derived structure of hK$_{Ca}$3.1 unveiled the involvement of the S4-S5 linker in establishing both the functional and structural connection between Calmodulin and the C-terminal portion of the K$_{Ca}$ channels (202). His192 residue, situated within this linker, is positioned near the pocket where activators are believed to exert their influence. Substituting this histidine with a non-charged alanine (H192A) led to the disruption of the interaction between BA6b9, a K$_{Ca}$3.1 blocker designed to share structural similarities with Riluzole/1-EBIO, and K$_{Ca}$3.1 (203).

Given the structural resemblance between BA6b9 and the modulators utilized in this investigation, along with their compatibility with overlapping binding sites, we examined whether the H192A mutation would impact the activation of hK$_{Ca}$3.1 by SKA 31 under both neutral and acidic conditions. As depicted in **Figure 26A**, SKA-31 activated the H192A-K$_{Ca}$3.1 current in a reversible manner, akin to wild-type K$_{Ca}$3.1. The cycles of wash-in and wash-out could be repeated numerous times when the intracellular solution was adjusted to pH 7.2. The efficacy of SKA-31 in activating the current remained relatively stable over prolonged durations (**Figure 26B**). However, at pH$_i$ 6.5, SKA-31 gradually lost its effectiveness in activating the H192A-K$_{Ca}$3.1 current upon repeated administration (**Figure 26C and D**). This indicates that the loss of SKA-31-mediated potentiation of the current at acidic intracellular pH is independent of whether the protonated His or the neutral Ala is present at position 192.

CaM maintains constitutive binding to K$_{Ca}$ channels (202), requiring membrane-bound PIP$_2$ as a co-agonist in addition to Ca^{2+} ions (203). Thr79 within CaM serves as a substrate for Casein Kinase-2 (CK2) (204). Phosphorylation of Thr79 results in diminished sensitivity of the K$_{Ca}$2.2 channel to both PIP$_2$ (205) and Ca^{2+} (206). This phosphorylation can be mimicked by the phosphomimetic mutation T79D, which decreases K^+ current in both K$_{Ca}$2.2 (205) and K$_{Ca}$3.1 (203). The altered network of activators and co-activators in the presence of T79D-CaM may impact the modulation of K$_{Ca}$3.1 activation by SKA-31 under acidic pH$_i$ conditions. To investigate this, we co-transfected hK$_{Ca}$3.1 and T79D-CaM into CHO cells and assessed the potentiation of the whole-cell current at neutral and acidic pH$_i$. As illustrated in **Figure 27A**, under neutral pH$_i$ conditions, the current could be activated by SKA-31 similar to cells transfected with hK$_{Ca}$3.1 only. Activation cycles by SKA-31 resulted in consistent increases in the K^+ conductance over extended periods (**Figure 27B**). Conversely, when pH$_i$=6.5 was employed, SKA-31 gradually lost its potency over time in activating G$_K$ (**Figure 27C**).

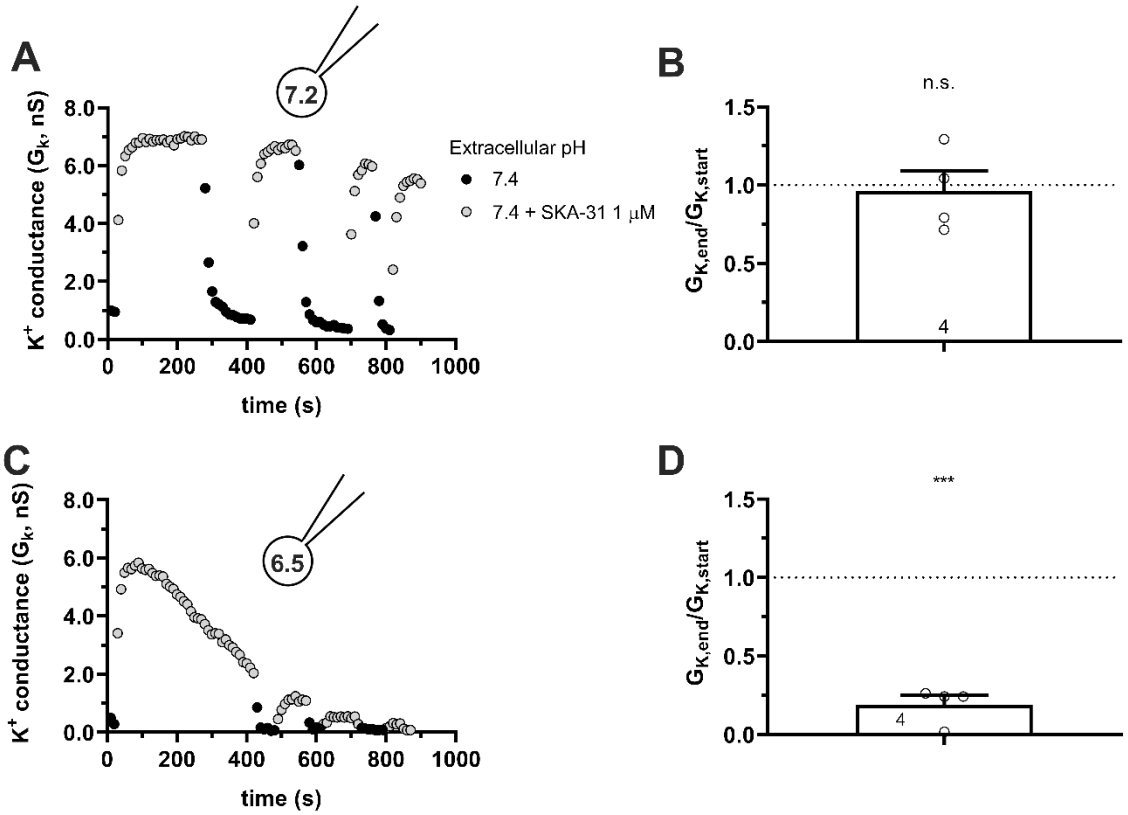

Figure 26. **Effect of SKA-31 on currents generated in CHO cells transfected with the mutated H192A-hK$_{Ca}$3.1 and GFP at different intracellular pH**. (**A**, **C**) K$_{Ca}$3.1 current traces were evoked by 150-ms-long voltage ramps, ranging from –120 to +50 mV in whole-cell patch-clamped CHO cells transfected with K$_{Ca}$3.1 channels. Voltage ramps were repeated every 10 seconds, the holding potential was –85 mV between pulses. The pipette filing solution was either pH$_i$=7.2 (7.2-ICS-250) (**A**) or pH$_i$=6.5 (6.5-ICS-250) (**C**). The extracellular solution was S-ECS with or without 1 μM SKA-31 as indicated. (**B**, **D**) Loss of the potency of SKA-31 was expressed as $G_{K,end}/G_{K,start}$ ratio ($G_{K,end}$ and $G_{K,start}$ are the averaged K^+ conductances with the presence of the activator in S-ECS at the end and at the beginning of the experiment, respectively), calculated for each cell and plotted as a bar graph (mean ± SEM). Symbols show individual values, numbers in the bar indicate the number of cells. **B** refers to **A** and **D** refers to **C**. Statistical analysis was performed using one-sample t-test (against H_0:μ_0=1 hypothesis) (**B**, **D**). ***p < 0.001, n.s., not significant (p > 0.05).

Although the average loss of G_K (**Figure 27D**) by the experiment's end (>800 s) was slightly reduced compared to CHO cells transfected with wild-type (**Figure 23D**) or H192A K$_{Ca}$3.1 constructs (**Figure 26D**), the $G_{K,end}/G_{K,start}$ ratio did not significantly differ among the three groups (One-way ANOVA, p>0.05). Additionally, some cells exhibited a very slow restoration of SKA-31 potency over time (**Figure 27C**). This phenomenon was not further investigated due to the inherent limitations of whole-cell patch-clamp techniques over prolonged durations exceeding 15-20 minutes.

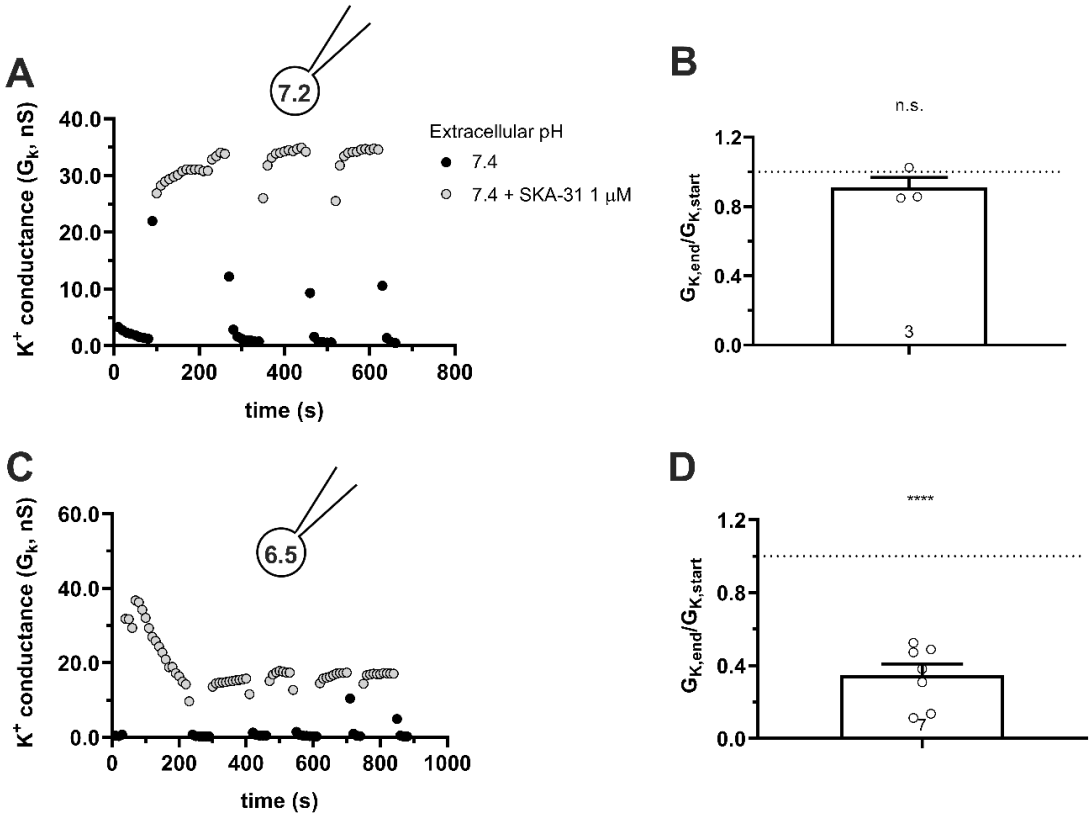

Figure 27. **Effect of SKA-31 on currents generated in CHO cells transfected with turboGFP-hK_{Ca}3.1 and the mutated T79D-CaM at different intracellular pH**. (**A**, **C**) K_{Ca}3.1 current traces were evoked by 150-ms-long voltage ramps, ranging from −120 to +50 mV in whole-cell patch-clamped CHO cells transfected with KCa3.1 channels. Voltage ramps were repeated every 10 seconds, the holding potential was −85 mV between pulses. The pipette filing solution was either pH_i=7.2 (7.2-ICS-250) (**A**) or pH_i=6.5 (6.5-ICS-250) (**C**). (**B**, **D**) Loss of the potency of SKA-31 was expressed as $G_{K,end}/G_{K,start}$ ratio ($G_{K,end}$ and $G_{K,start}$ are the averaged K^+ conductances with the presence of the activator in S-ECS at the end and at the beginning of the experiment, respectively), calculated for each cell and plotted as a bar graph (mean ± SEM). Symbols show individual values, numbers in the bar indicate the number of cells. **B** refers to **A** and **D** refers to **C**. Statistical analysis was performed using one-sample t-test (against H_0:μ_0=1 hypothesis) (**B**, **D**). ****p < 0.0001, n.s., not significant (p > 0.05).

5.2.7 High intracellular Ca^{2+} concentration hinders the inhibitory effect of intracellular acidity

K_{Ca}3.1 is extremely sensitive to intracellular calcium concentrations, with an EC_{50} ranging from 100 to 400 nM (26) and a typical sigmoidal activation curve (207) (see **Figure 3A**). When SKA-31 was administered to hK_{Ca}3.1-expressing CHO cells and a 1 µM Ca^{2+} concentration was used in the pipette at a pH_i of 7.2, we observed: 1) an increased baseline K_{Ca}3.1 conductance due to the elevated intracellular calcium levels (**Figure 28A, B**) and 2) a reduced potentiation of G_K by SKA-31 (approximately 2-fold compared to approximately 50-fold at a cytosolic Ca^{2+} concentration of 250 nM), attributable to the near-saturation levels of channel calcium sensitivity. Intriguingly, at a cytosolic Ca^{2+} concentration of 1 µM, the effectiveness of SKA-31 in enhancing K_{Ca}3.1 conductance was maintained at acidic pH_i=6.5 (**Figure 28B**). The $G_{K,end}/G_{K,start}$ parameter obtained at pH_i=6.5 and 1 µM Ca^{2+} did not show

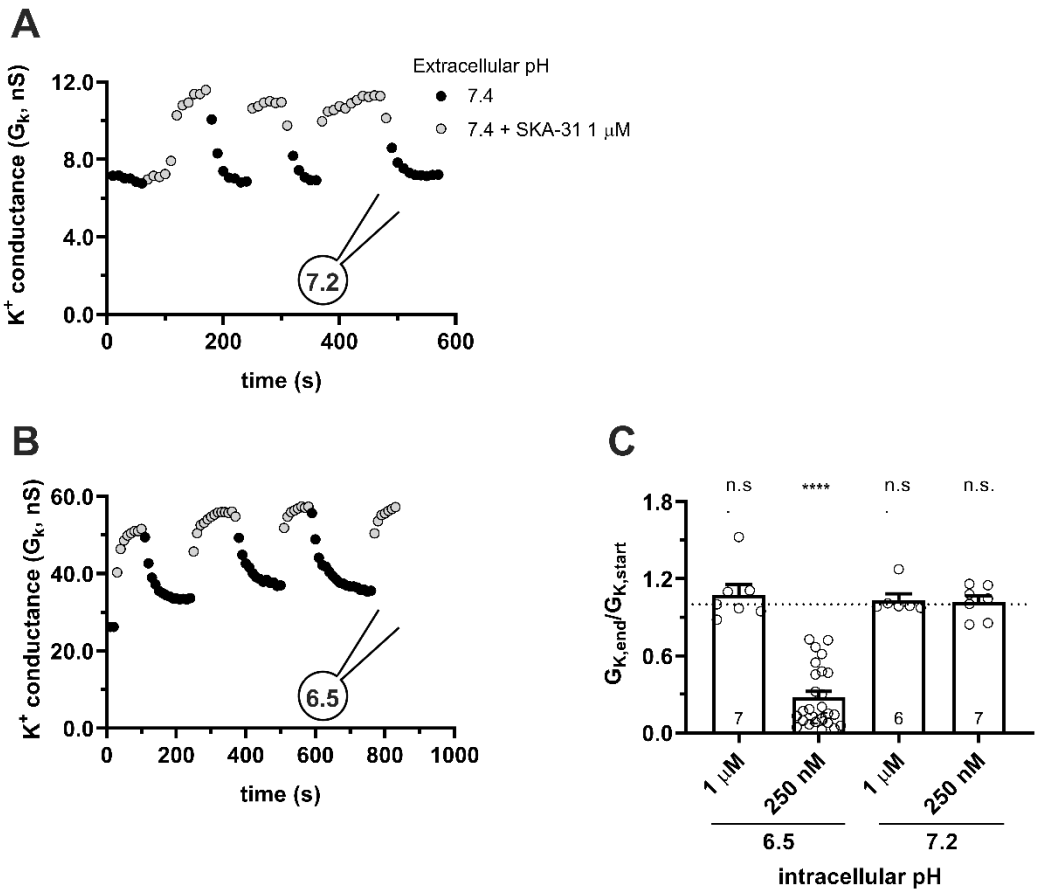

Figure 28. **High intracellular Ca^{2+} (1 μM) sustains the functionality of SKA-31**. (**A**, **B**) $K_{Ca}3.1$ current traces were evoked by 150-ms-long voltage ramps, ranging from −120 to +50 mV in whole-cell patch-clamped CHO cells transfected with $K_{Ca}3.1$ channels. Voltage ramps were repeated every 10 seconds, the holding potential was −85 mV between pulses. The pipette filing solution was at pH_i=6.5 and 1 μM Ca^{2+} (6.5-ICS) (**A**) and at pH_i=7.2 and 1 μM Ca^{2+} (S-ICS) (**B**). The extracellular solution was S-ECS with or without 1 μM SKA-31 as indicated. (**C**) Loss of the potency of SKA-31 was expressed as $G_{K,end}/G_{K,start}$ ratio ($G_{K,end}$ and $G_{K,start}$ are the averaged K^+ conductances with the presence of the activator in S-ECS at the end and at the beginning of the experiment, respectively), calculated for each cell and plotted as a bar graph (mean ± SEM). Symbols show individual values, numbers in the bar indicate the number of cells. Statistical analysis was performed using one-way ANOVA (against H_0:μ_0=1 hypothesis) with multiple comparison (Bonferroni) (**C**). ****p < 0.0001. n.s., not significant (p > 0.05).

statistically significant differences compared to the data obtained at pH_i=7.2 at either 1 μM or 250 nM cytosolic Ca^{2+} concentration (**Figure 28C**). This suggests that at saturating intracellular calcium concentrations the efficacy of SKA-31 in activating $K_{Ca}3.1$ remains constant regardless of the pH_i.

6 DISCUSSION

6.1 The voltage-gated H_v1 H^+ channel is expressed in tumor-infiltrating myeloid-derived suppressor cells

In this part of the dissertation we present, for the first time, evidence that murine MDSCs isolated directly from tumor tissue express the H_v1 channel both at the mRNA and protein levels. Furthermore, we found that the characteristics of the whole-cell current in MDSCs derived from tumors closely resemble the features of H_v1 currents observed in various cell types and in cells expressing H_v1 heterologously. These features include voltage-dependent activation, a ~40 mV shift in the activation threshold of the current per unit change in extracellular pH, as extensively reviewed by (208), and high selectivity for H^+ ions, as well as sensitivity to the guanidine derivative ClGBI (209).

A key novelty of our study is that the expression of H_v1 was shown in MDSCs obtained from tumors. As outlined in the introduction, the LLC tumor model in mice proved to be a suitable source for isolating MDSCs. LLC tumors are typically characterized as immunologically "cold" tumors (185), marked by high infiltration of MDSCs and an immunosuppressive microenvironment (210). While MDSCs are a focal point in tumor immunology and subject to intensive investigation, there is still no consensus on the phenotypic definition of these cells. In mice, Mo-MDSCs are typically defined as $CD11b^+Ly6C^+$ and PMN-MDSCs as $CD11b^+Ly6G^+Ly6C^{low}$, although these markers commonly define other subsets of myeloid cells as well (211). Recognizing the limitations in identifying these cells solely based on cell surface markers, we utilized immunofluorescence to demonstrate the presence of both PMN-MDCSs and Mo-MDSCs in LLC tumors induced in mice. Furthermore, Mo-MDSCs can be distinguished from tumor-associated macrophages (TAMs) due to their lower expression of F4/80 (186). This distinction was utilized in flow cytometric separation and specific enrichment of MDSCs for electrophysiological investigations. Our findings revealed that tumor-derived PMN-MDSCs were the most prevalent subset in LLC tumors, detected by flow cytometry approximately six times more frequently than Mo-MDSCs. This prevalence is consistent with similar tumor types (212,213), and comparable proportions have been reported in pancreatic ductal adenocarcinoma (PDAC) (213) and autoimmune diseases such as autoimmune arthritis (214).

Due to the complexity in defining MDSCs solely based on membrane markers, it is a common practice to confirm the identity of these cells through functional studies. Typically, this involves demonstrating their ability to suppress T cell proliferation to avoid confusion with phenotypically similar monocytes and neutrophils (186). In our investigation, we found that

tumor-derived Mo-MDSCs exhibited T-cell suppressive activity, while PMN-MDSCs, despite their higher abundance, did not demonstrate such suppression, at least under the MDSC/splenocyte ratios utilized in our experiments. This lack of anti-proliferative behavior in PMN-MDSCs aligns with findings from other studies conducted in LLC tumors in mice (187,215) and has also been observed in contexts such as PDAC (216), autoimmune arthritis (214), and MDSCs found in transplanted organs in humans (217). However, PMN-MDSCs may still promote tumor growth by inhibiting cytolytic T cell activation directly and indirectly influencing other myeloid cells and natural killer cells (NKs) (218,219). They are known to be the primary source of immunosuppressive mediators like ROS and RNS, which dampen TCR signaling and regulate cytokine secretion (219,220). Furthermore, PMN-MDSCs hinder the recruitment of cytolytic T cells (221) and contribute to tumor progression by releasing MMPs and factors that facilitate tumor angiogenesis (222). Moreover, a recent electrophysiological study provides strong evidence that the cells classified as PMN-MDSCs in our study are distinct from neutrophils. Immler and colleagues demonstrated through electrophysiological assays that neutrophil polymorphonuclear leukocytes functionally express voltage-gated $K_v1.3$ K^+ channels (223), a feature notably absent in our whole-cell recordings of MDSCs, where $K_v1.3$ or any other voltage-gated K^+ current was not detected.

Several lines of evidence support that whole-cell H_v1 currents were recorded in tumor-derived Mo- and PMN-MDSCs in our study. First, the currents were slowly activating, rapidly deactivating, and with no sign of inactivation, which is characteristic of H_v1 (208,224). Moreover, the currents were recorded using intra- and extracellular solutions that lacked (K^+, Na^+) or contained negligible concentration (Cl^-) of conventional permeating ions; thus, the contribution of other conductances to the whole-cell current, that could mimic the behavior of H_v1, are minimized.

Second, the whole-cell currents observed in both types of MDSCs were influenced by the pH gradient across the membrane and the membrane potential. The threshold voltage required for the activation of these currents shifted along the voltage axis in response to changes in ΔpH, approximately 40 mV per unit change in extracellular pH, closely resembling previous descriptions of proton currents in various cell types (208), including bone marrow-derived MDSCs (190). However, the threshold voltage (V_{thr}) of these currents varied among different cell types (76,225). For instance, under identical pH gradients (ΔpH = 1.2) and recording conditions, the H_v1 current in human chorion-derived mesenchymal cells activated at a membrane potential ~10 mV more positive than that of hH_v1 expressed in HEK-293 cells (76). In contrast, the V_{thr} values observed in both types of MDSCs in our study were approximately 10 mV more negative than that of hH_v1 in HEK-293 cells. This more negative threshold

potential may facilitate the opening of H_v1 channels at membrane potentials within the physiological range typically observed for non-excitable cells. However, the V_{thr} values determined in our study were more positive than the reversal potentials of the H^+ currents obtained over a wide range of ΔpH values, thus allowing the H_v1 channel to conduct protons solely in the outward direction, similar to other cell types (208). Additionally, we observed that the V_{thr} in PMN-MDSCs was depolarized compared to Mo-MDSCs under symmetrical pH conditions ($pH_e \sim pH_i$), although this did not affect the overall V_{thr}–ΔpH relationship of approximately –40 mV per one unit ΔpH change (226). The V_{thr} of approximately +40 mV in symmetric solutions in PMN-MDSCs is qualitatively similar to that determined for the H_v1 current in murine neutrophil granulocytes (approximately +50 mV, (227)), which are closely related to PMN-MDSCs. Moreover, specific mutations introduced in the hH_v1 channel significantly altered V_{thr} without affecting the V_{thr}-ΔpH relationship (228). However, it remains uncertain whether our observations stem from technical errors primarily due to the extremely low ion currents in Mo-MDSCs or from translational or post-translational differences between H_v1 in PMN- and Mo-MDSCs.

Third, the H_v1 current observed in PMN-MDSCs exhibits a notable selectivity for H^+, as evidenced by the E_{rev}-ΔpH relationship closely resembling the theoretical relationship predicted for H^+ ions from the Nernst equation. While the slope of the E_{rev}-ΔpH relationship in rat alveolar epithelial cells (229) and canine myocytes (230) mirrors the theoretical slope calculated from the Nernst equation for H^+ ions (~ −59 mV per one unit ΔpH change), the slopes observed in Jurkat cells (−47 mV per one unit ΔpH change, (231)) and in MDSCs in our study (−42 mV per one unit ΔpH change) are shallower. A similar discrepancy has been noted in murine microglia, where it was proposed that proton depletion, resulting from the passage of proton current through H_v1 channels, may contribute to the shallower slope (232). Moreover, the small currents observed in MDSCs are susceptible to contamination by non-specific leakage, even with applied leak corrections; any contribution of leakage to the whole-cell current shifts the reversal potentials towards depolarized potentials. The challenges arising from incomplete leakage subtraction precluded the reliable determination of the reversal potential in Mo-MDSCs, where currents are exceedingly small, often less than 100 pA even under optimal ΔpH and membrane potential conditions.

Fourth, the currents observed in both PMN-MDSCs and Mo-MDSCs demonstrated sensitivity to ClGBI, a guanidine derivative small molecule inhibitor of H_v1 (209). Although the ClGBI is a very unselective drug (96), it is commonly utilized as an indicator of H_v1 current presence in various cell types (76,104,230). We demonstrated that ClGBI at a concentration of 200 μM reversibly blocked approximately 80% of the whole-cell currents in both PMN- and

Mo-MDSCs. Based on the observed block percentage and assuming a sigmoidal dose-response function with a Hill coefficient of 1, the single-point estimate of the IC_{50} is approximately 50 μM, which aligns with the reported potency of ClGBI in inhibiting H_v1 (209,230). This pharmacological evidence further supports our conclusion that these currents correspond to proton currents mediated by H_v1 in MDSCs.

Fifth, the electrophysiological findings are strongly corroborated by molecular biology analyses, where the mRNA transcript of H_v1 was identified in MDSCs using RT-qPCR, along with the H_v1 protein itself being detected in Western blots. The human H_v1 proton channel protein exhibits two isoforms: a long, full-length isoform and a shorter variant lacking an N-terminal region due to alternative splicing (233). The antibody utilized in our study recognizes both isoforms, a fact confirmed in the CH12 mouse B cell lymphoma cell line used as a positive control in our investigation, as well as in human B cell lymphomas reported previously (233). However, we observed only the long form in both PMN-MDCS and Mo-MDSCs isolated from the LLC tumor. The absence of the short form suggests that it may not be expressed or may be present in negligible amounts below the detection limit, indicating that the long isoform of Hv1 likely contributes to the functionality of tumor-derived MDSCs.

While the H_v1 proton channel has been extensively characterized in various immune cell types, to our knowledge, there is a lack of information regarding H_v1 expression in tumor-associated inflammatory cells. Our study, for the first time, identified a substantial population of H_v1^+ myeloid cells within a tumor, consistent with the cell surface marker phenotype of PMN- and Mo-MDSCs (as described above). Our electrophysiology findings are in line with data reported for in vitro-generated MDSCs, where H_v1 currents of comparable magnitude (ranging between 200 pA and 1 nA at +130 mV) were observed using the patch-clamp technique in a mixed MDSC population (190). The MDSCs utilized by Alvear-Arias et al. were generated through the differentiation of bone marrow-derived myeloid precursors induced by GM-CSF (190), while in our study, MDSCs were directly isolated from LLC tumors induced in mice. Our findings suggest that in vitro-differentiated MDSCs could serve as valuable tools for investigating H_v1-dependent regulation of T cell function in cancer, given the similarity in channel phenotype between these cells and tumor-derived MDSCs regarding H_v1 expression. Additionally, we demonstrated that both PMN- and Mo-MDSCs exhibit H_v1-mediated H^+ currents, albeit to varying degrees, indicating that the ion channel phenotype of the two MDSC subtypes is comparable, at least in mice.

What could be the functional implications of H_v1-mediated H^+ currents in MDSCs? Neutrophils, which share close similarities with MDSCs, express functional H_v1, and these H^+ currents play a role in balancing positive charge efflux necessary for sustaining ROS production

(234). Given that ROS production is also a hallmark of MDSCs' immunosuppressive activity (235), the functional expression of H_v1 in MDSCs and its susceptibility to H_v1 inhibitors appears reasonable. Consistent with this notion, electrophysiological studies have demonstrated H_v1-mediated H^+ currents in MDSCs ((190) and this study) and blocking H_v1 using inhibitors like ClGBI and Zn^{2+} has been shown to inhibit ROS production and alleviate the suppression of T cell proliferation by MDSCs (190). However, prolonged exposure of MDSCs to H_v1 inhibitors for more than 2 hours resulted in significant cell death, raising concerns about the specificity of ClGBI's effects. This, coupled with the administration of a reversible blocker (ClGBI) during short-term pre-incubation of MDSCs followed by wash-out, complicates the interpretation of data from T cell/MDSC co-culture experiments. In our experiments, ClGBI applied alone, without MDSCs, inhibited T cell proliferation, precluding the use of T cell/MDSC co-culture experiments in the presence of ClGBI (96). The potential adverse effects of currently available H_v1 inhibitors underscore the necessity for the development of more specific and higher-affinity H_v1 inhibitors.

The proton efflux facilitated by the H_v1 proton channel might additionally contribute to the acidic environment within the TME, a condition that tumor cells can tolerate well but which hinders the tumor-suppressive capabilities of T cells and NK cells (236). Consequently, regulating the acidity of the tumor microenvironment through H_v1 inhibition could potentially enhance the anti-tumor actions of immune cells in cancer therapy. However, recent findings have also indicated that the heightened intracellular acidity in activated T cells resulting from the absence of the H_v1 proton channel diminishes the effector function of these T cells (237). This aspect must also be considered when evaluating the overall efficacy of H_v1-targeted cancer therapy. Moreover, changes in the extracellular and intracellular pH may influence the operation of the ion channels of immune cells, cancer cells and other cellular components of the TME (238,239). As ion channels in cancer cells and cellular components of the TME are attractive pharmacological targets to treat cancer, it bears outmost importance to determine the effectiveness of ion channel modulators under the very special intra- and extracellular pH and ionic milieu characteristic for the TME (240,241). One aspect of this was also investigated in the dissertation and discussed below (242).

6.2 Intracellular acidity impedes $K_{Ca}3.1$ activation by Riluzole and SKA-31

This part of my dissertation is, to our knowledge, the first comprehensive study that analyzes how extra- and intracellular pH influences the magnitude of the $hK_{Ca}3.1$ current and its potentiation by the positive modulators of the channel SKA-31 and Riluzole. We showed

that the hK_{Ca}3.1 current expressed endogenously in human peripheral blood lymphocytes or expressed heterologously in CHO cells shows very subtle sensitivity to the pH_i ranging from 6.5 to 8.0 and pH_e ranging from 6.0 to 8.0. The very potent activators of K_{Ca}3.1, Riluzole and SKA-31, induce robust K_{Ca}3.1 currents at normal (pH_i = 7.2) and alkaline (pH_i = 8.0) intracellular pH for both endogenously and heterologously expressed channels. On the other hand, the potency of SKA-31 in activating the K_{Ca}3.1 current declines over time when the intracellular pH is acidic (pH_i < 6.5). The loss of the potency of SKA-31 was not specific for K_{Ca}3.1, the potentiation of the current also declined over time when K_{Ca}2.2 was studied at pH_i = 6.5. The loss of the SKA-31 potency at acidic pH_i was also shown for a K_{Ca}3.1 mutant where a titratable His was mutated to Ala (H192A) near the binding pocket for the activators. Similarly, transfection of CHO with T79D, a Calmodulin mutant that confers reduced Ca^{2+} sensitivity to K_{Ca}3.1, did not prevent the loss-of-potency phenotype when SKA-31 was applied at acidic pH_i. However, increasing the cytosolic Ca^{2+} concentration to 1 µM eliminated the loss-of-potency phenotype of SKA-31 activation at acidic pH_i.

The reliance of K^+ conductance on extracellular pH likely stems from multiple factors. One possibility is associated with the alteration of surface charges when the H^+ concentration increases upon decreasing the extracellular pH (pH_e). This alteration can impact the function of the voltage sensor domain (VSD) in voltage-gated channels, as evidenced in studies on Shaker (243) and K_v1.3 (244,245) channels. Unlike voltage-gated channels, K_{Ca}3.1 lacks the charges in the S4 helix of the VSD characteristic for other voltage-gated ion channels. Consistent with this K_{Ca}3.1 does not operate as a voltage-gated ion channel (246). Hence, the absence of an effect of pH_e on K^+ conductance in K_{Ca}3.1 is not unexpected. Additionally, pH_e can regulate ion channels by specifically interacting with exposed titratable amino acid residues. This phenomenon has been observed in Na^+-permeable ASIC ion channels (247,248). Notably, acidic extracellular pH can significantly influence the conductance, inactivation kinetics, and pharmacology of K_v1.3 due to the presence of a titratable His residue in the channel's pore entrance (177,245,249). However, the human K_{Ca}3.1 channel contains a valine at a corresponding position (V257). While there are titratable amino acid residues near the selectivity filter of K_{Ca}3.1, such as H236 and D239, and even if these become protonated at acidic pH_e, they do not notably affect the K^+ conductance of K_{Ca}3.1 channels. Acidic pH_e notably decreases K^+ currents through hK_{Ca}3.1, although the reduction in current never exceeds 15%–20% compared to pH_e = 7.4. Moreover, this effect is primarily observed at extracellular pH 6.0, which is exceedingly low and may represent the lower extreme in pathological context.

pH alterations also impact several voltage-gated K^+ channels. For instance, in peripheral blood lymphocytes (PBLs), the whole-cell K_v1.3 current was augmented by alkaline pH and

suppressed by acidic pH (245). This sensitivity to pH changes was ascribed to modifications in both the number of channels opening and the single-channel conductance. In Shaker-IR K^+ channels, a decrease in current at acidic pH results from a reversible blockade of the channels by protons (250). This proton blockade of Shaker IR channels was accompanied by a notable decline in the single-channel current, and it was proposed that protons interact specifically with amino acid side chains within the channels' internal vestibule, although the specific side chains involved were not identified. Despite the structural similarities between K_v channels and $K_{Ca}3.1$, such as the presence of a cytoplasmic activation gate at Val282 and a selectivity filter, the influence of pH on $K_{Ca}3.1$ conductance is nearly absent, as demonstrated in our investigation.

Based on the lack of sensitivity of the $K_{Ca}3.1$ current to variations in both intracellular and extracellular pH, we infer that the gating mechanism of $K_{Ca}3.1$ (202) and the network of co-activators (Ca^{2+}, CaM, and PIP_2) remain unaffected by pH levels relevant to both physiological and pathophysiological conditions. This conclusion appears to contradict earlier research that demonstrated pH sensitivity in the shape (251), Ca^{2+} binding capacity (252), and Ca^{2+} affinity (253) of CaM. These contrasting outcomes may stem from previous studies utilizing isolated CaM in solution or employing mathematical models, which could account for the discrepancy with our findings.

Voltage- and Ca^{2+}-activated channels are susceptible to inhibition by small molecules and/or peptide blockers. A notable pharmacological property of $K_{Ca}3.1$ is its responsiveness to a group of small molecules derived from the structure of EBIO-1 (254), which act as channel activators. These activators can be employed experimentally to enhance channel function, thereby influencing cellular responses under physiological and pathophysiological conditions (as discussed below). The mechanism of action of these activators involves shifting the calcium-activation curve towards lower intracellular Ca^{2+} concentrations in a concentration-dependent manner, consequently increasing the apparent Ca^{2+} affinity. However, they are incapable of activating the channels in the absence of intracellular Ca^{2+}. Thus, while they function as positive-gating modulators, they also exhibit a super-agonist effect by activating the current even when cytosolic Ca^{2+} concentrations are saturating, as demonstrated by the activation of $K_{Ca}3.1$ by SKA-31 at a concentration of 1 µM Ca^{2+}. Considering the structures of Riluzole and SKA-31 and their predicted pK_a values (2.96 and 3.5), their protonation status is minimally affected within the pH range of 6.0 to 8.0. Consistent with this, both SKA-31 and Riluzole enhance the $K_{Ca}3.1$ current across all combinations of pH_e-pH_i, as long as the intracellular pH remains neutral or basic.

In contrast, when the intracellular pH was acidic, both SKA-31 and Riluzole demonstrated a decline in their ability to activate $K_{Ca}3.1$ over the duration of several hundred seconds in our experiments. One possible explanation for this loss of potency could be that exposure to acidic intracellular pH induces an irreversible structural change in the activator molecules over the extended duration of the experiments. However, our data suggest otherwise. Both Riluzole and SKA-31 maintained their effectiveness when dissolved in an extracellular solution with a pH of 6.0. Throughout the day, all extracellular solutions, including those containing SKA/Riluzole at pH 6.0, retained the potency of the activators. Furthermore, upon immediate application of SKA-31 or Riluzole, the $K_{Ca}3.1$ current was enhanced even under acidic intracellular pH conditions. This indicates that the access of SKA-31 and Riluzole to the modulatory site, including membrane permeation, remains unhindered regardless of the combination of intracellular and extracellular pH. Additionally, upon exposing the intracellular environment to acidic pH, the decline in SKA-31-mediated current activation progressed when we paused SKA-31 application or interrupted the current recordings for several hundred seconds. The only intervention that prevented this loss of potency was the increase in cytosolic Ca^{2+} concentration to 1 μM.

Another possibility for the reduction in $K_{Ca}3.1$ conductance induced by the activators at acidic intracellular pH could involve a combination of factors. This might include the acidic intracellular pH, low (250 nM) Ca^{2+} concentration, and the presence of activators, which could result in decreased availability of the channels for opening. Further experiments are warranted to explore this hypothesis, which could involve investigating the phosphorylation of His358 in $K_{Ca}3.1$ at different intracellular pH values and its impact on the CaM-dependent activation of the channels (255–258).

While our current investigations into the molecular basis of the loss of $K_{Ca}3.1$ activator potency at acidic intracellular pH remain inconclusive, this phenomenon presents an intriguing area of study with potential implications for experimental applications. Pharmacologically activating $K_{Ca}3.1$ using positive modulators has emerged as a promising strategy to enhance the suppressed immune response against cancer (259,260) (recently reviewed in (261)). This approach holds particular significance for overcoming the immunosuppressive TME, characterized by elevated extracellular K^+ levels (262,263), adenosine concentration (263), and acidity (264).

For instance, activating $K_{Ca}3.1$ channels with 1-EBIO restored the chemotaxis ability of cancer-derived $CD8^+$ T cells in the presence of adenosine (265) and improved T cell function *in vitro* under conditions of high extracellular [K^+] typical of the TME (262,266). Given that the intracellular pH in the acidic TME is also acidic (266), the benefits of $K_{Ca}3.1$ positive

modulators may be compromised by the loss-of-potency phenotype observed at acidic intracellular pH in our study. On the other hand, various cancer types like glioblastoma (260), pancreatic ductal adenocarcinoma (267), prostate cancer (268), non-small cell lung cancer (269), and breast cancer (270) exhibit $K_{Ca}3.1$ overexpression. In these cases, using an activator could potentially be counterproductive and, on the contrary, the loss of potency of activators in the acidic TME may even be advantageous. Therefore, the overall impact of the acidic intracellular pH-induced loss of $K_{Ca}3.1$ activator potency must be carefully assessed for both immune system function and cancer cell behavior.

7 SUMMARY

The tumor microenvironment includes diverse immune cell types immersed in a very complex and hostile system characterized by hypoxia, nutrient deficiency and acidity. Acidity, in particular, will directly affect the functionality of several proteins, among which ion channels. In this PhD dissertation we tested whether $K_{Ca}3.1$, an ion channel essential for lymphocytic activation and proliferation, is affected by changes in extracellular and intracellular pH. We discovered that K^+ currents through $K_{Ca}3.1$ were minimally, but reversibly, altered by a shift in the extracellular pH. Notably, acidic pH_e caused a current drop and basic pH_e caused a current increase. These changes were statistically significant, but never extended beyond ~20% compared to the baseline and could probably be considered physiologically irrelevant. We also enquired into the pH sensitivity of two $K_{Ca}3.1$ activators: Riluzole and SKA-31. These substances have been suggested as possible oncological immune boosters, therefore their relationship with pH should be better characterized. We showed that both Riluzole and SKA-31 activate $K_{Ca}3.1$ in a fast and reversible manner, unfazed by alkaline or acidic extracellular pH. However, when the intracellular pH was shifted to acidic values (6.2-6.7) both Riluzole and SKA-31 lost their potency in a time-dependent and an irreversible manner. We were not able to determine which molecular components contributed to this phenomenon, since mutations of sensitive spots in $K_{Ca}3.1$ (H192A) and in the ion channel-bound Calmodulin (T79D) did not restore the lost potency. However, a high Ca^{2+} intracellular concentration apparently restabilizes the optimal functionality of SKA-31, suggesting a possible role of Calmodulin in this newly discovered phenomenon.

Lymphocytes are not the only immune cells inhabiting the tumor microenvironment. Another important cell type is the myeloid-derived suppressor cell, which has been shown to host H_v1 as its main ion channel. H_v1 is the only H^+ channel in mammals and it is strongly sensitive to changes in pH and ΔpH_{e-i}. However, most of the information we have about H_v1 in myeloid-derived suppressor cells stem from *in vitro*-generated murine cells, which can be different from *in vivo* ones. We obtained tumor-related myeloid-derived suppressor cells after subcutaneously implanting a tumor mass in the flank of C57BL/10 mice and analyzed the expression of H_v1 through Western blotting, qPCR, immunofluorescence and patch clamping. Through patch clamping we showed that these cells do not apparently host other voltage-gated currents except for the H^+ current, which was identified thanks to several biophysical and pharmacological pieces of evidence.

8 KEYWORDS

MDSC

KCa3.1

Hv1

Ion channels

pH

Riluzole

SKA-31

Patch-clamp electrophysiology

Tumor microenvironment

Ion channel modulation

Mutagenesis

9 REFERENCES

1. Xu H, Martinoia E, Szabo I. Organellar Channels and Transporters. *Cell Calcium* (2015) 58:1. doi: 10.1016/J.CECA.2015.02.006
2. Gadsby DC. Ion channels versus ion pumps: the principal difference, in principle. *Nature Reviews Molecular Cell Biology 2009 10:5* (2009) 10:344–352. doi: 10.1038/nrm2668
3. Alberts B, Johnson A, Lewis J, Raff M, Roberts K, Walter P. Ion Channels and the Electrical Properties of Membranes. (2002) https://www.ncbi.nlm.nih.gov/books/NBK26910/ [Accessed June 5, 2023]
4. Volkov V. Quantitative description of ion transport via plasma membrane of yeast and small cells. *Front Plant Sci* (2015) 6:425. doi: 10.3389/FPLS.2015.00425/BIBTEX
5. Ashcroft F, Gadsby D, Miller C. Introduction. The blurred boundary between channels and transporters: We dedicate this volume to the memory of Peter Läuger, a pioneer of the link between channels and pumps. *Philosophical Transactions of the Royal Society B: Biological Sciences* (2009) 364:145. doi: 10.1098/RSTB.2008.0245
6. Maljevic S, Lerche H. Potassium channels: A review of broadening therapeutic possibilities for neurological diseases. *J Neurol* (2013) 260: doi: 10.1007/s00415-012-6727-8
7. O'Grady SM. ION TRANSPORT | Potassium Channels. *Encyclopedia of Respiratory Medicine, Four-Volume Set* (2006)477–482. doi: 10.1016/B0-12-370879-6/00203-9
8. Alexander SPH, Mathie A, Peters JA, Veale EL, Striessnig J, Kelly E, Armstrong JF, Faccenda E, Harding SD, Pawson AJ, et al. THE CONCISE GUIDE TO PHARMACOLOGY 2019/20: Ion channels. *Br J Pharmacol* (2019) 176:S142–S228. doi: 10.1111/BPH.14749
9. Kuang Q, Purhonen P, Hebert H. Structure of potassium channels. *Cellular and Molecular Life Sciences* (2015) 72:3677. doi: 10.1007/S00018-015-1948-5
10. Delaney E, Khanna P, Tu LW, Robinson JM, Deutsch C. Determinants of pore folding in potassium channel biogenesis. *Proc Natl Acad Sci U S A* (2014) 111:4620–4625. doi: 10.1073/PNAS.1324274111/-/DCSUPPLEMENTAL/PNAS.201324274SI.PDF
11. Reddi R, Matulef K, Riederer EA, Whorton MR, Valiyaveetil FI. Structural basis for C-type inactivation in a Shaker family voltage-gated K + channel. (2022). 8804 p.
12. Prole DL, Marrion N V. Identification of putative potassium channel homologues in pathogenic protozoa. *PLoS One* (2012) 7: doi: 10.1371/JOURNAL.PONE.0032264
13. Orfali R, Albanyan N. Ca2+-Sensitive Potassium Channels. *Molecules 2023, Vol 28, Page 885* (2023) 28:885. doi: 10.3390/MOLECULES28020885
14. Wei AD, Gutman GA, Aldrich R, Chandy KG, Grissmer S, Wulff H. International Union of Pharmacology. LII. Nomenclature and Molecular Relationships of Calcium-Activated Potassium Channels. *Pharmacol Rev* (2005) 57:463–472. doi: 10.1124/PR.57.4.9
15. Kshatri AS, Gonzalez-Hernandez A, Giraldez T. Physiological Roles and Therapeutic Potential of Ca2+ Activated Potassium Channels in the Nervous System. *Front Mol Neurosci* (2018) 11:258. doi: 10.3389/FNMOL.2018.00258/BIBTEX
16. Köhler M, Hirschberg B, Bond CT, Kinzie JM, Marrion N V., Maylie J, Adelman JP. Small-Conductance, Calcium-Activated Potassium Channels from Mammalian Brain. *Science (1979)* (1996) 273:1709–1714. doi: 10.1126/SCIENCE.273.5282.1709
17. Núñez E, Muguruza-Montero A, Villarroel A. Atomistic Insights of Calmodulin Gating of Complete Ion Channels. *International Journal of Molecular Sciences 2020, Vol 21, Page 1285* (2020) 21:1285. doi: 10.3390/IJMS21041285
18. Orfali R, Nam YW, Nguyen HM, Rahman MA, Yang G, Cui M, Wulff H, Zhang M. Channelopathy-causing mutations in the S45A/S45B and HA/HB helices of KCa2.3

and KCa3.1 channels alter their apparent Ca2+ sensitivity. *Cell Calcium* (2022) 102: doi: 10.1016/j.ceca.2022.102538
19. Kovalenko I, Glasauer A, Schöckel L, Sauter DRP, Ehrmann A, Sohler F, Hägebarth A, Novak I, Christian S. Identification of KCa3.1 Channel as a Novel Regulator of Oxidative Phosphorylation in a Subset of Pancreatic Carcinoma Cell Lines. *PLoS One* (2016) 11: doi: 10.1371/JOURNAL.PONE.0160658
20. Lam J, Coleman N, Garing ALA, Wulff H. The Therapeutic Potential of Small-Conductance KCa2 Channels in Neurodegenerative and Psychiatric Diseases. *Expert Opin Ther Targets* (2013) 17:1203. doi: 10.1517/14728222.2013.823161
21. Maqoud F, Cetrone M, Mele A, Tricarico D. Molecular structure and function of big calcium-activated potassium channels in skeletal muscle: Pharmacological perspectives. *Physiol Genomics* (2017) 49:306–317. doi: 10.1152/PHYSIOLGENOMICS.00121.2016/ASSET/IMAGES/LARGE/ZH70051741800002.JPEG
22. Oh KH, Abraham LS, Gegg C, Silvestri C, Huang YC, Alkema MJ, Furst J, Raicu D, Kim H. Presynaptic BK channel localization is dependent on the hierarchical organization of alpha-catulin and dystrobrevin and fine-tuned by CaV2 calcium channels. *BMC Neurosci* (2015) 16:1–13. doi: 10.1186/S12868-015-0166-2/FIGURES/7
23. Schumacher MA, Rivard AF, Bächinger HP, Adelman JP. Structure of the gating domain of a Ca2+-activated K+ channel complexed with Ca2+/calmodulin. *Nature 2001 410:6832* (2001) 410:1120–1124. doi: 10.1038/35074145
24. Lee CH, MacKinnon R. Activation mechanism of a human SK-calmodulin channel complex elucidated by cryo-EM structures. *Science* (2018) 360:508. doi: 10.1126/SCIENCE.AAS9466
25. Morales P, Garneau L, Klein H, Lavoie MF, Parent L, Sauvé R. Contribution of the KCa3.1 channel-calmodulin interactions to the regulation of the KCa3.1 gating process. *J Gen Physiol* (2013) 142:37–60. doi: 10.1085/JGP.201210933
26. Shim H, Brown BM, Singh L, Singh V, Fettinger JC, Yarov-Yarovoy V, Wulff H. The Trials and Tribulations of Structure Assisted Design of KCa Channel Activators. *Front Pharmacol* (2019) 10: doi: 10.3389/FPHAR.2019.00972
27. Halling DB, Liebeskind BJ, Hall AW, Aldrich RW. Conserved properties of individual Ca2+-binding sites in calmodulin. *Proc Natl Acad Sci U S A* (2016) 113:E1216–E1225. doi: 10.1073/PNAS.1600385113/SUPPL_FILE/PNAS.1600385113.ST04.DOCX
28. Neely A, Hidalgo P. Structure-function of proteins interacting with the α1 pore-forming subunit of high-voltage-activated calcium channels. *Front Physiol* (2014) 5 JUN: doi: 10.3389/FPHYS.2014.00209
29. Yang CF, Tsai WC. Calmodulin: The switch button of calcium signaling. *Tzu-Chi Medical Journal* (2022) 34:15. doi: 10.4103/TCMJ.TCMJ_285_20
30. Castle NA, London DO, Creech C, Fajloun Z, Stocker JW, Sabatier JM. Maurotoxin: A Potent Inhibitor of Intermediate Conductance Ca2+-Activated Potassium Channels. *Mol Pharmacol* (2003) 63:409–418. doi: 10.1124/MOL.63.2.409
31. Jäger H, Grissmer S. Characterization of the outer pore region of the apamin-sensitive Ca2+-activated K+ channel rSK2. *Toxicon* (2004) 43:951–960. doi: 10.1016/j.toxicon.2004.03.025
32. Kuzmenkov AI, Peigneur S, Nasburg JA, Mineev KS, Nikolaev M V., Pinheiro-Junior EL, Arseniev AS, Wulff H, Tytgat J, Vassilevski AA. Apamin structure and pharmacology revisited. *Front Pharmacol* (2022) 13:3482. doi: 10.3389/FPHAR.2022.977440/BIBTEX
33. Nolting A, Ferraro T, D'Hoedt D, Stocker M. An amino acid outside the pore region influences apamin sensitivity in small conductance Ca2+-activated K+ channels. *J Biol Chem* (2007) 282:3478. doi: 10.1074/JBC.M607213200

34. Benton DCH, Garbarg M, Moss GWJ. The Relationship between Functional Inhibition and Binding for KCa2 Channel Blockers. *PLoS One* (2013) 8: doi: 10.1371/JOURNAL.PONE.0073328
35. Brown BM, Pressley B, Wulff H. KCa3.1 Channel Modulators as Potential Therapeutic Compounds for Glioblastoma. *Curr Neuropharmacol* (2018) 16:618. doi: 10.2174/1570159X15666170630164226
36. Stocker JW, De Franceschi L, McNaughton-Smith GA, Corrocher R, Beuzard Y, Brugnara C. ICA-17043, a novel Gardos channel blocker, prevents sickled red blood cell dehydration in vitro and in vivo in SAD mice. *Blood* (2003) 101:2412–2418. doi: 10.1182/BLOOD-2002-05-1433
37. Devor DC, Singh AK, Frizzell RA, Bridges RJ. Modulation of Cl- secretion by benzimidazolones. I. Direct activation of a Ca(2+)-dependent K+ channel. *Am J Physiol* (1996) 271: doi: 10.1152/AJPLUNG.1996.271.5.L775
38. Skaaning Jensen BO, Strøbæk D, Christophersen P, Jørgensen TD, Hansen C, Silahtaroglu A, Olesen SP, Ahring PK. Characterization of the cloned human intermediate-conductance Ca2+- activated K+ channel. *Am J Physiol Cell Physiol* (1998) 275: doi: 10.1152/AJPCELL.1998.275.3.C848/ASSET/IMAGES/LARGE/ACEL00906008X.JPEG
39. Pedarzani P, Mosbacher J, Rivard A, Cingolani LA, Oliver D, Stocker M, Adelman JP, Fakler B. Control of Electrical Activity in Central Neurons by Modulating the Gating of Small Conductance Ca2+-activated K+ Channels. *Journal of Biological Chemistry* (2001) 276:9762–9769. doi: 10.1074/JBC.M010001200
40. Hougaard C, Jensen ML, Dale TJ, Miller DD, Davies DJ, Eriksen BL, Strøbæk D, Trezise DJ, Christophersen P. Selective activation of the SK1 subtype of human small-conductance Ca 2+-activated K+ channels by 4-(2-methoxyphenylcarbamoyloxymethyl)-piperidine-1-carboxylic acid tert-butyl ester (GW542573X) is dependent on serine 293 in the S5 segment. *Mol Pharmacol* (2009) 76:569–578. doi: 10.1124/MOL.109.056663
41. Wittekindt OH, Visan V, Tomita H, Imtiaz F, Gargus JJ, Lehmann-Horn F, Grissmer S, Morris-Rosendahl DJ. An Apamin-and Scyllatoxin-Insensitive Isoform of the Human SK3 Channel. (2004) http://molpharm.aspetjournals.org [Accessed March 7, 2023]
42. Hougaard C, Eriksen BL, Jørgensen S, Johansen TH, Dyhring T, Madsen LS, Strøbæk D, Christophersen P. Selective positive modulation of the SK3 and SK2 subtypes of small conductance Ca2+-activated K+ channels. *Br J Pharmacol* (2007) 151:655. doi: 10.1038/SJ.BJP.0707281
43. Grunnet M, Jespersen T, Angelo K, Frøkjær-Jensen C, Klaerke DA, Olesen SP, Jensen BS. Pharmacological modulation of SK3 channels. *Neuropharmacology* (2001) 40:879–887. doi: 10.1016/S0028-3908(01)00028-4
44. Christophersen P, Wulff H. Pharmacological gating modulation of small- and intermediate-conductance Ca2+-activated K+ channels (KCa2.x and KCa3.1). *Channels* (2015) 9:336. doi: 10.1080/19336950.2015.1071748
45. Barrett KE, Keely SJ. Chloride Secretion by the Intestinal Epithelium: Molecular Basis and Regulatory Aspects. *Annu Rev Physiol* (2000) 62:535–572. doi: 10.1146/annurev.physiol.62.1.535
46. Pedarzani P, Stocker M. Molecular and cellular basis of small- and intermediate-conductance, calcium-activated potassium channel function in the brain. *Cellular and Molecular Life Sciences* (2008) 65:3196. doi: 10.1007/S00018-008-8216-X
47. Strøbæk D, Teuber L, Jørgensen TD, Ahring PK, Kjær K, Hansen RS, Olesen SP, Christophersen P, Skaaning-Jensen B. Activation of human IK and SK Ca2+-activated K+ channels by NS309 (6,7-dichloro-1H-indole-2,3-dione 3-oxime). *Biochimica et*

Biophysica Acta (BBA) - Biomembranes (2004) 1665:1–5. doi: 10.1016/J.BBAMEM.2004.07.006
48. Radtke J, Schmidt K, Wulff H, Köhler R, De Wit C. Activation of KCa3.1 by SKA-31 induces arteriolar dilatation and lowers blood pressure in normo- and hypertensive connexin40-deficient mice. *Br J Pharmacol* (2013) 170:293. doi: 10.1111/BPH.12267
49. Liu BS, Ferreira R, Lively S, Schlichter LC. Microglial SK3 and SK4 currents and activation state are modulated by the neuroprotective drug, riluzole. *Journal of Neuroimmune Pharmacology* (2013) 8:227–237. doi: 10.1007/S11481-012-9365-0/FIGURES/3
50. Sankaranarayanan A, Raman G, Busch C, Schultz T, Zimin PI, Hoyer J, Köhler R, Wulff H. Naphtho[1,2-d]thiazol-2-ylamine (SKA-31), a New Activator of KCa2 and KCa3.1 Potassium Channels, Potentiates the Endothelium-Derived Hyperpolarizing Factor Response and Lowers Blood Pressure. *Mol Pharmacol* (2009) 75:281. doi: 10.1124/MOL.108.051425
51. Jenkins DP, Yu W, Brown BM, Løjkner LD, Wulff H. Development of a QPatch Automated Electrophysiology Assay for Identifying KCa3.1 Inhibitors and Activators. *Assay Drug Dev Technol* (2013) 11:551. doi: 10.1089/ADT.2013.543
52. Wolfart J, Neuhoff H, Franz O, Roeper J. Differential Expression of the Small-Conductance, Calcium-Activated Potassium Channel SK3 Is Critical for Pacemaker Control in Dopaminergic Midbrain Neurons. *The Journal of Neuroscience* (2001) 21:3443. doi: 10.1523/JNEUROSCI.21-10-03443.2001
53. Zhang M, Pascal JM, Schumann M, Armen RS, Zhang JF. Identification of the functional binding pocket for compounds targeting small-conductance Ca2+-activated potassium channels. *Nat Commun* (2012) 3:1021. doi: 10.1038/NCOMMS2017
54. Zhang M, Pascal JM, Zhang JF. Unstructured to structured transition of an intrinsically disordered protein peptide in coupling Ca2+-sensing and SK channel activation. *Proc Natl Acad Sci U S A* (2013) 110:4828–4833. doi: 10.1073/PNAS.1220253110/-/DCSUPPLEMENTAL
55. Cho LTY, Alexandrou AJ, Torella R, Knafels J, Hobbs J, Taylor T, Loucif A, Konopacka A, Bell S, Stevens EB, et al. An Intracellular Allosteric Modulator Binding Pocket in SK2 Ion Channels Is Shared by Multiple Chemotypes. *Structure* (2018) 26:533-544.e3. doi: 10.1016/J.STR.2018.02.017
56. Cui M, Qin G, Yu K, Bowers MS, Zhang M. Targeting the Small- and Intermediate-Conductance Ca2+-Activated Potassium Channels: The Drug-Binding Pocket at the Channel/Calmodulin Interface. *Neurosignals* (2015) 22:65–78. doi: 10.1159/000367896
57. Burg S, Shapiro S, Peretz A, Haimov E, Redko B, Yeheskel A, Simhaev L, Engel H, Raveh A, Ben-Bassat A, et al. Allosteric inhibitors targeting the calmodulin-PIP2 interface of SK4 K+ channels for atrial fibrillation treatment. *Proc Natl Acad Sci U S A* (2022) 119:e2202926119. doi: 10.1073/PNAS.2202926119/SUPPL_FILE/PNAS.2202926119.SAPP.PDF
58. Brown BM, Shim H, Christophersen P, Wulff H. Pharmacology of Small-and Intermediate-Conductance Calcium-Activated Potassium Channels. *Annu Rev Pharmacol Toxicol* (2019) doi: 10.1146/annurev-pharmtox-010919
59. Nam YW, Cui M, El-Sayed NS, Orfali R, Nguyen M, Yang G, Rahman MA, Lee J, Zhang M. Subtype-selective positive modulation of KCa2 channels depends on the HA/HB helices. *Br J Pharmacol* (2022) 179:460–472. doi: 10.1111/bph.15676
60. Ferreira R, Schlichter LC. Selective Activation of KCa3.1 and CRAC Channels by P2Y2 Receptors Promotes Ca2+ Signaling, Store Refilling and Migration of Rat Microglial Cells. *PLoS One* (2013) 8: doi: 10.1371/journal.pone.0062345

61. Li W, Halling DB, Hall AW, Aldrich RW. EF hands at the N-lobe of calmodulin are required for both SK channel gating and stable SK-calmodulin interaction. *Journal of General Physiology* (2009) 134:281–293. doi: 10.1085/jgp.200910295
62. Bagur R, Hajnóczky G. Intracellular Ca2+ sensing: role in calcium homeostasis and signaling. *Mol Cell* (2017) 66:780. doi: 10.1016/J.MOLCEL.2017.05.028
63. Zhang M, Pascal JM, Zhang JF. Unstructured to structured transition of an intrinsically disordered protein peptide in coupling Ca2+-sensing and SK channel activation. *Proc Natl Acad Sci U S A* (2013) 110:4828–4833. doi: 10.1073/PNAS.1220253110/-/DCSUPPLEMENTAL
64. Zhang M, Meng XY, Zhang JF, Cui M, Logothetis DE. Molecular overlap in the regulation of SK channels by small molecules and phosphoinositides. *Sci Adv* (2015) 1: doi: 10.1126/SCIADV.1500008
65. Pedarzani P, Mosbacher J, Rivard A, Cingolani LA, Oliver D, Stocker M, Adelman JP, Fakler B. Control of Electrical Activity in Central Neurons by Modulating the Gating of Small Conductance Ca2+-activated K+ Channels. *Journal of Biological Chemistry* (2001) 276:9762–9769. doi: 10.1074/JBC.M010001200
66. Brown BM, Shim H, Zhang M, Yarov-Yarovoy V, Wulff H. Structural determinants for the selectivity of the positive KCa3.1 gating modulator 5-methylnaphtho[2,1-d]oxazol-2-amine (SKA-121). *Mol Pharmacol* (2017) 92:469–480. doi: 10.1124/MOL.117.109421/-/DC1
67. Orfali R, Nam YW, Nguyen HM, Rahman MA, Yang G, Cui M, Wulff H, Zhang M. Channelopathy-causing mutations in the S45A/S45B and HA/HB helices of KCa2.3 and KCa3.1 channels alter their apparent Ca2+ sensitivity. *Cell Calcium* (2022) 102:102538. doi: 10.1016/J.CECA.2022.102538
68. Nam Y-W, Pala R, Salem El-Sayed N, Larin-Henriquez D, Amirrad F, Yang G, Rahman MA, Orfali R, Downey M, Parang K, et al. Subtype-Selective Positive Modulation of K Ca 2.3 Channels Increases Cilia Length. *Cite This: ACS Chem Biol* (2344) 2022: doi: 10.1021/acschembio.2c00469
69. DeCoursey TE. Voltage-Gated Proton Channels. *Cell Mol Life Sci* (2008) 65:2554. doi: 10.1007/S00018-008-8056-8
70. Sasaki M, Takagi M, Okamura Y. A voltage sensor-domain protein is a voltage-gated proton channel. *Science* (2006) 312:589–592. doi: 10.1126/SCIENCE.1122352
71. Ramsey IS, Moran MM, Chong JA, Clapham DE. A voltage-gated proton-selective channel lacking the pore domain. *Nature 2006 440:7088* (2006) 440:1213–1216. doi: 10.1038/nature04700
72. Decoursey TE. The voltage-gated proton channel: a riddle, wrapped in a mystery, inside an enigma. *Biochemistry* (2015) 54:3250. doi: 10.1021/ACS.BIOCHEM.5B00353
73. DeCoursey TE. Voltage-gated Proton Channels. *Compr Physiol* (2012) 2:1355. doi: 10.1002/CPHY.C100071
74. DeCoursey TE. Voltage and pH sensing by the voltage-gated proton channel, HV1. *J R Soc Interface* (2018) 15: doi: 10.1098/RSIF.2018.0108
75. Schladt TM, Berger TK. Voltage and pH difference across the membrane control the S4 voltage-sensor motion of the Hv1 proton channel. *Scientific Reports 2020 10:1* (2020) 10:1–13. doi: 10.1038/s41598-020-77986-z
76. Mészáros B, Papp F, Mocsár G, Kókai E, Kovács K, Tajti G, Panyi G. The voltage-gated proton channel hHv1 is functionally expressed in human chorion-derived mesenchymal stem cells. *Sci Rep* (2020) 10: doi: 10.1038/S41598-020-63517-3
77. Carmona EM, Fernandez M, Alvear-Arias JJ, Neely A, Larsson HP, Alvarez O, Garate JA, Latorre R, Gonzalez C. The voltage sensor is responsible for ΔpH dependence in Hv1 channels. *Proc Natl Acad Sci U S A* (2021) 118:e2025556118. doi: 10.1073/PNAS.2025556118/SUPPL_FILE/PNAS.2025556118.SAPP.PDF

78. Coe D, Poobalasingam T, Fu H, Bonacina F, Wang G, Morales V, Moregola A, Mitro N, Cheung KCP, Ward EJ, et al. Loss of voltage-gated hydrogen channel 1 expression reveals heterogeneous metabolic adaptation to intracellular acidification by T cells. *JCI Insight* (2022) 7: doi: 10.1172/JCI.INSIGHT.147814
79. Capasso M, Bhamrah MK, Henley T, Boyd RS, Langlais C, Cain K, Dinsdale D, Pulford K, Khan M, Musset B, et al. HVCN1 modulates BCR signal strength via regulation of BCR-dependent generation of reactive oxygen species. *Nat Immunol* (2010) 11:265. doi: 10.1038/NI.1843
80. Okochi Y, Sasaki M, Iwasaki H, Okamura Y. Voltage-gated proton channel is expressed on phagosomes. *Biochem Biophys Res Commun* (2009) 382:274–279. doi: 10.1016/J.BBRC.2009.03.036
81. Petheo GL, Orient A, Baráth M, Kovács I, Réthi B, Lányi Á, Rajki A, Rajnavölgyi É, Geiszt M. Molecular and Functional Characterization of Hv1 Proton Channel in Human Granulocytes. *PLoS One* (2010) 5: doi: 10.1371/JOURNAL.PONE.0014081
82. Montes-Cobos E, Huscher B, Engler JB, Woo MS, Binkle L, Bauer S, Kursawe N, Moles M, Friese MA, Ufer F. Voltage-Gated Proton Channel Hv1 Controls TLR9 Activation in Plasmacytoid Dendritic Cells. *J Immunol* (2020) 205:3001–3010. doi: 10.4049/JIMMUNOL.2000404
83. Wu LJ. Voltage-gated proton channel HV1 in microglia. *Neuroscientist* (2014) 20:599–609. doi: 10.1177/1073858413519864
84. Zhao R, Kennedy K, De Blas GA, Orta G, Pavarotti MA, Arias RJ, de la Vega-Beltrán JL, Li Q, Dai H, Perozo E, et al. Role of human Hv1 channels in sperm capacitation and white blood cell respiratory burst established by a designed peptide inhibitor. *Proc Natl Acad Sci U S A* (2018) 115:E11847–E11856. doi: 10.1073/PNAS.1816189115/SUPPL_FILE/PNAS.1816189115.SAPP.PDF
85. Ramsey IS, Ruchti E, Kaczmarek JS, Clapham DE. Hv1 proton channels are required for high-level NADPH oxidase-dependent superoxide production during the phagocyte respiratory burst. *Proc Natl Acad Sci U S A* (2009) 106:7642–7647. doi: 10.1073/PNAS.0902761106
86. Panday A, Sahoo MK, Osorio D, Batra S. NADPH oxidases: an overview from structure to innate immunity-associated pathologies. *Cell Mol Immunol* (2015) 12:5. doi: 10.1038/CMI.2014.89
87. Delgado-Bermúdez A, Yeste M, Bonet S, Pinart E. A Review on the Role of Bicarbonate and Proton Transporters during Sperm Capacitation in Mammals. *Int J Mol Sci* (2022) 23: doi: 10.3390/ijms23116333
88. Morgan D, Capasso M, Musset B, Cherny V V., Ríos E, Dyer MJS, DeCoursey TE. Voltage-gated proton channels maintain pH in human neutrophils during phagocytosis. *Proc Natl Acad Sci U S A* (2009) 106:18022. doi: 10.1073/PNAS.0905565106
89. Ugel S, De Sanctis F, Mandruzzato S, Bronte V. Tumor-induced myeloid deviation: when myeloid-derived suppressor cells meet tumor-associated macrophages. *J Clin Invest* (2015) 125:3365. doi: 10.1172/JCI80006
90. Kusmartsev S, Gabrilovich DI. Role Of Immature Myeloid Cells in Mechanisms of Immune Evasion In Cancer. *Cancer Immunol Immunother* (2006) 55:237. doi: 10.1007/S00262-005-0048-Z
91. Kusmartsev S, Nefedova Y, Yoder D, Gabrilovich DI. Antigen-Specific Inhibition of CD8+ T Cell Response by Immature Myeloid Cells in Cancer Is Mediated by Reactive Oxygen Species. *The Journal of Immunology* (2004) 172:989–999. doi: 10.4049/JIMMUNOL.172.2.989
92. Nagaraj S, Gupta K, Pisarev V, Kinarsky L, Sherman S, Kang L, Herber DL, Schneck J, Gabrilovich DI. Altered recognition of antigen is a novel mechanism of CD8+ T cell tolerance in cancer. *Nat Med* (2007) 13:828. doi: 10.1038/NM1609

93. Qiu F, Chamberlin A, Watkins BM, Ionescu A, Perez ME, Barro-Soria R, González C, Noskov SY, Larsson HP. Molecular mechanism of Zn2+ inhibition of a voltage-gated proton channel. *Proc Natl Acad Sci U S A* (2016) 113:E5962–E5971. doi: 10.1073/PNAS.1604082113/-/DCSUPPLEMENTAL
94. Tombola F, Ulbrich MH, Isacoff EY. The voltage-gated proton channel Hv1 has two pores each controlled by one voltage sensor. *Neuron* (2008) 58:546. doi: 10.1016/J.NEURON.2008.03.026
95. Hong L, Pathak MM, Kim IH, Ta D, Tombola F. Voltage-sensing domain of voltage-gated proton channel Hv1 shares mechanism of block with pore domains. *Neuron* (2013) 77:274. doi: 10.1016/J.NEURON.2012.11.013
96. Szanto TG, Feher A, Korpos E, Gyöngyösi A, Kállai J, Mészáros B, Ovari K, Lányi Á, Panyi G, Varga Z. 5-Chloro-2-Guanidinobenzimidazole (ClGBI) Is a Non-Selective Inhibitor of the Human HV1 Channel. *Pharmaceuticals 2023, Vol 16, Page 656* (2023) 16:656. doi: 10.3390/PH16050656
97. Hong L, Kim IH, Tombola F. Molecular determinants of Hv1 proton channel inhibition by guanidine derivatives. *Proc Natl Acad Sci U S A* (2014) 111:9971–9976. doi: 10.1073/PNAS.1324012111/-/DCSUPPLEMENTAL
98. Zhao R, Kennedy K, De Blas GA, Orta G, Pavarotti MA, Arias RJ, de la Vega-Beltrán JL, Li Q, Dai H, Perozo E, et al. Role of human Hv1 channels in sperm capacitation and white blood cell respiratory burst established by a designed peptide inhibitor. *Proc Natl Acad Sci U S A* (2018) 115:E11847–E11856. doi: 10.1073/PNAS.1816189115/-/DCSUPPLEMENTAL
99. El Chemaly A, Jaquet V, Cambet Y, Caillon A, Cherpin O, Balafa A, Krause KH, Demaurex N. Discovery and validation of new Hv1 proton channel inhibitors with onco-therapeutic potential. *Biochimica et Biophysica Acta (BBA) - Molecular Cell Research* (2023) 1870:119415. doi: 10.1016/J.BBAMCR.2022.119415
100. Zhao C, Hong L, Riahi S, Lim VT, Tobias DJ, Tombola F. A novel Hv1 inhibitor reveals a new mechanism of inhibition of a voltage-sensing domain. *J Gen Physiol* (2021) 153: doi: 10.1085/JGP.202012833
101. Alvear-Arias JJ, Carrillo C, Villar JP, Garcia-Betancourt R, Pena-Pichicoi A, Fernandez A, Fernandez M, Carmona EM, Pupo A, Neely A, et al. Expression of Hv1 proton channels in myeloid-derived suppressor cells (MDSC) and its potential role in T cell regulation. *Proc Natl Acad Sci U S A* (2022) 119: doi: 10.1073/PNAS.2104453119
102. Rangel-Yescas G, Cervantes C, Cervantes-Rocha MA, Suárez-Delgado E, Banaszak AT, Maldonado E, Ramsey IS, Rosenbaum T, Islas LD. Discovery and characterization of Hv1-type proton channels in reef-building corals. *Elife* (2021) 10: doi: 10.7554/ELIFE.69248
103. Asuaje A, Smaldini P, Martín P, Enrique N, Orlowski A, Aiello EA, Gonzalez León C, Docena G, Milesi V. The inhibition of voltage-gated H+ channel (HVCN1) induces acidification of leukemic Jurkat T cells promoting cell death by apoptosis. *Pflugers Arch* (2017) 469:251–261. doi: 10.1007/S00424-016-1928-0
104. Gattas MV, Jaffe A, Barahona J, Conner GE. Proton channel blockers inhibit Duox activity independent of Hv1 effects. *Redox Biol* (2020) 28: doi: 10.1016/J.REDOX.2019.101346
105. Pierce G. Should we clean up the reputation of "dirty drugs"? *Can J Physiol Pharmacol* (2012) 90:1333–1334. doi: 10.1139/Y2012-110
106. Abbas AK, Lichtman AH, Pillai S. *Cellular and Molecular Immunology - 10th Edition*. Saunders/Elsevier. (2021). 600 p. https://www.elsevier.com/books/cellular-and-molecular-immunology/abbas/978-0-323-75748-5 [Accessed May 9, 2023]
107. Feske S. Calcium signalling in lymphocyte activation and disease. *Nature Reviews Immunology 2007 7:9* (2007) 7:690–702. doi: 10.1038/nri2152

108. Cahalan MD, Chandy KG. The functional network of ion channels in T lymphocytes. *Immunol Rev* (2009) 231:59. doi: 10.1111/J.1600-065X.2009.00816.X
109. Chimote AA, Hajdu P, Kottyan LC, Harley JB, Yun Y, Conforti L. Nanovesicle-targeted Kv1.3 knockdown in memory T cells suppresses CD40L expression and memory phenotype. *J Autoimmun* (2016) 69:86. doi: 10.1016/J.JAUT.2016.03.004
110. Di L, Srivastava S, Zhdanova O, Ding Y, Li Z, Wulff H, Lafaille M, Skolnik EY. Inhibition of the K+ channel KCa3.1 ameliorates T cell-mediated colitis. *Proc Natl Acad Sci U S A* (2010) 107:1541–1546. doi: 10.1073/PNAS.0910133107/SUPPL_FILE/PNAS.200910133SI.PDF
111. Naseem MU, Tajti G, Gaspar A, Szanto TG, Borrego J, Panyi G. Optimization of Pichia pastoris Expression System for High-Level Production of Margatoxin. *Front Pharmacol* (2021) 12:2454. doi: 10.3389/FPHAR.2021.733610/BIBTEX
112. Ghanshani S, Wulff H, Miller MJ, Rohm H, Neben A, Gutman GA, Cahalan MD, Chandy KG. Up-regulation of the IKCa1 Potassium Channel during T-cell Activation: MOLECULAR MECHANISM AND FUNCTIONAL CONSEQUENCES. *Journal of Biological Chemistry* (2000) 275:37137–37149. doi: 10.1074/JBC.M003941200
113. Chimote AA, Gawali VS, Newton HS, Wise-Draper TM, Conforti L. A Compartmentalized Reduction in Membrane-Proximal Calmodulin Reduces the Immune Surveillance Capabilities of CD8+ T Cells in Head and Neck Cancer. *Front Pharmacol* (2020) 11: doi: 10.3389/FPHAR.2020.00143/FULL
114. Cañas CA, Castaño-Valencia S, Castro-Herrera F. Pharmacological blockade of KV1.3 channel as a promising treatment in autoimmune diseases. *J Transl Autoimmun* (2022) 5: doi: 10.1016/j.jtauto.2022.100146
115. Wang X, Li G, Guo J, Zhang Z, Zhang S, Zhu Y, Cheng J, Yu L, Ji Y, Tao J. Kv1.3 Channel as a Key Therapeutic Target for Neuroinflammatory Diseases: State of the Art and Beyond. *Front Neurosci* (2020) 13: doi: 10.3389/fnins.2019.01393
116. Greten FR, Grivennikov SI. Inflammation and Cancer: Triggers, Mechanisms and Consequences. *Immunity* (2019) 51:27. doi: 10.1016/J.IMMUNI.2019.06.025
117. Gonzalez H, Hagerling C, Werb Z. Roles of the immune system in cancer: from tumor initiation to metastatic progression. *Genes Dev* (2018) 32:1267. doi: 10.1101/GAD.314617.118
118. Yuen GJ, Demissie E, Pillai S. B Lymphocytes and Cancer: A Love–Hate Relationship. *Trends Cancer* (2016) 2:747–757. doi: 10.1016/j.trecan.2016.10.010
119. Paijens ST, Vledder A, de Bruyn M, Nijman HW. Tumor-infiltrating lymphocytes in the immunotherapy era. *Cellular & Molecular Immunology 2020 18:4* (2020) 18:842–859. doi: 10.1038/s41423-020-00565-9
120. Barry ST, Gabrilovich DI, Sansom OJ, Campbell AD, Morton JP. Therapeutic targeting of tumour myeloid cells. *Nature Reviews Cancer 2023 23:4* (2023) 23:216–237. doi: 10.1038/s41568-022-00546-2
121. Ugel S, De Sanctis F, Mandruzzato S, Bronte V. Tumor-induced myeloid deviation: when myeloid-derived suppressor cells meet tumor-associated macrophages. *J Clin Invest* (2015) 125:3365. doi: 10.1172/JCI80006
122. Nagaraj S, Gupta K, Pisarev V, Kinarsky L, Sherman S, Kang L, Herber DL, Schneck J, Gabrilovich DI. Altered recognition of antigen is a novel mechanism of CD8+ T cell tolerance in cancer. *Nat Med* (2007) 13:828. doi: 10.1038/NM1609
123. Baumann T, Dunkel A, Schmid C, Schmitt S, Hiltensperger M, Lohr K, Laketa V, Donakonda S, Ahting U, Lorenz-Depiereux B, et al. Regulatory myeloid cells paralyze T cells through cell–cell transfer of the metabolite methylglyoxal. *Nature Immunology 2020 21:5* (2020) 21:555–566. doi: 10.1038/s41590-020-0666-9
124. Grzywa TM, Sosnowska A, Matryba P, Rydzynska Z, Jasinski M, Nowis D, Golab J. Myeloid Cell-Derived Arginase in Cancer Immune Response. *Front Immunol* (2020) 11:536322. doi: 10.3389/FIMMU.2020.00938/BIBTEX

125. Geiger R, Rieckmann JC, Wolf T, Basso C, Feng Y, Fuhrer T, Kogadeeva M, Picotti P, Meissner F, Mann M, et al. L-Arginine Modulates T Cell Metabolism and Enhances Survival and Anti-tumor Activity. *Cell* (2016) 167:829. doi: 10.1016/J.CELL.2016.09.031
126. Su LJ, Zhang JH, Gomez H, Murugan R, Hong X, Xu D, Jiang F, Peng ZY. Reactive Oxygen Species-Induced Lipid Peroxidation in Apoptosis, Autophagy, and Ferroptosis. *Oxid Med Cell Longev* (2019) 2019: doi: 10.1155/2019/5080843
127. Ugolini A, Tyurin VA, Tyurina YY, Tcyganov EN, Donthireddy L, Kagan VE, Gabrilovich DI, Veglia F. Polymorphonuclear myeloid-derived suppressor cells limit antigen cross-presentation by dendritic cells in cancer. *JCI Insight* (2020) 5: doi: 10.1172/JCI.INSIGHT.138581
128. Jin J, Lin J, Xu A, Lou J, Qian C, Li X, Wang Y, Yu W, Tao H. CCL2: An Important Mediator Between Tumor Cells and Host Cells in Tumor Microenvironment. *Front Oncol* (2021) 11:722916. doi: 10.3389/FONC.2021.722916/BIBTEX
129. Bianchi G, Vuerich M, Pellegatti P, Marimpietri D, Emionite L, Marigo I, Bronte V, Di Virgilio F, Pistoia V, Raffaghello L. ATP/P2X7 axis modulates myeloid-derived suppressor cell functions in neuroblastoma microenvironment. *Cell Death Dis* (2014) 5:e1135. doi: 10.1038/CDDIS.2014.109
130. Hegde VL, Nagarkatti PS, Nagarkatti M. Role of Myeloid-Derived Suppressor Cells in Amelioration of Experimental Autoimmune Hepatitis Following Activation of TRPV1 Receptors by Cannabidiol. *PLoS One* (2011) 6: doi: 10.1371/JOURNAL.PONE.0018281
131. Burgos-Panadero R, Lucantoni F, Gamero-Sandemetrio E, Cruz-Merino L de la, Álvaro T, Noguera R. The tumour microenvironment as an integrated framework to understand cancer biology. *Cancer Lett* (2019) 461:112–122. doi: 10.1016/J.CANLET.2019.07.010
132. Lee SY, Ju MK, Jeon HM, Jeong EK, Lee YJ, Kim CH, Park HG, Han SI, Kang HS. Regulation of Tumor Progression by Programmed Necrosis. *Oxid Med Cell Longev* (2018) 2018: doi: 10.1155/2018/3537471
133. Eil R, Vodnala SK, Clever D, Klebanoff CA, Sukumar M, Pan JH, Palmer DC, Gros A, Yamamoto TN, Patel SJ, et al. Ionic immune suppression within the tumour microenvironment limits T cell effector function. *Nature 2016 537:7621* (2016) 537:539–543. doi: 10.1038/nature19364
134. Ong ST, Ng AS, Ng XR, Zhuang Z, Wong BHS, Prasannan P, Kok YJ, Bi X, Shim H, Wulff H, et al. Extracellular K+ Dampens T Cell Functions: Implications for Immune Suppression in the Tumor Microenvironment. *Bioelectricity* (2019) 1:169. doi: 10.1089/BIOE.2019.0016
135. Eil R, Vodnala SK, Clever D, Klebanoff CA, Sukumar M, Pan JH, Palmer DC, Gros A, Yamamoto TN, Patel SJ, et al. Ionic immune suppression within the tumour microenvironment limits T cell effector function. *Nature 2016 537:7621* (2016) 537:539–543. doi: 10.1038/nature19364
136. Vodnala SK, Eil R, Kishton RJ, Sukumar M, Yamamoto TN, Ha NH, Lee PH, Shin MH, Patel SJ, Yu Z, et al. T cell stemness and dysfunction in tumors are triggered by a common mechanism. *Science* (2019) 363: doi: 10.1126/SCIENCE.AAU0135
137. Ong ST, Ng AS, Ng XR, Zhuang Z, Wong BHS, Prasannan P, Kok YJ, Bi X, Shim H, Wulff H, et al. Extracellular K + Dampens T Cell Functions: Implications for Immune Suppression in the Tumor Microenvironment . *Bioelectricity* (2019) 1:169–179. doi: 10.1089/bioe.2019.0016
138. Chandy KG, Norton RS. Channelling potassium to fight cancer. *Nature 2016 537:7621* (2016) 537:497–499. doi: 10.1038/nature19467
139. Greiner J V., Glonek T. Intracellular atp concentration and implication for cellular evolution. *Biology (Basel)* (2021) 10: doi: 10.3390/BIOLOGY10111166/S1

140. Trautmann A. Extracellular ATP in the immune system: more than just a “danger signal”. *Sci Signal* (2009) 2:pe6–pe6. doi: 10.1126/SCISIGNAL.256PE6
141. Hu LP, Zhang XX, Jiang SH, Tao LY, Li Q, Zhu LL, Yang MW, Huo YM, Jiang YS, Tian GA, et al. Targeting Purinergic Receptor P2Y2 Prevents the Growth of Pancreatic Ductal Adenocarcinoma by Inhibiting Cancer Cell Glycolysis. *Clin Cancer Res* (2019) 25:1318–1330. doi: 10.1158/1078-0432.CCR-18-2297
142. Pellegatti P, Raffaghello L, Bianchi G, Piccardi F, Pistoia V, Di Virgilio F. Increased Level of Extracellular ATP at Tumor Sites: In Vivo Imaging with Plasma Membrane Luciferase. *PLoS One* (2008) 3:e2599. doi: 10.1371/JOURNAL.PONE.0002599
143. Künzli BM, Berberat PO, Giese T, Csizmadia E, Kaczmarek E, Baker C, Halaceli I, Büchler MW, Friess H, Robson SC. Upregulation of CD39/NTPDases and P2 receptors in human pancreatic disease. *Am J Physiol Gastrointest Liver Physiol* (2007) 292: doi: 10.1152/AJPGI.00259.2006
144. Harvey JB, Phan LH, Villarreal OE, Bowser JL. CD73’s Potential as an Immunotherapy Target in Gastrointestinal Cancers. *Front Immunol* (2020) 11: doi: 10.3389/FIMMU.2020.00508
145. Gao ZW, Dong K, Zhang HZ. The Roles of CD73 in Cancer. *Biomed Res Int* (2014) 2014: doi: 10.1155/2014/460654
146. Guo S, Han F, Zhu W. CD39 – A bright target for cancer immunotherapy. *Biomedicine & Pharmacotherapy* (2022) 151:113066. doi: 10.1016/J.BIOPHA.2022.113066
147. Löfgren L, Pehrsson S, Hägglund G, Tjellström H, Nylander S. Accurate measurement of endogenous adenosine in human blood. *PLoS One* (2018) 13: doi: 10.1371/JOURNAL.PONE.0205707
148. Blay J. Adenosine and Tumor Microenvironment. *Encyclopedia of Cancer* (2011)49–52. doi: 10.1007/978-3-642-16483-5_89
149. Cekic C, Linden J. Adenosine A2A receptors intrinsically regulate CD8+ T cells in the tumor microenvironment. *Cancer Res* (2014) 74:7239. doi: 10.1158/0008-5472.CAN-13-3581
150. Chimote AA, Hajdu P, Sfyris AM, Gleich BN, Wise-Draper T, Casper KA, Conforti L. Kv1.3 channels mark functionally competent CD8+ tumor infiltrating lymphocytes in head and neck cancer. *Cancer Res* (2017) 77:53. doi: 10.1158/0008-5472.CAN-16-2372
151. Chimote AA, Balajthy A, Arnold MJ, Newton HS, Hajdu P, Qualtieri J, Wise-Draper T, Conforti L. A defect in KCa3.1 channel activity limits the ability of CD8+ T cells from cancer patients to infiltrate an adenosine-rich microenvironment. *Sci Signal* (2018) 11: doi: 10.1126/SCISIGNAL.AAQ1616
152. Chimote AA, Hajdu P, Kucher V, Boiko N, Kuras Z, Szilagyi O, Yun Y-H, Conforti L. Selective inhibition of KCa3.1 channels mediates adenosine regulation of the motility of human T cells. *J Immunol* (2013) 191:6273. doi: 10.4049/JIMMUNOL.1300702
153. Song CW, Park H, Ross BD. Intra- and Extracellular pH in Solid Tumors. *Antiangiogenic Agents in Cancer Therapy* (1999)51–64. doi: 10.1007/978-1-59259-453-5_4
154. Vaupel P, Multhoff G, Bennet L, Chan J, Vaupel P, Multhoff G, Physiol J. Revisiting the Warburg effect: historical dogma versus current understanding. *J Physiol* (2021) 599:1745–1757. doi: 10.1113/JP278810
155. Chen M, Chen C, Shen Z, Zhang X, Chen Y, Lin F, Ma X, Zhuang C, Mao Y, Gan H, et al. Extracellular pH is a biomarker enabling detection of breast cancer and liver cancer using CEST MRI. *Oncotarget* (2017) 8:45759–45767. doi: 10.18632/ONCOTARGET.17404
156. Thistlethwaite AJ, Leeper DB, Moylan DJ, Nerlinger RE. pH distribution in human tumors. *International Journal of Radiation Oncology*Biology*Physics* (1985) 11:1647–1652. doi: 10.1016/0360-3016(85)90217-2

157. Zachariah TP, Balaraman V, Crew RJ. Cardiorenal Syndrome Type 3. *Critical Care Nephrology: Third Edition* (2019)695-701.e2. doi: 10.1016/B978-0-323-44942-7.00113-8
158. White KA, Grillo-Hill BK, Barber DL. Cancer cell behaviors mediated by dysregulated pH dynamics at a glance. *J Cell Sci* (2017) 130:663–669. doi: 10.1242/JCS.195297
159. Pérez-Herrero E, Fernández-Medarde A. The reversed intra- and extracellular pH in tumors as a unified strategy to chemotherapeutic delivery using targeted nanocarriers. *Acta Pharm Sin B* (2021) 11:2243–2264. doi: 10.1016/J.APSB.2021.01.012
160. Goldenberg JM, Cárdenas-Rodríguez J, Pagel MD. Preliminary Results that Assess Metformin Treatment in a Preclinical Model of Pancreatic Cancer Using Simultaneous [18F]FDG PET and acidoCEST MRI. *Molecular imaging and biology : MIB : the official publication of the Academy of Molecular Imaging* (2018) 20:575. doi: 10.1007/S11307-018-1164-4
161. Huber V, Camisaschi C, Berzi A, Ferro S, Lugini L, Triulzi T, Tuccitto A, Tagliabue E, Castelli C, Rivoltini L. Cancer acidity: An ultimate frontier of tumor immune escape and a novel target of immunomodulation. *Semin Cancer Biol* (2017) 43:74–89. doi: 10.1016/J.SEMCANCER.2017.03.001
162. Bosticardo M, Ariotti S, Losana G, Bernabei P, Forni G, Novelli F. Biased activation of human T lymphocytes due to low extracellular pH is antagonized by B7/CD28 costimulation. *Eur J Immunol* (2001) 31:2829–2838. doi: 10.1002/1521-4141(200109)31:9<2829::AID-IMMU2829>3.0.CO;2-U
163. Calcinotto A, Filipazzi P, Grioni M, Iero M, De Milito A, Ricupito A, Cova A, Canese R, Jachetti E, Rossetti M, et al. Modulation of microenvironment acidity reverses anergy in human and murine tumor-infiltrating T lymphocytes. *Cancer Res* (2012) 72:2746–2756. doi: 10.1158/0008-5472.CAN-11-1272/657110/P/MODULATION-OF-MICROENVIRONMENT-ACIDITY-REVERSES
164. Fischer K, Hoffmann P, Voelkl S, Meidenbauer N, Ammer J, Edinger M, Gottfried E, Schwarz S, Rothe G, Hoves S, et al. Inhibitory effect of tumor cell–derived lactic acid on human T cells. *Blood* (2007) 109:3812–3819. doi: 10.1182/BLOOD-2006-07-035972
165. Audero MM, Carvalho TMA, Ruffinatti FA, Loeck T, Yassine M, Chinigò G, Folcher A, Farfariello V, Amadori S, Vaghi C, et al. Acidic Growth Conditions Promote Epithelial-to-Mesenchymal Transition to Select More Aggressive PDAC Cell Phenotypes In Vitro. *Cancers (Basel)* (2023) 15:2572. doi: 10.3390/CANCERS15092572
166. Stock C, Gassner B, Hauck CR, Arnold H, Mally S, Eble JA, Dieterich P, Schwab A. Migration of human melanoma cells depends on extracellular pH and Na+/H+ exchange. *J Physiol* (2005) 567:225. doi: 10.1113/JPHYSIOL.2005.088344
167. Rofstad EK, Mathiesen B, Kindem K, Galappathi K. Acidic extracellular pH promotes experimental metastasis of human melanoma cells in athymic nude mice. *Cancer Res* (2006) 66:6699–6707. doi: 10.1158/0008-5472.CAN-06-0983
168. Kato Y, Lambert CA, Colige AC, Mineur P, Noël A, Frankenne F, Foidart JM, Baba M, Hata RI, Miyazaki K, et al. Acidic extracellular pH induces matrix metalloproteinase-9 expression in mouse metastatic melanoma cells through the phospholipase D-mitogen-activated protein kinase signaling. *J Biol Chem* (2005) 280:10938–10944. doi: 10.1074/JBC.M411313200
169. Yang L, DeBusk LM, Fukuda K, Fingleton B, Green-Jarvis B, Shyr Y, Matrisian LM, Carbone DP, Lin PC. Expansion of myeloid immune suppressor Gr+CD11b+ cells in tumor-bearing host directly promotes tumor angiogenesis. *Cancer Cell* (2004) 6:409–421. doi: 10.1016/J.CCR.2004.08.031
170. Wang Y, Li SJ, Pan J, Che Y, Yin J, Zhao Q. Specific expression of the human voltage-gated proton channel Hv1 in highly metastatic breast cancer cells, promotes

tumor progression and metastasis. *Biochem Biophys Res Commun* (2011) 412:353–359. doi: 10.1016/J.BBRC.2011.07.102
171. Ranade SS, Syeda R, Patapoutian A. Mechanically Activated Ion Channels. *Neuron* (2015) 87:1162. doi: 10.1016/J.NEURON.2015.08.032
172. Lamas JA, Rueda-Ruzafa L, Herrera-Pérez S. Ion Channels and Thermosensitivity: TRP, TREK, or Both? *Int J Mol Sci* (2019) 20: doi: 10.3390/IJMS20102371
173. Holzer P. Acid-sensitive ion channels and receptors. *Handb Exp Pharmacol* (2009) 194:283–332. doi: 10.1007/978-3-540-79090-7_9
174. Yang F, Zheng J. High temperature sensitivity is intrinsic to voltage-gated potassium channels. *Elife* (2014) 3:e03255. doi: 10.7554/ELIFE.03255
175. Pahapill PA, Schlichter LC. Modulation of potassium channels in human T lymphocytes: effects of temperature. *J Physiol* (1990) 422:103. doi: 10.1113/JPHYSIOL.1990.SP017975
176. Deutsch C, Lee SC. Modulation of K+ currents in human lymphocytes by pH. *J Physiol* (1989) 413:399–413. doi: 10.1113/JPHYSIOL.1989.SP017660
177. Voros O, Szilagyi O, Balajthy A, Somodi S, Panyi G, Hajdu P. The C-terminal HRET sequence of Kv1.3 regulates gating rather than targeting of Kv1.3 to the plasma membrane. *Sci Rep* (2018) 8: doi: 10.1038/s41598-018-24159-8
178. Evdokimov AG, Pokross ME, Egorov NS, Zaraisky AG, Yampolsky I V., Merzlyak EM, Shkoporov AN, Sander I, Lukyanov KA, Chudakov DM. Structural basis for the fast maturation of Arthropoda green fluorescent protein. *EMBO Rep* (2006) 7:1006–1012. doi: 10.1038/sj.embor.7400787
179. Cozzolino M, Gyöngyösi A, Korpos E, Gogolak P, Naseem MU, Kállai J, Lanyi A, Panyi G. The Voltage-Gated Hv1 H+ Channel Is Expressed in Tumor-Infiltrating Myeloid-Derived Suppressor Cells. *Int J Mol Sci* (2023) 24: doi: 10.3390/ijms24076216
180. Bers DM, Patton CW, Nuccitelli R. "A Practical Guide to the Preparation of Ca2+ Buffers.," *Methods in Cell Biology*. (2010). p. 1–26 doi: 10.1016/S0091-679X(10)99001-8
181. Jenkins DP, Yu W, Brown BM, Løjkner LD, Wulff H. Development of a QPatch automated electrophysiology assay for identifying KCa3.1 inhibitors and activators. *Assay Drug Dev Technol* (2013) 11:551–560. doi: 10.1089/adt.2013.543
182. Rashid MH, Borin TF, Ara R, Piranlioglu R, Achyut BR, Korkaya H, Liu Y, Arbab AS. Critical immunosuppressive effect of MDSC-derived exosomes in the tumor microenvironment. *Oncol Rep* (2021) 45:1171–1181. doi: 10.3892/or.2021.7936
183. Giannotta C, Autino F, Massaia M. The immune suppressive tumor microenvironment in multiple myeloma: The contribution of myeloid-derived suppressor cells. *Front Immunol* (2023) 13: doi: 10.3389/fimmu.2022.1102471
184. Husain Z, Huang Y, Seth P, Sukhatme VP. Tumor-Derived Lactate Modifies Antitumor Immune Response: Effect on Myeloid-Derived Suppressor Cells and NK Cells. *The Journal of Immunology* (2013) 191:1486–1495. doi: 10.4049/jimmunol.1202702
185. Sun C, Nagaoka K, Kobayashi Y, Nakagawa H, Kakimi K, Nakajima J. Neoantigen dendritic cell vaccination combined with anti-cd38 and cpg elicits anti-tumor immunity against the immune checkpoint therapy-resistant murine lung cancer cell line llc1. *Cancers (Basel)* (2021) 13: doi: 10.3390/cancers13215508
186. Bronte V, Brandau S, Chen SH, Colombo MP, Frey AB, Greten TF, Mandruzzato S, Murray PJ, Ochoa A, Ostrand-Rosenberg S, et al. Recommendations for myeloid-derived suppressor cell nomenclature and characterization standards. *Nat Commun* (2016) 7: doi: 10.1038/ncomms12150
187. Haverkamp JM, Smith AM, Weinlich R, Dillon CP, Qualls JE, Neale G, Koss B, Kim Y, Bronte V, Herold MJ, et al. Myeloid-derived suppressor activity is mediated by

monocytic lineages maintained by continuous inhibition of extrinsic and intrinsic death pathways. *Immunity* (2014) 41:947–959. doi: 10.1016/j.immuni.2014.10.020
188. Petheo GL, Orient A, Baráth M, Kovács I, Réthi B, Lányi Á, Rajki A, Rajnavölgyi É, Geiszt M. Molecular and functional characterization of Hv1 proton channel in human granulocytes. *PLoS One* (2010) 5: doi: 10.1371/journal.pone.0014081
189. Okochi Y, Okamura Y. Regulation of Neutrophil Functions by Hv1/VSOP Voltage-Gated Proton Channels. *Int J Mol Sci* (2021) 22:2620. doi: 10.3390/ijms22052620
190. Alvear-Arias JJ, Carrillo C, Villar JP, Garcia-Betancourt R, Peña-Pichicoi A, Fernandez A, Fernandez M, Carmona EM, Pupo A, Neely A, et al. Expression of Hv 1 proton channels in myeloid-derived suppressor cells (MDSC) and its potential role in T cell regulation. *Proceedings of the National Academy of Sciences* (2022) 119: doi: 10.1073/pnas.2104453119
191. Sokolov VS, Cherny V V., Ayuyan AG, DeCoursey TE. Analysis of an electrostatic mechanism for ΔpH dependent gating of the voltage-gated proton channel, HV1, supports a contribution of protons to gating charge. *Biochimica et Biophysica Acta (BBA) - Bioenergetics* (2021) 1862:148480. doi: 10.1016/j.bbabio.2021.148480
192. Ghanshani S, Wulff H, Miller MJ, Rohm H, Neben A, Gutman GA, Cahalan MD, Chandy KG. Up-regulation of the IKCa1 potassium channel during T-cell activation: Molecular mechanism and functional consequences. *Journal of Biological Chemistry* (2000) 275:37137–37149. doi: 10.1074/jbc.M003941200
193. Varga Z, Tajti G, Panyi G. The Kv1.3 K+ channel in the immune system and its "precision pharmacology" using peptide toxins. *Biol Futur* (2021) 72:75–83. doi: 10.1007/s42977-021-00071-7
194. Navarro-Pérez M, Estadella I, Benavente-Garcia A, Orellana-Fernández R, Petit A, Ferreres JC, Felipe A. The Phosphorylation of Kv1.3: A Modulatory Mechanism for a Multifunctional Ion Channel. *Cancers (Basel)* (2023) 15: doi: 10.3390/cancers15102716
195. Hou P, Zhang R, Liu Y, Feng J, Wang W, Wu Y, Ding J. Physiological role of Kv1.3 channel in T lymphocyte cell investigated quantitatively by kinetic modeling. *PLoS One* (2014) 9: doi: 10.1371/journal.pone.0089975
196. Teresa Pérez-García M, Cidad P, López-López JR. The secret life of ion channels: Kv1.3 potassium channels and proliferation. *Am J Physiol Cell Physiol* (2018) 314:27–42. doi: 10.1152/ajpcell.00136.2017.-Kv1.3
197. Somodi S, Varga Z, Hajdu P, Starkus JG, Levy DI, Gáspár R″, Panyi G. pH-dependent modulation of Kv1.3 inactivation: role of His399. *Am J Physiol Cell Physiol* (2004) 287:1067–1076. doi: 10.1152/ajpcell.00438.2003.-The
198. Yu SP, Kerchner GA. Rapid Communication Endogenous Voltage-Gated Potassium Channels in Human Embryonic Kidney (HEK293) Cells. *J Neurosci Res* (1998) 52:612–617.
199. Sankaranarayanan A, Raman G, Busch C, Schultz T, Zimin PI, Hoyer J, Köhler R, Wulff H. Naphtho[1,2-d]thiazol-2-ylamine (SKA-31), a new activator of KCa2 and KCa3.1 potassium channels, potentiates the endothelium-derived hyperpolarizing factor response and lowers blood pressure. *Mol Pharmacol* (2009) 75:281–295. doi: 10.1124/mol.108.051425
200. Guéguinou M, Chantôme A, Fromont G, Bougnoux P, Vandier C, Potier-Cartereau M. KCa and Ca2+ channels: The complex thought. *Biochim Biophys Acta Mol Cell Res* (2014) 1843:2322–2333. doi: 10.1016/j.bbamcr.2014.02.019
201. Aiyar J, Withka JM, Rizzi JP, Singteton DH, Gtenn ~, Andrews C, Lin W, Boyd J, Hanson DC, Simon M, et al. Topology of the Pore-Region of a K + Channel Revealed by the NMR-Derived Structures of Scorpion Toxins. *Neuron* (1995) 15:1169–1181.

202. Lee CH, MacKinnon R. Activation mechanism of a human SK-calmodulin channel complex elucidated by cryo-EM structures. *Science (1979)* (2018) 360:508–513. doi: 10.1126/science.aas9466
203. Burg S, Shapiro S, Peretz A, Haimov E, Redko B, Yeheskel A, Simhaev L, Engel H, Raveh A, Ben-Bassat A, et al. Allosteric inhibitors targeting the calmodulin-PIP2 interface of SK4 K+ channels for atrial fibrillation treatment. *Proceedings of the National Academy of Sciences* (2022) 119: doi: 10.1073/pnas.2202926119
204. Bildl W, Strassmaier T, Thurm H, Andersen J, Eble S, Oliver D, Knipper M, Mann M, Schulte U, Adelman JP, et al. Protein Kinase CK2 Is Coassembled with Small Conductance Ca 2-Activated K Channels and Regulates Channel Gating calcium ([Ca 2] i) and provide a hyperpolarizing K con-ductance that is fundamental for a wide range of physio-logical processes, including neuronal excitability (Stocker et al., 1999), rhythmic hormone release from gland cells (Tse and Hille, 1992), smooth muscle tone (Doughty et. (2004). 847–858 p.
205. Zhang M, Meng XY, Cui M, Pascal JM, Logothetis DE, Zhang JF. Selective phosphorylation modulates the PIP 2 sensitivity of the CaM-SK channel complex. *Nat Chem Biol* (2014) 10:753–759. doi: 10.1038/nchembio.1592
206. Allen D, Fakler B, Maylie J, Adelman JP. Organization and regulation of small conductance Ca2+-activated K+ channel multiprotein complexes. *Journal of Neuroscience* (2007) 27:2369–2376. doi: 10.1523/JNEUROSCI.3565-06.2007
207. Bailey MA, Grabe M, Devor DC. Characterization of the PCMBS-dependent modification of KCa3.1 channel gating. *Journal of General Physiology* (2010) 136:367–387. doi: 10.1085/jgp.201010430
208. Musset B, Decoursey T. Biophysical properties of the voltage-gated proton channel HV1. *Wiley Interdiscip Rev Membr Transp Signal* (2012) 1:605–620. doi: 10.1002/wmts.55
209. Hong L, Kim IH, Tombola F. Molecular determinants of Hv1 proton channel inhibition by guanidine derivatives. *Proc Natl Acad Sci U S A* (2014) 111:9971–9976. doi: 10.1073/pnas.1324012111
210. Duan Q, Zhang H, Zheng J, Zhang L. Turning Cold into Hot: Firing up the Tumor Microenvironment. *Trends Cancer* (2020) 6:605–618. doi: 10.1016/j.trecan.2020.02.022
211. Hegde S, Leader AM, Merad M. MDSC: Markers, development, states, and unaddressed complexity. *Immunity* (2021) 54:875–884. doi: 10.1016/j.immuni.2021.04.004
212. Zhang, MD J, Zhang, MD L, Yang, MD Y, Liu, MD Q, Ma, MD H, Huang, MD A, Zhao, MD Y, Xia, MD Z, Liu, MD T, Wu, MD G. Polymorphonuclear-MDSCs Facilitate Tumor Regrowth After Radiation by Suppressing CD8+ T Cells. *Int J Radiat Oncol Biol Phys* (2021) 109:1533–1546. doi: 10.1016/j.ijrobp.2020.11.038
213. Metzger P, Kirchleitner S V., Boehmer DFR, Hörth C, Eisele A, Ormanns S, Gunzer M, Lech M, Lauber K, Endres S, et al. Systemic but not MDSC-specific IRF4 deficiency promotes an immunosuppressed tumor microenvironment in a murine pancreatic cancer model. *Cancer Immunology, Immunotherapy* (2020) 69:2101–2112. doi: 10.1007/s00262-020-02605-9
214. Li M, Zhu D, Wang T, Xia X, Tian J, Wang S. Roles of Myeloid-Derived Suppressor Cell Subpopulations in Autoimmune Arthritis. *Front Immunol* (2018) 9: doi: 10.3389/fimmu.2018.02849
215. Veglia F, Hashimoto A, Dweep H, Sanseviero E, de Leo A, Tcyganov E, Kossenkov A, Mulligan C, Nam B, Masters G, et al. Analysis of classical neutrophils and polymorphonuclear myeloid-derived suppressor cells in cancer patients and tumor-bearing mice. *Journal of Experimental Medicine* (2021) 218: doi: 10.1084/JEM.20201803

216. Trovato R, Fiore A, Sartori S, Canè S, Giugno R, Cascione L, Paiella S, Salvia R, De Sanctis F, Poffe O, et al. Immunosuppression by monocytic myeloid-derived suppressor cells in patients with pancreatic ductal carcinoma is orchestrated by STAT3. *J Immunother Cancer* (2019) 7: doi: 10.1186/s40425-019-0734-6
217. Luan Y, Mosheir E, Menon MC, Wilson D, Woytovich C, Ochando J, Murphy B. Monocytic myeloid-derived suppressor cells accumulate in renal transplant patients and mediate CD4+Foxp3+ treg expansion. *American Journal of Transplantation* (2013) 13:3123–3131. doi: 10.1111/ajt.12461
218. Sinha P, Clements VK, Bunt SK, Albelda SM, Ostrand-Rosenberg S. Cross-Talk between Myeloid-Derived Suppressor Cells and Macrophages Subverts Tumor Immunity toward a Type 2 Response. *The Journal of Immunology* (2007) 179:977–983. doi: 10.4049/jimmunol.179.2.977
219. Ostrand-Rosenberg S, Sinha P, Beury DW, Clements VK. Cross-talk between myeloid-derived suppressor cells (MDSC), macrophages, and dendritic cells enhances tumor-induced immune suppression. *Semin Cancer Biol* (2012) 22:275–281. doi: 10.1016/j.semcancer.2012.01.011
220. Kramer ED, Abrams SI. Granulocytic Myeloid-Derived Suppressor Cells as Negative Regulators of Anticancer Immunity. *Front Immunol* (2020) 11: doi: 10.3389/fimmu.2020.01963
221. Zhou J, Nefedova Y, Lei A, Gabrilovich D. Neutrophils and PMN-MDSC: Their biological role and interaction with stromal cells. *Semin Immunol* (2018) 35:19–28. doi: 10.1016/j.smim.2017.12.004
222. Kowanetz M, Wu X, Lee J, Tan M, Hagenbeek T, Qu X, Yu L, Ross J, Korsisaari N, Cao T, et al. Granulocyte-colony stimulating factor promotes lung metastasis through mobilization of Ly6G+Ly6C+ granulocytes. *Proc Natl Acad Sci U S A* (2010) 107:21248–21255. doi: 10.1073/pnas.1015855107
223. Immler R, Nadolni W, Bertsch A, Morikis V, Rohwedder I, Masgrau-Alsina S, Schroll T, Yevtushenko A, Soehnlein O, Moser M, et al. The voltage-gated potassium channel KV1.3 regulates neutrophil recruitment during inflammation. *Cardiovasc Res* (2022) 118:1289–1302. doi: 10.1093/cvr/cvab133
224. Carmona EM, Peter Larsson H, Neely A, Alvarez O, Latorre R, Gonzalez C. Gating charge displacement in a monomeric voltage-gated proton (Hv1) channel. *Proc Natl Acad Sci U S A* (2018) 115:9240–9245. doi: 10.1073/pnas.1809705115
225. Kawanabe A, Okamura Y. Effects of unsaturated fatty acids on the kinetics of voltage-gated proton channels heterologously expressed in cultured cells. *Journal of Physiology* (2016) 594:595–610. doi: 10.1113/JP271274
226. Ramsey IS, Mokrab Y, Carvacho I, Sands ZA, Sansom MSP, Clapham DE. An aqueous H+ permeation pathway in the voltage-gated proton channel Hv1. *Nat Struct Mol Biol* (2010) 17:869–875. doi: 10.1038/nsmb.1826
227. Ramsey IS, Ruchti E, Kaczmarek JS, Clapham DE. Hv1 proton channels are required for high-level NADPH oxidase-dependent superoxide production during the phagocyte respiratory burst. *Proceedings of the National Academy of Sciences* (2009) 106:7642–7647. doi: 10.1073/pnas.0902761106
228. Rebolledo S, Qiu F, Peter Larsson H. Molecular structure and function of Hv1 channels. *Wiley Interdiscip Rev Membr Transp Signal* (2012) 1:763–777. doi: 10.1002/wmts.49
229. Cherny V V, Markin VS, Decoursey TE. The Voltage-activated Hydrogen Ion Conductance in Rat Alveolar Epithelial Cells Is Determined by the pH Gradient. (1995). 861–896 p.
230. Ma J, Gao X, Li Y, DeCoursey TE, Shull GE, Wang HS. The HVCN1 voltage-gated proton channel contributes to pH regulation in canine ventricular myocytes. *Journal of Physiology* (2022) 600:2089–2103. doi: 10.1113/JP282126

231. Schilling T, Gratopp A, DeCoursey TE, Eder C. Voltage-activated proton currents in huma lymphocytes. *Journal of Physiology* (2002) 545:93–105. doi: 10.1113/jphysiol.2002.028878
232. Wu L-J, Wu G, Sharif MRA, Baker A, Jia Y, Fahey FH, Luo HR, Feener EP, Clapham DE. The voltage-gated proton channel Hv1 enhances brain damage from ischemic stroke. *Nat Neurosci* (2012) 15:565–573. doi: 10.1038/nn.3059
233. Hondares E, Brown MA, Musset B, Morgan D, Cherny V V., Taubert C, Bhamrah MK, Coe D, Marelli-Berg F, Gribben JG, et al. Enhanced activation of an amino-terminally truncated isoform of the voltage-gated proton channel HVCN1 enriched in malignant B cells. *Proc Natl Acad Sci U S A* (2014) 111:18078–18083. doi: 10.1073/pnas.1411390111
234. El Chemaly A, Okochi Y, Sasaki M, Arnaudeau S, Okamura Y, Demaurex N. VSOP/Hv1 proton channels sustain calcium entry, neutrophil migration, and superoxide production by limiting cell depolarization and acidification. *Journal of Experimental Medicine* (2010) 207:129–139. doi: 10.1084/jem.20091837
235. Ohl K, Tenbrock K. Reactive Oxygen Species as Regulators of MDSC-Mediated Immune Suppression. *Front Immunol* (2018) 9: doi: 10.3389/fimmu.2018.02499
236. Huber V, Camisaschi C, Berzi A, Ferro S, Lugini L, Triulzi T, Tuccitto A, Tagliabue E, Castelli C, Rivoltini L. Cancer acidity: An ultimate frontier of tumor immune escape and a novel target of immunomodulation. *Semin Cancer Biol* (2017) 43:74–89. doi: 10.1016/j.semcancer.2017.03.001
237. Coe D, Poobalasingam T, Fu H, Bonacina F, Wang G, Morales V, Moregola A, Mitro N, Cheung KCP, Ward EJ, et al. Loss of voltage-gated hydrogen channel 1 expression reveals heterogeneous metabolic adaptation to intracellular acidification by T cells. *JCI Insight* (2022) 7: doi: 10.1172/jci.insight.147814
238. Pethő Z, Najder K, Carvalho T, McMorrow R, Todesca LM, Rugi M, Bulk E, Chan A, Löwik CWGM, Reshkin SJ, et al. pH-channeling in cancer: How pH-dependence of cation channels shapes cancer pathophysiology. *Cancers (Basel)* (2020) 12:1–37. doi: 10.3390/cancers12092484
239. Hosonuma M, Yoshimura K. Association between pH regulation of the tumor microenvironment and immunological state. *Front Oncol* (2023) 13: doi: 10.3389/fonc.2023.1175563
240. Bell DC, Leanza L, Gentile S, Sauter DR. News and views on ion channels in cancer: is cancer a channelopathy? *Front Pharmacol* (2023) 14: doi: 10.3389/fphar.2023.1258933
241. Lang F, Stournaras C. Ion channels in cancer: Future perspectives and clinical potential. *Philosophical Transactions of the Royal Society B: Biological Sciences* (2014) 369: doi: 10.1098/rstb.2013.0108
242. Cozzolino M, Panyi G. Intracellular acidity impedes KCa3.1 activation by Riluzole and SKA-31. *Front Pharmacol* (2024) 15: doi: 10.3389/fphar.2024.1380655
243. Broomand A, Österberg F, Wardi T, Elinder F. Electrostatic domino effect in the Shaker K channel turret. *Biophys J* (2007) 93:2307–2314. doi: 10.1529/biophysj.107.104349
244. Teisseyre A, Mozrzymas JW. The influence of protons and zinc ions on the steady-state inactivation of Kv1.3 potassium channels. *Cell Mol Biol Lett* (2007) 12:220–230. doi: 10.2478/s11658-006-0067-6
245. Deutsch C, Lee SC. Modulation of K+ currents in human lymphocytes by pH. *Joutrnal of Physiology* (1989) 413:399–413.
246. Sforna L, Megaro A, Pessia M, Franciolini F, Catacuzzeno L. Structure, Gating and Basic Functions of the Ca2+-activated K Channel of Intermediate Conductance. *Curr Neuropharmacol* (2018) 16:608–617. doi: 10.2174/1570159x15666170830122402

247. Gonzales EB, Kawate T, Gouaux E. Pore architecture and ion sites in acid-sensing ion channels and P2X receptors. *Nature* (2009) 460:599–604. doi: 10.1038/nature08218
248. Cheng YR, Jiang BY, Chen CC. Acid-sensing ion channels: Dual function proteins for chemo-sensing and mechano-sensing. *J Biomed Sci* (2018) 25: doi: 10.1186/s12929-018-0448-y
249. Somodi S, Hajdu P, Gáspár R, Panyi G, Varga Z. Effects of changes in extracellular pH and potassium concentration on Kv1.3 inactivation. *European Biophysics Journal*. (2008). p. 1145–1156 doi: 10.1007/s00249-008-0267-2
250. Starkus JG, Varga Z, Schönherr R, Heinemann SH. Mechanisms of the inhibition of Shaker potassium channels by protons. *Pflugers Arch* (2003) 447:44–54. doi: 10.1007/s00424-003-1121-0
251. Pandey K, Dhoke RR, Rathore YS, Nath SK, Verma N, Bawa S, Ashish. Low pH overrides the need of calcium ions for the shape-function relationship of calmodulin: Resolving prevailing debates. *Journal of Physical Chemistry B* (2014) 118:5059–5074. doi: 10.1021/jp501641r
252. Valeyev N V., Bates DG, Heslop-Harrison P, Postlethwaite I, Kotov N V. Elucidating the mechanisms of cooperative calcium-calmodulin interactions: A structural systems biology approach. *BMC Syst Biol* (2008) 2: doi: 10.1186/1752-0509-2-48
253. Iida S, Potter JD. Calcium Binding to Calmodulin. Cooperativity of the Calcium-Binding Sites. *The Journal of Biochemistry* (1986) 99:1765–1772. doi: 10.1093/oxfordjournals.jbchem.a135654
254. Brown BM, Shim H, Christophersen P, Wulff H. Pharmacology of Small- and Intermediate-Conductance Calcium-Activated Potassium Channels. *Annual Review of Pharmacology and Toxicology Annu Rev Pharmacol Toxicol 2020* (2019) 60:219–240. doi: 10.1146/annurev-pharmtox-010919
255. Srivastava S, Panda S, Li Z, Fuhs SR, Hunter T, Thiele DJ, Hubbard SR, Skolnik EY. Histidine phosphorylation relieves copper inhibition in the mammalian potassium channel KCa3.1. *Elife* (2016) 5: doi: 10.7554/eLife.16093
256. Srivastava S, Li Z, Ko K, Choudhury P, Albaqumi M, Johnson AK, Yan Y, Backer JM, Unutmaz D, Coetzee WA, et al. Histidine Phosphorylation of the Potassium Channel KCa3.1 by Nucleoside Diphosphate Kinase B Is Required for Activation of KCa3.1 and CD4 T Cells. *Mol Cell* (2006) 24:665–675. doi: 10.1016/j.molcel.2006.11.012
257. Ji T, Corbalán-García S, Hubbard SR. Crystal structure of the C-terminal four-helix bundle of the potassium channel KCa3.1. *PLoS One* (2018) 13: doi: 10.1371/journal.pone.0199942
258. Zechel S, Hager MD, Priemel T, Harrington MJ. Healing through histidine: Bioinspired pathways to self-healing polymers via imidazole-metal coordination. *Biomimetics* (2019) 4: doi: 10.3390/biomimetics4010020
259. Chandy KG, Norton RS. Immunology: Channelling potassium to fight cancer. *Nature* (2016) 537:497–499. doi: 10.1038/nature19467
260. Brown BM, Pressley B, Wulff H. KCa3.1 Channel Modulators as Potential Therapeutic Compounds for Glioblastoma. *Curr Neuropharmacol* (2017) 15: doi: 10.2174/1570159x15666170630164226
261. Chirra M, Newton HS, Gawali VS, Wise-Draper TM, Chimote AA, Conforti L. How the Potassium Channel Response of T Lymphocytes to the Tumor Microenvironment Shapes Antitumor Immunity. *Cancers (Basel)* (2022) 14: doi: 10.3390/cancers14153564
262. Eil R, Vodnala SK, Clever D, Klebanoff CA, Sukumar M, Pan JH, Palmer DC, Gros A, Yamamoto TN, Patel SJ, et al. Ionic immune suppression within the tumour microenvironment limits T cell effector function. *Nature* (2016) 537:539–543. doi: 10.1038/nature19364

263. Chiarella AM, Ryu YK, Manji GA, Rustgi AK. Extracellular ATP and Adenosine in Cancer Pathogenesis and Treatment. *Trends Cancer* (2021) 7:731–750. doi: 10.1016/j.trecan.2021.04.008
264. Huber V, Camisaschi C, Berzi A, Ferro S, Lugini L, Triulzi T, Tuccitto A, Tagliabue E, Castelli C, Rivoltini L. Cancer acidity: An ultimate frontier of tumor immune escape and a novel target of immunomodulation. *Semin Cancer Biol* (2017) 43:74–89. doi: 10.1016/j.semcancer.2017.03.001
265. Chimote AA, Balajthy A, Arnold MJ, Newton HS, Hajdu P, Qualtieri J, Wise-Draper T, Conforti L. A defect in KCa3.1 channel activity limits the ability of CD8+ T cells from cancer patients to infiltrate an adenosine-rich microenvironment. *Sci Signal* (2018) 11: doi: 10.1126/scisignal.aaq1616
266. Navarro F, Casares N, Martín-Otal C, Lasarte-Cía A, Gorraiz M, Sarrión P, Llopiz D, Reparaz D, Varo N, Rodriguez-Madoz JR, et al. Overcoming T cell dysfunction in acidic pH to enhance adoptive T cell transfer immunotherapy. *Oncoimmunology* (2022) 11: doi: 10.1080/2162402X.2022.2070337
267. Soret B, Hense J, Lüdtke S, Thale I, Schwab A, Düfer M. Pancreatic KCa3.1 channels in health and disease. *Biol Chem* (2023) 404:339–353. doi: 10.1515/hsz-2022-0232
268. Ohya S, Kimura K, Niwa S, Ohno A, Kojima Y, Sasaki S, Kohri K, Imaizumi Y. Malignancy Grade-Dependent Expression of K +-Channel Subtypes in Human Prostate Cancer. *Journal of Pharmacological Sciences J Pharmacol Sci* (2009) 109:1.
269. Bulk E, Ay AS, Hammadi M, Ouadid-Ahidouch H, Schelhaas S, Hascher A, Rohde C, Thoennissen NH, Wiewrodt R, Schmidt E, et al. Epigenetic dysregulation of KCa3.1 channels induces poor prognosis in lung cancer. *Int J Cancer* (2015) 137:1306–1317. doi: 10.1002/ijc.29490
270. Gross D, Bischof H, Maier S, Sporbeck K, Birkenfeld AL, Malli R, Ruth P, Proikas-Cezanne T, Lukowski R. IKCa channels control breast cancer metabolism including AMPK-driven autophagy. *Cell Death Dis* (2022) 13: doi: 10.1038/s41419-022-05329-z

10 APPENDIX

UNIVERSITY of DEBRECEN

UNIVERSITY AND NATIONAL LIBRARY
UNIVERSITY OF DEBRECEN
H-4002 Egyetem tér 1, Debrecen
Phone: +3652/410-443, email: publikaciok@lib.unideb.hu

Registry number: DEENK/465/2024.PL
Subject: PhD Publication List

Candidate: Marco Cozzolino
Doctoral School: Doctoral School of Molecular Medicine

List of publications related to the dissertation

1. **Cozzolino, M.**, Panyi, G.: Intracellular acidity impedes KCa3.1 activation by Riluzole and SKA-31. *Front. Pharmacol. 15*, 1-23, 2024.
   DOI: http://dx.doi.org/10.3389/fphar.2024.1380655
   IF: 5.6 (2022)
2. **Cozzolino, M.**, Gyöngyösi, A., Korpos, É., Gogolák, P., Naseem, M. U., Kállai, J., Lányi, Á., Panyi, G.: The Voltage-Gated Hv1 H^+ Channel Is Expressed in Tumor-Infiltrating Myeloid-Derived Suppressor Cells.
   Int. J. Mol. Sci. 24 (7), 1-24, 2023.
   DOI: http://dx.doi.org/10.3390/ijms24076216
   IF: 5.6 (2022)

DEBRECENI EGYETEM Egyetemi és Nemzeti Könyvtár

UNIVERSITY AND NATIONAL LIBRARY
UNIVERSITY OF DEBRECEN
H-4002 Egyetem tér 1, Debrecen
Phone: +3652/410-443, email: publikaciok@lib.unideb.hu

List of other publications

3. Somodi, L., Bekéné Debreceni, I., Kis, G., **Cozzolino, M.**, Kappelmayer, J., Antal, M., Panyi, G., Bárdos, H., Mutch, N. J., Muszbek, L.: Activation mechanism dependent surface exposure of cellular factor XIII on activated platelets and platelet microparticles.
J. Thromb. Haemost. 20 (5), 1223-1235, 2022.
DOI: http://dx.doi.org/10.1111/jth.15668
IF: 10.4

4. Hofschröer, V., Najder, K., Rugi, M., Bouazzi, R., **Cozzolino, M.**, Arcangeli, A., Panyi, G., Schwab, A.: Ion Channels Orchestrate Pancreatic Ductal Adenocarcinoma Progression and Therapy.
Front. Pharmacol. 11, 1-28, 2021.
DOI: http://dx.doi.org/10.3389/fphar.2020.586599
IF: 5.988

Total IF of journals (all publications): 27,588
Total IF of journals (publications related to the dissertation): 11,2

The Candidate's publication data submitted to the iDEa Tudóstér have been validated by DEENK on the basis of the Journal Citation Report (Impact Factor) database.

03 September, 2024